UNCLASSIFIED

SECURITY CLASSIFICATION OF THIS PAGE *(When Data Entered)*

REPORT DOCUMENTATION PAGE		READ INSTRUCTIONS BEFORE COMPLETING FORM
1. REPORT NUMBER TR-913	2. GOVT ACCESSION NO. *	3. RECIPIENT'S CATALOG NUMBER
4. TITLE *(and Subtitle)* A SUMMARY OF THE PREVOST EFFECTIVE STRESS SOIL MODEL		5. TYPE OF REPORT & PERIOD COVERED Final; Oct 1983 – Sep 1984 6. PERFORMING ORG. REPORT NUMBER
7. AUTHOR(s) J. M. Ferritto and R. T. Nakamoto		8. CONTRACT OR GRANT NUMBER(s)
9. PERFORMING ORGANIZATION NAME AND ADDRESS NAVAL CIVIL ENGINEERING LABORATORY Port Hueneme, California 93043		10. PROGRAM ELEMENT, PROJECT, TASK AREA & WORK UNIT NUMBERS YR023.03.01.004 ZR000-001-188
11. CONTROLLING OFFICE NAME AND ADDRESS Naval Facilities Engineering Command Alexandria, Virginia 22332		12. REPORT DATE October 1983 13. NUMBER OF PAGES 105
14. MONITORING AGENCY NAME & ADDRESS*(if different from Controlling Office)* Chief of Naval Material Navy Department Washington, DC 20360		15. SECURITY CLASS. *(of this report)* Unclassified 15a. DECLASSIFICATION/DOWNGRADING SCHEDULE

16. DISTRIBUTION STATEMENT *(of this Report)*

Approved for public release; distribution is unlimited.

17. DISTRIBUTION STATEMENT *(of the abstract entered in Block 20, if different from Report)*

18. SUPPLEMENTARY NOTES

*DN287264
DN487267

19. KEY WORDS *(Continue on reverse side if necessary and identify by block number)*

Effective stress, soil model, testing, finite elements

20. ABSTRACT *(Continue on reverse side if necessary and identify by block number)*

This report presents a summary of the Prevost effective stress soil model. A summary of the model formulation is given with its implementation into the DYNAFLOW finite element code. Test data are compared with code prediction. Several boundary value problems are solved as a demonstration of capability.

DD FORM 1 JAN 73 1473 EDITION OF 1 NOV 65 IS OBSOLETE

UNCLASSIFIED

SECURITY CLASSIFICATION OF THIS PAGE *(When Data Entered)*

Library Card

Naval Civil Engineering Laboratory
A SUMMARY OF THE PREVOST EFFECTIVE STRESS
SOIL MODEL (Final), by J. M. Ferritto and R. T. Nakamoto
TR-913 105 pp illus October 1984 Unclassified

1. Effective stress 2. Finite element I. YR023.03.01.004

This report presents a summary of the Prevost effective stress soil model. A summary of the model formulation is given with its implementation into the DYNAFLOW finite element code. Test data are compared with code prediction. Several boundary value problems are solved as a demonstration of capability.

CONTENTS

INTRODUCTION

Characterizing soil behavior under loading is a complex task. In recent years the finite element method has been a useful tool in analyzing structures, structures on soil, and soil-structures themselves. Emphasis in the past has been placed on use of nonlinear plasticity soil models to capture soil response more accurately. Recent work has focused on effective stress analysis - the ability not only to calculate soil stress but also to calculate pore fluid pressure.

An effective stress model can be applied to analysis of ocean floor soils, nearshore and offshore structures, and seismic phenomena. Oscillations in loading, whether from wave action or seismic shaking, produce dynamic loading that can induce significant increases in pore pressure. In turn this increase in pore pressure can reduce allowable soil capacities and at the same time increase deformations from a reduction in effective confining stress. Under extreme conditions, flow slides and liquefaction occur. Although liquefaction has been identified as a phenomenon for 20 years, soil mechanics experts are just beginning to understand the interaction of stress confinement and drainage path that occurs in the field, such as under a foundation or around a pile. For example, common engineering practice in evaluating seismically induced soil liquefaction considers ground conditions as level away from the structure, and shear stresses from the structure are not even considered. Also, present design guidelines for pile foundations are based on static load.

Recent earthquakes, particularly those in Alaska, Japan, and Chile, have emphasized the high damage threat the soil liquefaction phenomenon poses to waterfront structures. In the 1960 Chilean earthquake (magnitude 7) quaywalls, sheet piles, and sea walls were damaged by

liquefaction of loose, fine, sandy soils. In the 1964 Alaskan earthquake (magnitude 8.4) severe damage to Anchorage, Cordova, and Valdez occurred, including large-scale landslides, as a result of liquefaction. Japanese earthquakes (Niigata, 1964, magnitude 7.3; Miyagi-Ken-Oki, 1978, magnitude 7.4) caused severe waterfront damage to wharfs, bulkheads, quaywalls, piers, and conventional structures. The majority of the damage sustained in waterfront areas was from liquefaction of loose, cohesionless sands.

A study conducted by the Office of Naval Research (Ref 1) recognized a major liquefaction hazard existing at West Coast Naval activities. A more recent investigation at the Naval Air Station (NAS), North Island, Calif. (Ref 2), concluded that liquefaction under design earthquake levels could result in destruction of such critical structures as aircraft carrier berths, aviation fuel tank farms, and underground utility service lines. Unfortunately, almost all previous studies of the liquefaction problem have been concerned with either conventional building foundations or with analyses of dams, and procedures for analyzing specialized Navy structures are not available.

The effective stress model is of major significance since the Navy must locate in areas where the water table is high. Even if liquefaction (a loss of shear strength from a loss of effective confining stress) does not occur, a buildup of pore pressure is probable both in sands and clays. This pore pressure buildup can be of major significance in structural behavior.

The Navy has a drydock certification program in progress. The drydocks are examples of structures surrounded by soil, often with a high water table. Soil loading causes wall deflections which, in turn, alter the soil load. Note that even though drydocks are critical Navy structures, the present analytical techniques reflect the state-of-the-art of 1950. Basically, static structural analysis procedures are used with estimates of the soil pressure. The drydock is only one of many types of waterfront structures illustrating the significance of soil-structure interaction.

The effective stress soil model is a critical tool for use on waterfront structures. Dynamic analysis techniques are essential for a realistic assessment of drydock safety. Drydocks are only one application; others include quaywalls, bulkheads, retaining walls, ocean floor structures, as well as other structures.

Effective stress techniques are also useful in understanding site behavior because pore pressure builds up during the cyclic loading process, increasing deformations.

Conventional finite element techniques presently utilize a total stress approach characterizing the soil elastically in terms of shear modulus and Poisson's ratio or inelastically in terms of a curved stress-strain fit typically from single triaxial compression and extension tests. This approach does not consider the pore fluid separately from the soil skeleton, but actual soil behavior depends heavily upon the behavior of the fluid. Initially upon loading, much of the load is carried by the near incompressible fluid; as drainage occurs, load is transferred to the soil skeleton. Fluid flow controlled by soil permeability plays an important part in computations of the actual loading and settlements in the soil. To neglect the pore fluid, as is presently done in total stress finite element programs used today, is a gross oversimplification limited to dry soils and is not well-suited to waterfront construction.

This report summarizes previous work, and has been funded by Minerals Management Service and the Navy. During FY81 a detailed review of available material models was made, and model behavior was compared with test data (Ref 3). Based on the comparative study, it was determined that the Prevost model was applicable to both cohesive and cohesionless materials and that its development was very far along and well into the implementation stage.

During FY82, modifications were accomplished by contract with Professor J.H. Prevost to include the effects of cyclic degradation. Soil test data were obtained by contract with Professor P. Lade of the University of California at Los Angeles, Calif. (UCLA). Reference 4 presents this work. During FY83, additional test data were obtained by contract with Dr. Richard Ladd, Woodward-Clyde Consultants (Ref 5).

Test data and model prediction were compared, and several boundary value problems were tried (Ref 6). During the current fiscal year, work continued on comparison of model prediction and test data and also on advanced boundary value problem formulation and solution. Required enhancements were made in the program formulation.

PREVOST SOIL MODEL FORMULATION

In the Prevost soil model, soil is viewed as a multi-phase medium consisting of an inelastic porous skeleton and viscous fluids. The model (Ref 7 and 8) is a general analytical model that describes the nonlinear, anisotropic, elasto-plastic, stress and strain dependent, and strength properties of the skeleton when subjected to a three-dimensional loading. The following is taken directly from Prevost (Ref 9).

The constitutive equations for the solid skeleton are written in one of the following forms:

$$\underset{\sim}{C} : \overset{\cdot}{\underset{\sim}{\varepsilon}} = \begin{cases} \overset{\cdot}{\underset{\sim}{\sigma}}' & \text{small deformations} \\ \overset{\nabla}{\underset{\sim}{\sigma}}' + \underset{\sim}{\sigma}' \text{ div } \underset{\sim}{v} & \text{finite deformations} \end{cases} \tag{1}$$

where: $\underset{\sim}{\sigma}'$ = effective Cauchy stress tensor

$\underset{\sim}{v}$ = spatial velocity of solid phase

$\overset{\cdot}{\underset{\sim}{\varepsilon}}$ = the rate of deformation tensor for the solid phase (symmetric part of the spatial solid velocity gradient)

$\cdot$ = material derivative

$\overset{\nabla}{\underset{\sim}{\sigma}}'$ = Jaumann derivative, given by:

$$\overset{\nabla}{\underset{\sim}{\sigma}}' = \overset{\cdot}{\underset{\sim}{\sigma}}' + \underset{\sim}{\sigma}' \cdot \underset{\sim}{w} - \underset{\sim}{w} \cdot \sigma' \tag{2}$$

where $\underset{\sim}{w}$ is the spin tensor for the solid phase (skew-symmetric part of the spatial solid velocity gradient). In Equation 1, C_{abcd} is a tensor valued function $\underset{\sim}{\sigma}'$ and the solid deformation gradients.

For soil media, the form of the C-tensor is given as follows,

$$\underset{\sim}{C} = \underset{\sim}{E} - \frac{(\underset{\sim}{E}:\underset{\sim}{P})\ (\tilde{\underset{\sim}{Q}}:\underset{\sim}{E})}{H' + \underset{\sim}{Q}:\underset{\sim}{E}:\underset{\sim}{P}} \tag{3}$$

where: H' = plastic modulus

$\underset{\sim}{P}$ and $\underset{\sim}{Q}$ = symmetric second-order tensors, such that $\underset{\sim}{P}$ gives the direction of plastic deformations and $\tilde{\underset{\sim}{Q}}$ the outer normal to the active yield surface

$\underset{\sim}{E}$ = fourth-order tensor of elastic moduli, assumed isotropic, viz.,

$$E_{abcd} = \Lambda\, \delta_{ab}\delta_{bc} + G\,(\delta_{ac}\delta_{bd} + \delta_{ad}\delta_{bc}) \tag{4}$$

where Λ and G are Lame's constants, and δ_{ab} is the Kronecker delta. The yield function is selected of the following form

$$f = \frac{3}{2}\,(\underset{\sim}{S} - \underset{\sim}{\alpha}) : (\underset{\sim}{S} - \underset{\sim}{\alpha}) + C^2\,(p' - \beta)^2 = k^2 \tag{5}$$

where: $\underset{\sim}{S} = \underset{\sim}{\sigma}' - p'\underset{\sim}{1}$ = deviatoric stress tensor

$p' = (1/3)\ \mathrm{tr}\ \underset{\sim}{\sigma}'$ = effective mean normal stress

$\underset{\sim}{\alpha}$ and β = coordinates of the center of the yield surface in the deviatoric stress subspace and along the hydrostatic stress axis, respectively

k = size of the yield surface

C = material parameter called the yield surface axis ratio

From Equation 5

$$\mathrm{grad}\ f = \frac{\partial f}{\partial \underset{\sim}{\sigma}'} = 3\,(\underset{\sim}{S} - \underset{\sim}{\alpha}) + \frac{2}{3} - C^2\,(p' - \beta)\,\underset{\sim}{1} \tag{6}$$

and

$$\left|\ \mathrm{grad}\ f\ \right|^2 = 6k^2 + 6C^2\,(\tfrac{2}{9}\,C^2 - 1)\,(p' - \beta)^2 \tag{7}$$

It is convenient to decompose $\underset{\sim}{P}$ and $\underset{\sim}{Q}$ into their deviatoric and dilational components, and in the following

$$\underset{\sim}{P} = \underset{\sim}{P}' + P'' \underset{\sim}{1} \qquad \underset{\sim}{Q} = \underset{\sim}{Q}' + Q'' \underset{\sim}{1} \tag{8}$$

where

$$P'' = \frac{1}{3} \operatorname{tr} \underset{\sim}{P} \qquad Q'' = \frac{1}{3} \operatorname{tr} \underset{\sim}{Q} \tag{9}$$

and

$$\underset{\sim}{Q} = \operatorname{grad} f / \left| \operatorname{grad} f \right| \tag{10}$$

The plastic potential is selected such that the plastic rate of deformation vector remains normal to the projection of the yield surface onto the deviatoric stress subspace

$$\underset{\sim}{P}' = \underset{\sim}{Q}' \tag{11a}$$

and

$$3P'' = Q'' + A \operatorname{tr} (\underset{\sim}{Q}')^3 / \operatorname{tr} (\underset{\sim}{Q}')^2 \tag{11b}$$

where

$$\operatorname{tr} (\underset{\sim}{Q}')^2 = \underset{\sim}{Q}' : \underset{\sim}{Q}' = Q'_{ab} Q'_{ab} \tag{12}$$

$$\operatorname{tr} (\underset{\sim}{Q}')^3 = 3 \det (\underset{\sim}{Q}') = Q'_{ab} Q'_{bc} Q'_{ca}$$

where A is the material parameter which measures the departure from an associative plastic flow rule. When A = 0, the principal directions of $\underset{\sim}{P}$ and $\underset{\sim}{Q}$ coincide and consequently the $\underset{\sim}{C}$ tensor possesses the major symmetry and leads to a symmetric material tangent stiffness. On the other hand, when $A \neq 0$, the principal directions of $\underset{\sim}{P}$ and $\underset{\sim}{Q}$ do not coincide, and $\underset{\sim}{C}$ does not possess the major symmetry.

From Equations 4, 8, and 9,

$$\underset{\sim}{Q}:\underset{\sim}{\underset{\sim}{E}}:\underset{\sim}{P} = B \text{ tr } \underset{\sim}{P} \text{ tr } \underset{\sim}{Q} + 2G \underset{\sim}{P}':\underset{\sim}{Q}' \tag{13}$$

where $B = \Lambda + 2G/3$ = the elastic bulk

G = shear moduli

For the small deformation case:

$$\dot{\underset{\sim}{\sigma}}' = 2G \dot{\underset{\sim}{\varepsilon}} + (B-\frac{2G}{3}) \dot{\varepsilon}_v \underset{\sim}{1} \tag{14}$$

$$- (2G \underset{\sim}{Q}' + B\ 3P'' \underset{\sim}{1})\left(\frac{2G \underset{\sim}{Q}' \dot{\underset{\sim}{\varepsilon}} + B\ 3Q'' \dot{\varepsilon}_v}{H' + 2G \underset{\sim}{Q}':\underset{\sim}{Q}' + B\ 3Q''3P''}\right)$$

where $\dot{\varepsilon}_v = \text{tr } \dot{\underset{\sim}{\varepsilon}}$; or, equivalently, in terms of deviatoric and dilational components:

$$\dot{\underset{\sim}{S}} = 2G \dot{\underset{\sim}{e}} - 2G \underset{\sim}{Q}'\left(\frac{2G \underset{\sim}{Q}' \dot{\underset{\sim}{e}} + B\ 3Q'' \dot{\varepsilon}_v}{H' + 2G \underset{\sim}{Q}':\underset{\sim}{Q}' + B\ 3Q''\ 3P''}\right) \tag{15a}$$

$$\dot{p}' = B \dot{\varepsilon}_v - B\ 3P''\left(\frac{2G \underset{\sim}{Q}':\dot{\underset{\sim}{e}} + B\ 3Q'' \dot{\varepsilon}_v}{H' + 2G \underset{\sim}{Q}':\underset{\sim}{Q}' + B\ 3Q''3P''}\right) \tag{15b}$$

where $\dot{\underset{\sim}{e}} = \dot{\underset{\sim}{\varepsilon}} - \dot{\varepsilon}_v \underset{\sim}{1}$ = deviatoric rate of deformation tensor. When $\underset{\sim}{Q}' = 0$, $3Q''^2 = 1$ and Equation 15b simplifies to

$$\dot{p} = (\frac{1}{B} + \frac{1}{H'})^{-1} \dot{\varepsilon}_v \tag{16}$$

and the plastic modulus H' thus plays the role of a plastic <u>bulk</u> modulus. Similarly, when $Q'' = 0$, $\underset{\sim}{Q}':\underset{\sim}{Q}' = 1$ and Equation 15 yields

$$\underset{\sim}{Q}':\dot{\underset{\sim}{S}} = (\frac{1}{2G} + \frac{1}{H'})^{-1} \underset{\sim}{Q}':\dot{\underset{\sim}{e}} \tag{17}$$

and the plastic modulus H' thus plays the role of a plastic <u>shear</u> modulus.

When $C = 0$, the yield surface plots in stress space as a cylinder (translated Von-Mises yield surface) whose axis is parallel to the space diagonal. When $C \neq 0$, the yield surface plots in stress space as an ellipsoidal surface of revolution whose axis is parallel to the space diagonal. In order to allow for the adjustment of the plastic hardening rule to any kind of experimental data (for example, data obtained from axial or simple shear soil tests), a collection of nested yield surfaces is used. The surfaces are all similar; i.e., the axis ratio C in Equation 5 is the same for all yield surfaces. The yield surfaces, in general, may translate and change in size, but never rotate. The model, therefore, combines properties of isotropic and kinematic plasticity. In order to avoid overlappings of the surfaces (which would lead to a non-unique definition of the constitutive theory) the isotropic/kinematic hardening rule couples the simultaneous deformation/translation of all yield surfaces. A plastic modulus $H'^{(m)}$ and a non-associative parameter $A^{(m)}$ are associated with each yield surface, m. In general, both $A^{(m)}$ and $H'^{(m)}$ are allowed to take different values at different locations on any given yield surface; i.e., both $A^{(m)}$ and $H'^{(m)}$ are functions of position.

The following rules have been used for $A^{(m)}$ and $H'^{(m)}$:

Cohesive soils: $A^{(m)}$ is constant on each surface, and

$$H'^{(m)} = h'^{(m)} + \frac{\text{tr } \underset{\sim}{Q}^{(m)}}{\sqrt{3}} B'^{(m)} \tag{18}$$

where $h'^{(m)}$ = plastic shear modulus, and $[h'^{(m)} \pm B'^{(m)}]$ = the plastic bulk moduli.

Cohesionless soils: Both $A^{(m)}$ and $H'^{(m)}$ are allowed to vary on each yield surface;

$$A^{(m)} = A_i^{(m)} \quad \begin{cases} i=1 \text{ if } \text{tr } (\underset{\sim}{Q}'^{(m)})^3 > 0 \\ i=2 \text{ if } \text{tr } (\underset{\sim}{Q}'^{(m)})^3 < 0 \end{cases} \tag{19}$$

and

$$H'^{(m)} = h_i'^{(m)} \left| \frac{\text{tr } (\underset{\sim}{Q}'^{(m)})^3}{A_i} \right| + B_i'^{(m)} \left| 1 - \frac{\text{tr } (\underset{\sim}{Q}'^{(m)})^3}{A_i} \right| \qquad (20)$$

$$\begin{cases} i=1 \text{ if } \text{tr } \underset{\sim}{Q}^{(m)} > 0 \\ i=2 \text{ if } \text{tr } \underset{\sim}{Q}^{(m)} < 0 \end{cases}$$

where $h_i'^{(m)}$ and $B_i'^{(m)}$ play the role of plastic shear and bulk moduli, respectively.

The yield surfaces' initial positions and sizes reflect the past stress-strain history of the soil skeleton, and their initial positions, in particular, are a direct expression of the material's "memory" of its past loading history. Because the $\underset{\sim}{\alpha}$'s are not necessarily all equal to zero, the yielding of the material is anisotropic. Direction is therefore of importance, and the physical reference axes (x,y,z) are fixed with respect to the material element and specified to coincide with the reference axes of consolidation. For a soil element whose anisotropy initially exhibits rotational symmetry about the y-axis, $\alpha_x = \alpha_z = -\alpha_y/2$, and Equation 5 simplifies to

$$[(\sigma_y' - \sigma_x') - \alpha]^2 + C^2 (p' - \beta)^2 - k^2 = 0 \qquad (21)$$

where α is $3\alpha_y/2$. The yield surfaces then plot as ellipses in the axisymmetric stress plane ($\sigma_x' = \sigma_z'$) as shown in Figure 1a. Points C and E on the outermost yield surface define the critical state conditions (i.e., $H' = 0$) for axial compression and extension loading conditions, respectively. It is assumed that the slopes of the critical state lines OC and OE remain constant during yielding.

The yielding surfaces are allowed to change in size as well as to be translated by the stress point. Their associated plastic moduli are also allowed to vary; in general, both k and H' are functions of the

plastic strain history. They are conveniently taken as functions of invariant measures of the amount of plastic volumetric strains or plastic shear distortions, respectively. Complete specification of the model parameters requires the determination of:

(1) the initial positions and sizes of the yield surfaces together with their associated plastic moduli

(2) their size or plastic modulus changes as loading proceeds

(3) the elastic shear G and bulk B moduli

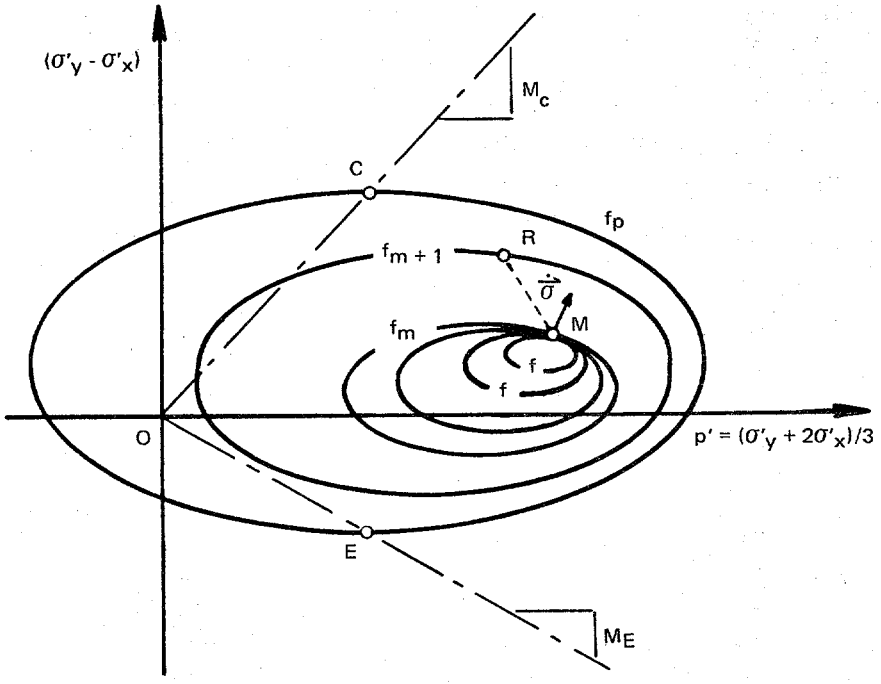

Figure 1(a). Prevost soil model - Field of yield surfaces.

The yield surface $f^{(1)}$ is chosen as a degenerate yield surface of size $k^{(1)} = 0$ which coincides with the stress point. Further, in order to get a smooth transition from the elastic into the plastic regime, $A^{(1)} = 0$ and $H'^{(1)} = \infty$, so that the material behavior inside $f^{(2)}$ is purely elastic. The dependence of the model parameters upon the effective mean normal stress and volumetric strain are assumed of the following form

$$x = x_1 \left(\frac{p'}{p'_1}\right)^n \qquad y = y_1 \exp(\lambda \varepsilon_v) \tag{22a}$$

respectively, where

$$x = B,\ G \text{ and } H'^{(m)}$$

and

$$y = \alpha_{ab}^{(m)},\ \beta^{(m)} \text{ and } k^{(m)}$$

where: n = experimental parameter ($n = 0.5$ for most cohesionless soils and $n = 1$ for most cohesive soils)

p'_1 = reference effective mean normal stress (i.e., at $\varepsilon_v = 0$ when $p' = p'_1$).

It is assumed that when the soil is in a "normally consolidated" state, the consolidation soil test results plot (1) as a straight line parallel to the projections of the critical state lines in the $\ell n(p'/p'_1)$ versus ε_v diagram and (2) as a straight line in the axial stress plane. The parameter λ is then simply determined from the results of K_o minus consolidation soil test results.

$$\lambda = \frac{1}{p'_K} \frac{\dot{p}'_K}{\dot{\varepsilon}^K_v} \tag{22b}$$

where the subscript/superscript K refers to K_o minus loading conditions. The soil's anisotropy originally develops during its deposition and subsequent consolidation which, in most practical cases, occurs under no lateral deformations. In the following, the y-axis is vertical and coincides with the direction of consolidation, the horizontal xz-plane is thus a plane of the material's isotropy; and the material's anisotropy initially exhibits rotational symmetry about the vertical y-axis. The model parameters required to characterize the behavior of any given soil can then be derived entirely from the results of conventional monotonic axial and cyclic strain-controlled simple shear soil texts. The above material in this section is based on Reference 9.

DETERMINATION OF MODEL PARAMETERS

Compressive stresses and strains are considered positive and all stresses are effective stresses unless otherwise specified. For a material which initially exhibits cross-anisotropy about the vertical y-axis, the initial position in stress space of the yield surfaces are defined by the sole determination of the two parameters $\alpha^{(m)}$ and $\beta^{(m)}$ and Equation 5 simplified to

$$[q - \alpha^{(m)}]^2 + C^2 [p' - \beta^{(m)}]^2 - [k^{(m)}]^2 = 0 \qquad (23)$$

for axial loading conditions (i.e., $\sigma'_x = \sigma'_z$ and $\tau_{xy} = \tau_{yz} = \tau_{zx} = 0$), where $q = (\sigma'_y - \sigma'_x)$. The yield surfaces then plot as circles in the q versus Cp' plane (referred to as the axial stress plane hereafter) as shown in Figure 1b. When the stress point reaches the yield surface $f^{(m)}$,

$$q = \alpha^{(m)} + k^{(m)} \sin\theta \qquad (24a)$$

$$p' = \beta^{(m)} + \frac{k^{(m)}}{C} \cos\theta \qquad (24b)$$

where θ is defined in Figure 1b and Equation 15 simplifies to:

$$\frac{\dot{\varepsilon}}{\dot{q}} = \frac{1}{2G} + \frac{1}{H'^{(m)}} \left[\frac{\sin\theta \, (\sin\theta + C\gamma \cos\theta)}{\sin^2\theta + \frac{2}{9} C^2 \cos^2\theta} \right] \qquad (25a)$$

$$\frac{\dot{\varepsilon}_v}{\dot{p}'} = \frac{1}{B} + \frac{1}{H'^{(m)}} \left[\frac{\frac{2C}{3} \cos\theta + A^{(m)} \sin\theta \, \frac{1}{3\gamma} (\sin\theta + C\gamma \cos\theta)}{\sin^2\theta + \frac{2}{9} C^2 \cos^2\theta} \right] \qquad (25b)$$

in which

$$\dot{\varepsilon}_v = \dot{\varepsilon}_y + 2\dot{\varepsilon}_x \qquad (26)$$

$$\dot{\varepsilon} = (\dot{\varepsilon}_y - \dot{\varepsilon}_x) \tag{27}$$

$$\gamma = \frac{\dot{p}'}{\dot{q}} \tag{28}$$

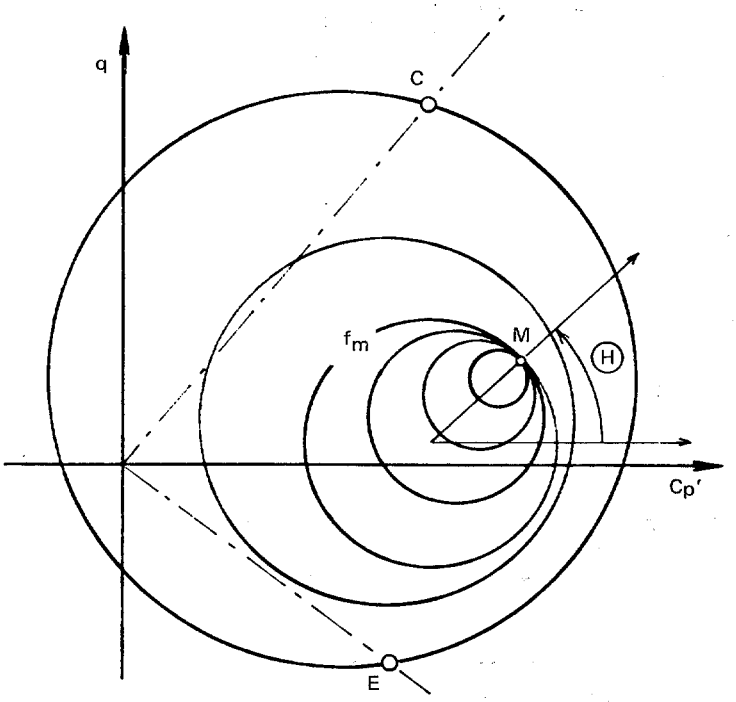

Figure 1(b). Prevost soil model - Yield surfaces in q-cp plane.

Monotonic Drained Axial Compression and Extension Soil Test Results

Let θ_C and θ_E denote the values of θ when the stress point reaches the yield surface $f^{(m)}$ in axial compression and extension loading conditions, respectively. Combining Equations 24 through 28, one finds that:

$$\tan(\theta_C + \theta_E) = \frac{-2R}{1 - R^2} \tag{29}$$

$$\frac{1}{\tan \theta_E} = \frac{3}{2C}\left[3\gamma_C\left(\frac{x_C}{y_C}\right) - A_C^{(m)}\right] \tag{30a}$$

$$\frac{1}{\tan \theta_E} = \frac{3}{2C}\left[3\gamma_E\left(\frac{x_E}{y_E}\right) - A_E^{(m)}\right] \tag{30b}$$

in which

$$R = C\,\frac{p'_C - p'_E \exp\ \lambda\left[\left(\varepsilon\frac{C}{v} - \varepsilon\frac{E}{v}\right)\right]}{q_C - q_E \exp\ \lambda\left[\left(\varepsilon\frac{C}{v} - \varepsilon\frac{E}{v}\right)\right]} \tag{31}$$

and

$$\frac{1}{x_C} = \left(\frac{p'_C}{p'_1}\right)^n \frac{\dot{\varepsilon}}{\dot{q}} - \frac{1}{2G_1} \tag{32}$$

$$\frac{1}{y_C} = \left(\frac{p'_C}{p'_1}\right)^n \frac{\dot{\varepsilon}_v}{\dot{p}'} - \frac{1}{B_1} \tag{33}$$

and similarly for x_E and y_E, where the subscript C and E refer to axial compression and extension loading conditions, respectively. Further,

$$H_C'^{(m)} = x_C \sin\theta_C\left(\frac{\sin\theta_C + C\gamma_C\cos\theta_C}{\sin^2\theta_C + \frac{2}{9}C^2\cos^2\theta_C}\right) \tag{34}$$

and, similarly, for $H_E'^{(m)}$.

The smooth experimental stress-strain curves obtained in axial tests are approximated by linear segments along which the tangent (or secant) modulus is constant. The degree of accuracy achieved by such as representative of the experimental curves is directly dependent upon the number of linear segments used. The model parameters associated with the yield surface $f^{(m)}$ are determined by the condition that the slopes $\dot{q}/\dot{\varepsilon}$ are to be the same in axial compression and extension tests when the stress point has reached the yield surface $f^{(m)}$. The corresponding values of θ_C and θ_E are determined by combining Equations 29 and 30 once a rule has been adopted for $A^{(m)}$. Once θ_C and θ_E have been determined, the model parameters associated with $f^{(m)}$ are simply obtained from Equations 24 and 25.

Monotonic Undrained Axial Compression and Extension Soil Test Results

In undrained tests, $\dot{\varepsilon}_v = 0$, and (from Equation 33) $y_C = y_E = -B_1$ in that case. The model parameters associated with the yield surface $f^{(m)}$ are again determined by the condition that the slopes $\dot{q}/\dot{\varepsilon}$ are to be the same in axial compression and extension tests when the stress point has reached the yield surface $f^{(m)}$. As previously, the corresponding values θ_C and θ_E are determined from Equations 29 and 30, in which

$$R = C \frac{p'_C - p'_E}{q_C - q_E} \tag{35}$$

Knowing θ_C and θ_E, the model parameters associated with $f^{(m)}$ are computed from Equations 24 and 25, in which $\varepsilon_v^C = \varepsilon_v^E = 0$.

Simple Shear Soil Test Results

In simple shear soil tests, $\dot{\varepsilon}_x = \dot{\varepsilon}_y = \dot{\varepsilon}_z = 0$. The necessary algebra for the determination of the model parameters is considerably simplified in that case if the elastic contributions to the normal strains are neglected. Equation 15 then yields $\sigma'_x = \sigma'_z$, and it follows that:

$$\frac{\dot{\gamma}_{xy}}{\dot{\tau}_{xy}} = \frac{1}{G} + \frac{2}{h'_m} \tag{36}$$

$$\alpha^{(m)} = (\sigma'_y - \sigma'_x) \tag{37}$$

$$\beta^{(m)} = \sigma'_y - \frac{2}{3}(\sigma'_y - \sigma'_x) \tag{38}$$

$$k^{(m)} = \sqrt{3\ \tau_{xy}} \tag{39}$$

The model parameters associated with the yield surface $f^{(m)}$ are then simply determined from the above equations and an incremented linear representation of the shear stress-strain curves obtained from a simple shear test. Note that the sole use of simple shear test results does not allow the determination of the parameters $B'^{(m)}$ and $A^{(m)}$. On the other hand, it is apparent from Equations 36 and 39 that the degradation of the mechanical properties of the material under cyclic shear loading conditions; i.e., $k^{(m)}(\bar{e})$ and $h'^{(m)}(\bar{e})$ with

$$\bar{e} = \int \left(\frac{2}{3} \dot{\underset{\sim}{e}}' : \dot{\underset{\sim}{e}}' \right) \qquad \dot{\underset{\sim}{e}} = \dot{\underset{\sim}{\varepsilon}} - \frac{1}{3} (\mathrm{tr}\, \dot{\hat{\underset{\sim}{\varepsilon}}}) \underset{\sim}{1} \tag{40}$$

where the integration is carried along the strain path, are most conveniently determined from the results of cyclic strain-controlled simple shear tests

$$(\bar{e} = \int \frac{1}{\sqrt{3}} \left| \dot{\gamma} \right| \text{ in that case}).$$

This is explained and further discussed in Reference 8. The above material is based directly on Prevost (Ref 9).

SCALING DATA FOR DEPTH

Based on limited data, it has been found reasonable to scale by the ratio of average confining stress levels. The elastic shear modulus, the initial elasto-plastic shear modulus, and the elastic bulk modulus are scaled by the square root of the stress ratio. The bulk exponent is not scaled. Initial stress components are scaled by the ratio. The softening parameters -- delta, delta ultimate, and the yield surface axis ratio -- are scaled by the stress ratio. The size of the yield surface is scaled by the stress ratio. The elasto-plastic shear and plastic bulk moduli are scaled by the square root of the stress ratio; the degree of nonassociativity is not scaled.

Anisotropic consolidation can also be treated by shifting the ellipses. It is assumed that isotropic data are used and the J_1 value is maintained constant, as follows:

$$J_1 = \sigma_v + 2\,\sigma_H \tag{42}$$

$$J_1 = (1 + 2\,k_o)\,\sigma_v \tag{43}$$

$$\text{Shift}\sqrt{J_2} = \frac{\sigma_v - \sigma_H}{\sqrt{3}} \tag{44}$$

$$\text{Shift}\ J_2 = \frac{(1 - k_o)}{\sqrt{3}}\,\sigma_v \tag{45}$$

$$\text{Shift}\ J_2 = \left(\frac{1 - k_o}{3}\right)\left(\frac{J_1}{1 + 2\,k_o}\right) \tag{46}$$

The new values for σ_v and σ_H are

$$\sigma_v = \frac{J_1}{1 + 2\,k_o} \tag{47}$$

$$\sigma_H = \frac{J_1 - \sigma_v}{2} \tag{48}$$

$$F\,(\sigma',\ \eta) = 0 \tag{49}$$

where J_1 is from the isotropic test and K is the coefficient of lateral earth pressure at rest.

It is suggested that data be first scaled to the correct J_1 and then shifted to anisotropic conditions.

DYNAFLOW FINITE ELEMENT CODE

The DYNAFLOW Program (Ref 10) is a finite element program intended for the static and transient analysis of linear and nonlinear two- and three-dimensional problems. The analysis capabilities include the following:

Static - Nonlinear elliptic boundary value problems with two degrees-of-freedom per two-dimensional node and three degrees-of-freedom per three-dimensional node.

Diffusion - Nonlinear parabolic boundary value problems with one additional degree-of-freedom for the phase porous fluid pore pressure.

Dynamic - Nonlinear hyperbolic boundary value problems with two additional degrees-of-freedom for the phase porous fluid.

The program incorporates the full Prevost model for nonlinear effective stress analysis. The material model produces a nonsymmetric stiffness matrix. Solution techniques employed allow for implicit, explicit, and implicit/explicit matrix solution.

For static analysis, an incremental predictor-corrector load-step procedure is utilized. The term $\alpha = 1$ is utilized and associates the midpoint of the load (time) interval to the predictor phase and achieves second-order accuracy.

For parabolic analysis diffusion problems, a Newton-Raphson iterative procedure is utilized. Unconditional stability is achieved for $\alpha \geq 1/2$, and a value of $\alpha = 1$ is recommended to maximize high frequency numerical dissipation. For explicit elements, a time-step restriction occurs:

$$\Delta t < \frac{2}{\lambda}$$

where λ is equal to the largest eigenvalue associated with the problem.

For hyperbolic analysis, an implicit-explicit predictor-multicorrector algorithm is used. Stability is achieved when $\alpha \geq 1/2$. Implicit elements are unconditionally stable if $\beta \geq \alpha/2$. Explicit elements have a time-step restriction:

$$\Omega < 2\ (1 - \xi)/(\alpha + 1/2)$$

where Ω is $\omega\Delta t$, and ξ is the modal viscous damping. When $\alpha = 3/2$ and $\beta = 1$, the dissipative properties of the algorithm damp all dynamic transient phenomena and permit static solution.

Solution of the porous media problem requires defining boundary conditions for the fluid as would occur in a conventional seepage analysis. This is accomplished by defining the third and fourth degrees of freedom, the x- and y-fluid velocities.

A standard 4-node element is used. To treat the initial pore fluid incompressibility, it is suggested that one-point Gaussian quadrature be used for the volumetric stiffness numerical integration and that two-by-two Gaussian quadrature be used for the deviatoric stiffness numerical integration. Use of elastic-plastic equations of the above type in analysis of boundary value problems requires that an efficient, "sturdy," and accurate numerical integration procedure for the plasticity equations at the stress point level be available. Substantial efforts have thus been devoted to designing a computational procedure with the best balance of accuracy and computation speed. The integration algorithm presently used in the stress routine is a generalization of the conventional radial return technique.

MODEL EVALUATION

Cohesive Soils

The soil data used in this section is part of the data which were collected by the organizing committee of the NSF/NSERC North American Workshop on plasticity and generalized stress-strain applications in

soil engineering held May 28-30, 1980 at McGill University, Montreal, Canada and reported by Prevost (Ref 9). Laboratory axial test data on a laboratory-prepared Kaolinite clay had then been provided to Prevost. Predictions about the constitutive behavior of the soil subjected to loading stress paths not identified in the data had been requested by the organizing committee. This section describes the test results by Prevost and their analysis and compares the model predictions with observed behavior in the tests.

The experimental tests had been conducted on cylindrical samples in a torsional shear testing device. All samples had first been K_0-consolidated with a cell pressure of 58 psi and a backpressure of 18 psi; in other words, the excess axial load necessary for K_0-consolidation was then released. All the tests were stress-controlled and performed under constant volume conditions (i.e., undrained).

Figure 2 shows in dashed lines the experimental results obtained in conventional undrained monotonic axial compression/extension soil tests and in solid lines the design curves used to determine the model parameters for that clay. Note that some data close to failure have been ignored in selecting the design curves because they are not consistent with the rest of the data. This inconsistency may be due to experimental difficulties in capturing failure states in stress-controlled testing devices.

Figure 3 shows model predictions for a shear test in which the major principal stress is inclined at $\theta = 15$ degrees, relative to the vertical axis of the soil specimen (Ref 9). Figure 3 also shows a comparison between predicted and observed behavior of the soil in these tests. Note that all the model predictions agree well with the experimental test results (Ref 9).

Cohesionless Soils

The model developed by Prevost is able to represent drained or undrained test data. Figures 4 and 5 show comparison of drained test data for the Silica sand and Banding sand. Figure 6 shows a comparison of undrained test data based on the undrained parameters of the Banding sand.

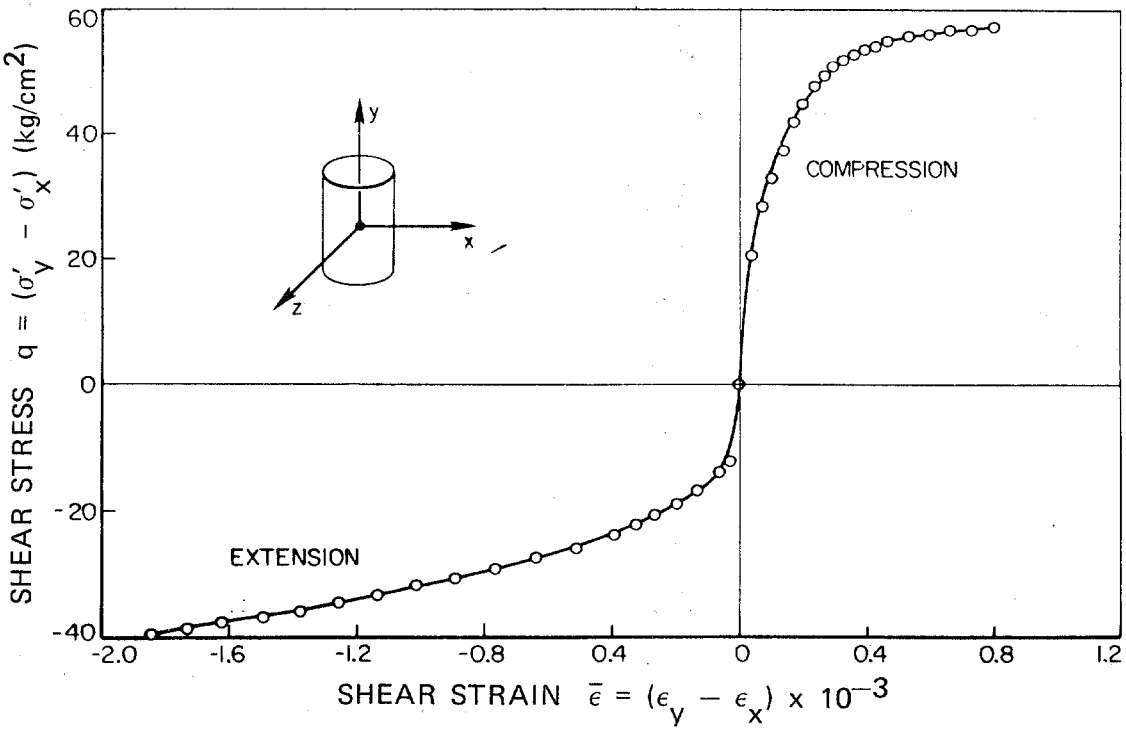

(a) Shear stress versus shear strain.

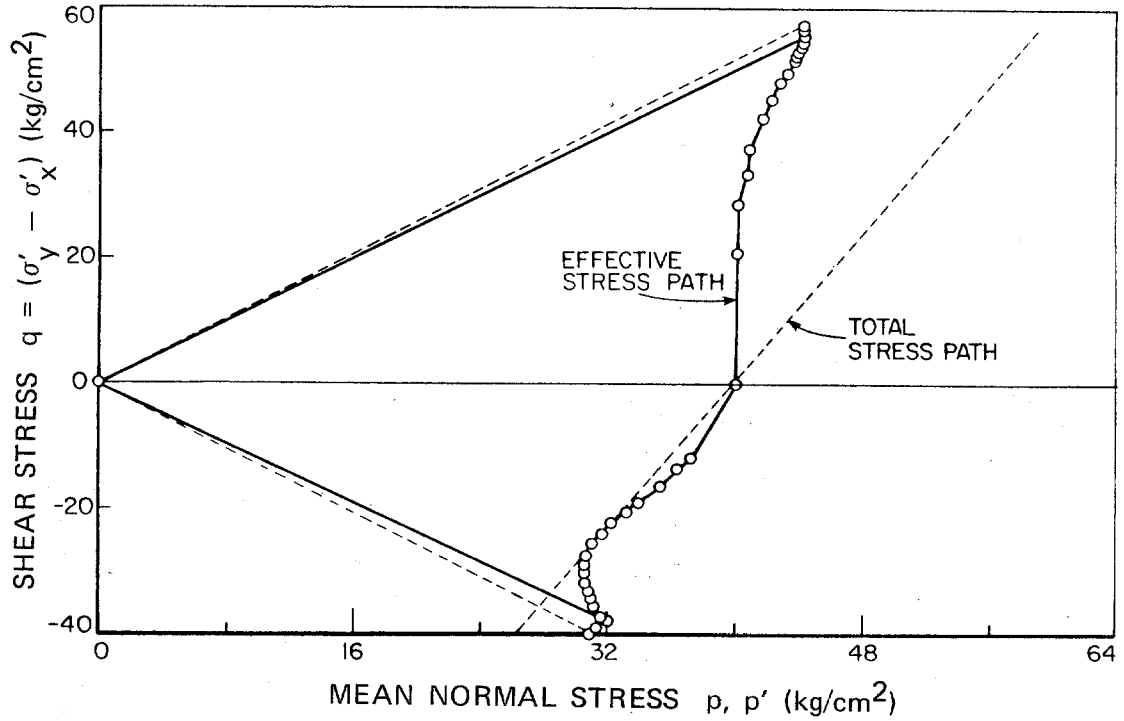

(b) Shear stress versus mean normal effective stress.

Figure 2. Kaolinite clay - undrained axial soil test results.

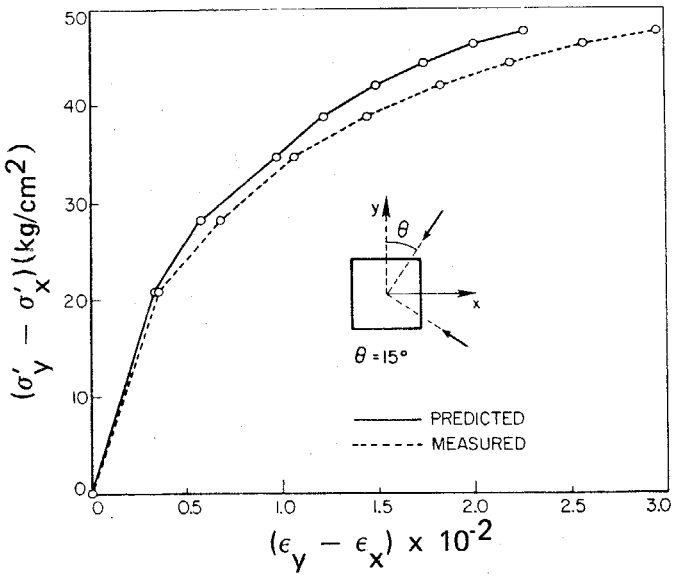

(a) Stress difference versus strain difference (x-y) ($\sigma_x - \sigma_y$) versus ($\epsilon_x - \epsilon_y$).

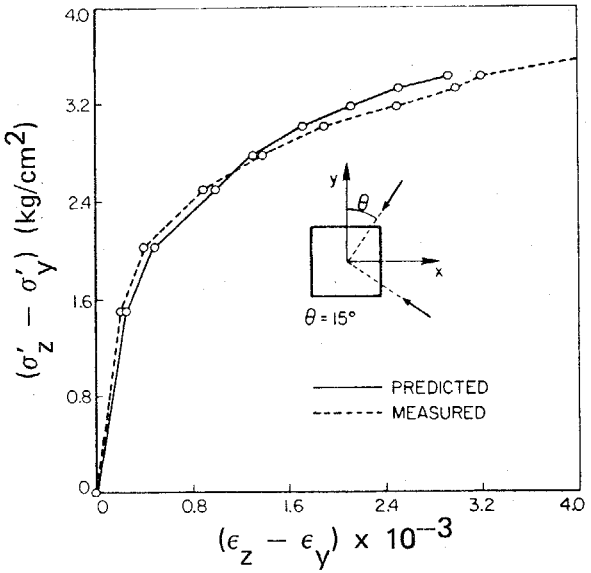

(b) Stress difference versus strain difference (y-z) ($\sigma_y - \sigma_z$) versus ($\epsilon_y - \epsilon_z$).

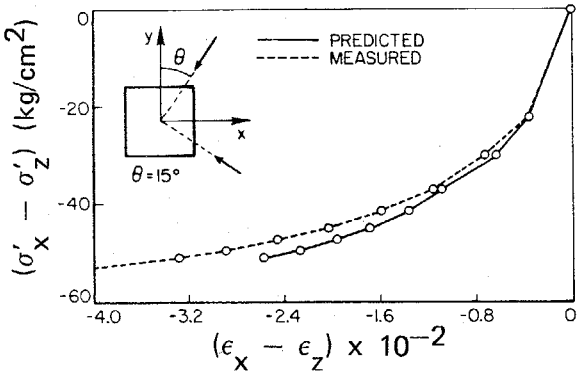

(c) Stress difference versus strain difference (x-z) ($\sigma_z - \sigma_x$) versus ($\epsilon_z - \epsilon_x$).

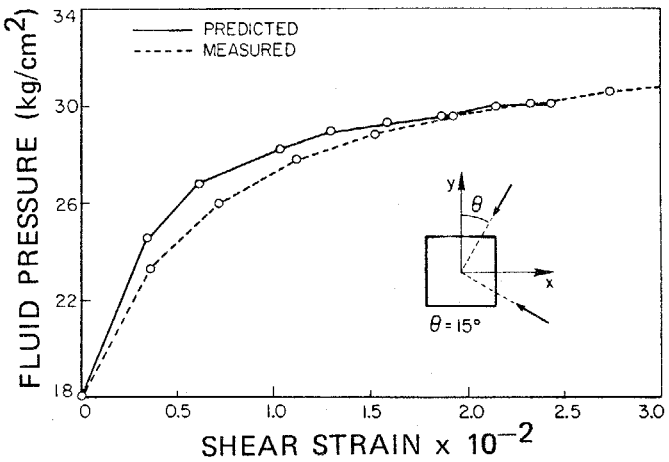

(d) Fluid pressure versus shear strain.

$$\frac{1}{2}\sqrt{(\epsilon_x - \epsilon_y)^2 + (\epsilon_y - \epsilon_z)^2 + (\epsilon_z - \epsilon_x)^2}$$

Figure 3. Kaolinite clay - undrained shear test with θ = 15°.

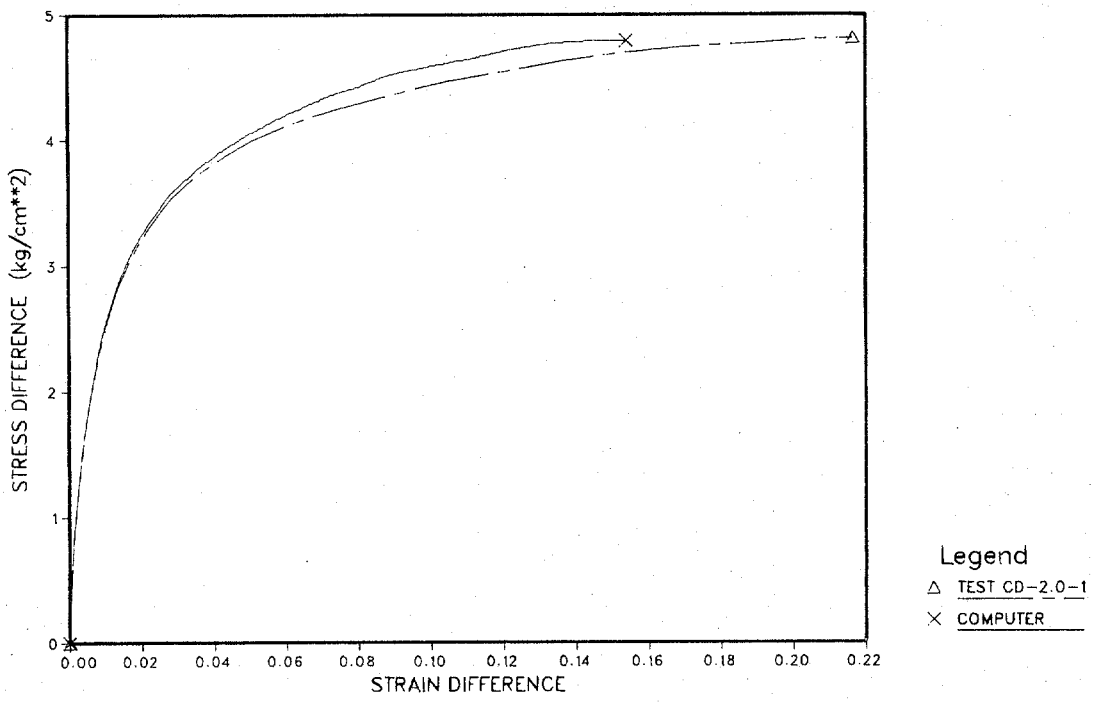

(a) Stress-strain.

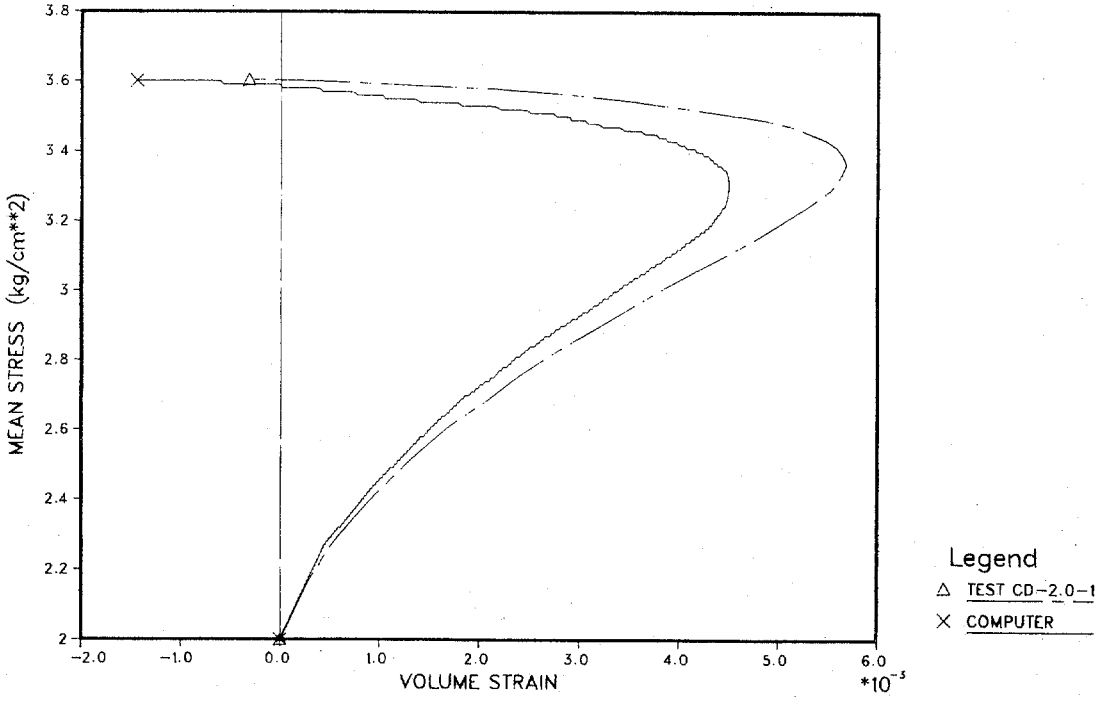

(b) Volume-strain.

Figure 4. Silica sand, drained compression.

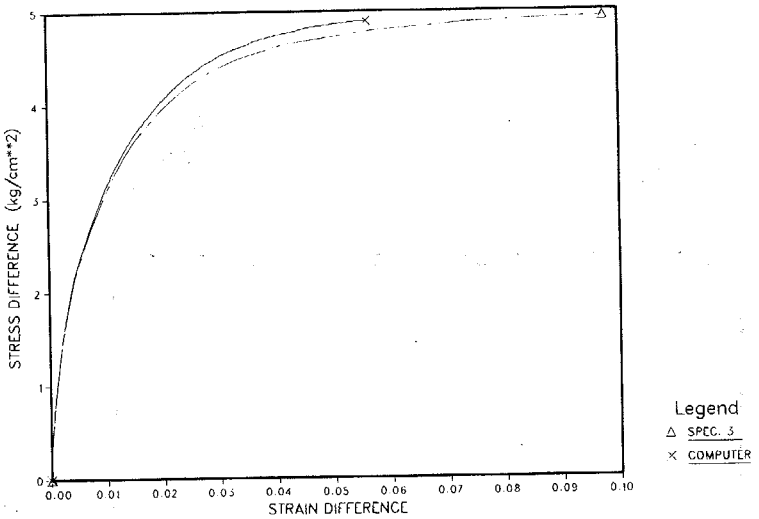

(a) Stress-strain.

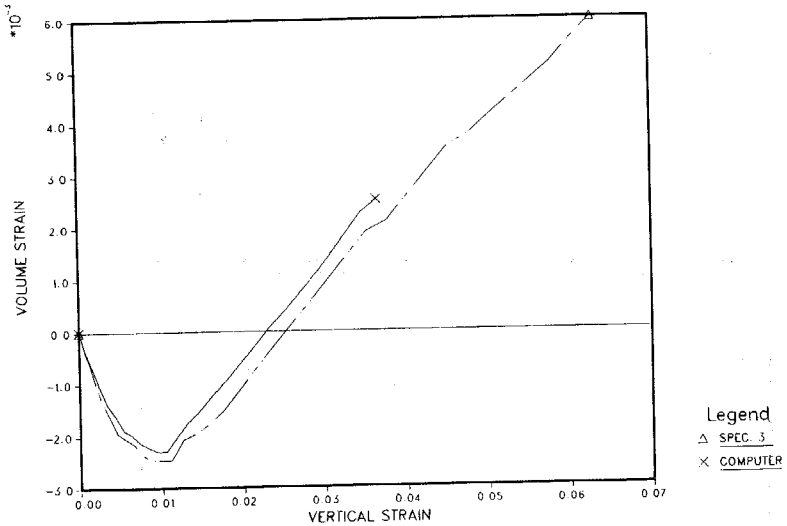

(b) Volume-strain.

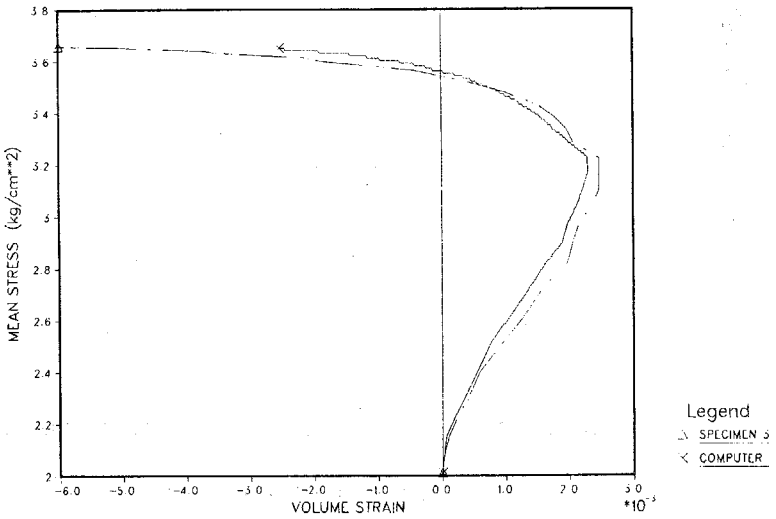

(c) Mean stress-volume strain.

Figure 5. Banding sand, drained compression.

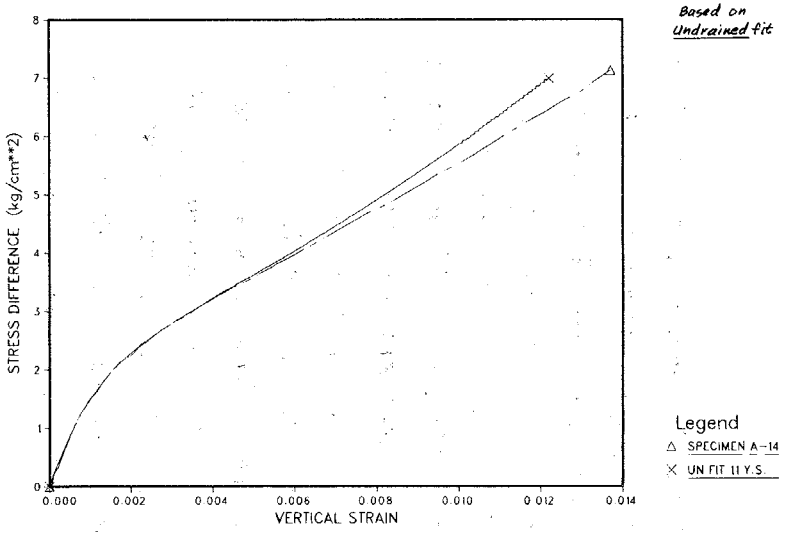

(a) Stress-strain.

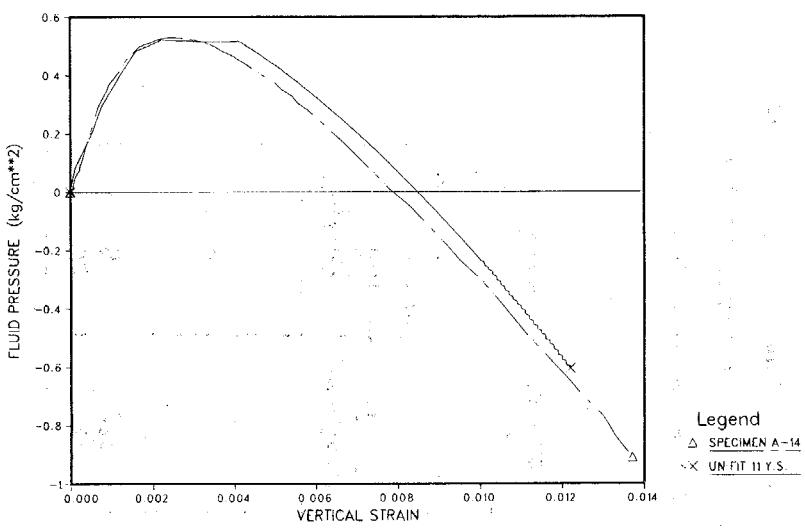

(b) Pore pressure.

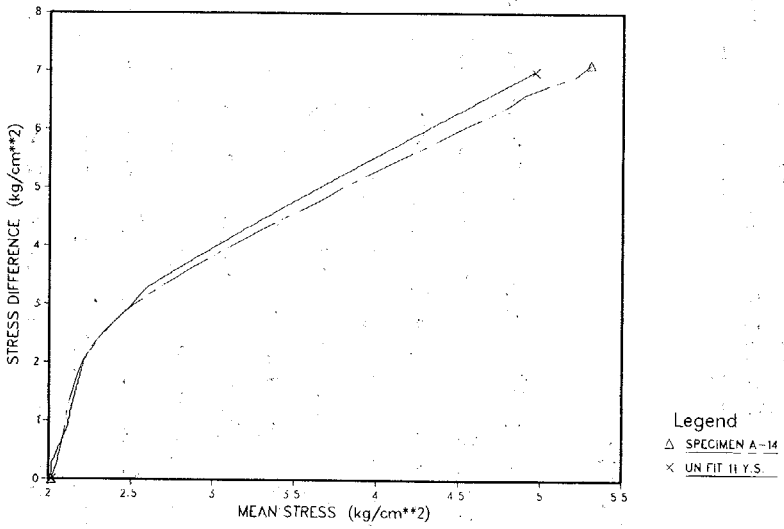

(c) Stress difference - mean stress.

Figure 6. Banding sand, undrained compression.

Typical liquefaction behavior is shown in Figure 7 where cyclic degradation and pore pressure buildup can be seen. Typical test results and model comparison are shown in Table 1 for the Banding sand.

Table 1. Results and Comparisons of Cyclic Tests With Undrained Banding Sand

Tests	Amplitude	No. of Cycles to Liquefaction	
		Measured	Predicted
Stress-controlled			
Cyclic compression	-1.20 kg/cm^2	4	2.5
Cyclic extension	+1.20 kg/cm^2	2	2
Strain-controlled			
Cyclic compression	-0.0013	≅20	20
Cyclic extension	+0.0013	≅24	20

SOIL COLUMN STUDY

A soil column approximately 12 meters in depth was studied; Figure 8 shows the mesh simulating infinite layers. Since the mesh is only one element wide, wave reflections are not possible. Vertical displacements are restrained; horizontal forces are applied to equilibrate gravity effects; and horizontal fluid flow is restrained. A sinusoidal excitation of 0.102g was applied to the base. Figure 9 shows the acceleration response, illustrating soil attenuation of the induced base motion which would be expected for loose soil. Figure 10 shows the variation of vertical effective stress with time at four depths. The stress decreases with increasing pore pressure. This shows an increase in vertical effective stress at the point in time that drainage begins. Figure 11 shows the pore pressure and Figure 12 the shear stress at the four depths. The expected buildup of pore pressure and drainage of near-surface layers are illustrated in the results of this case study.

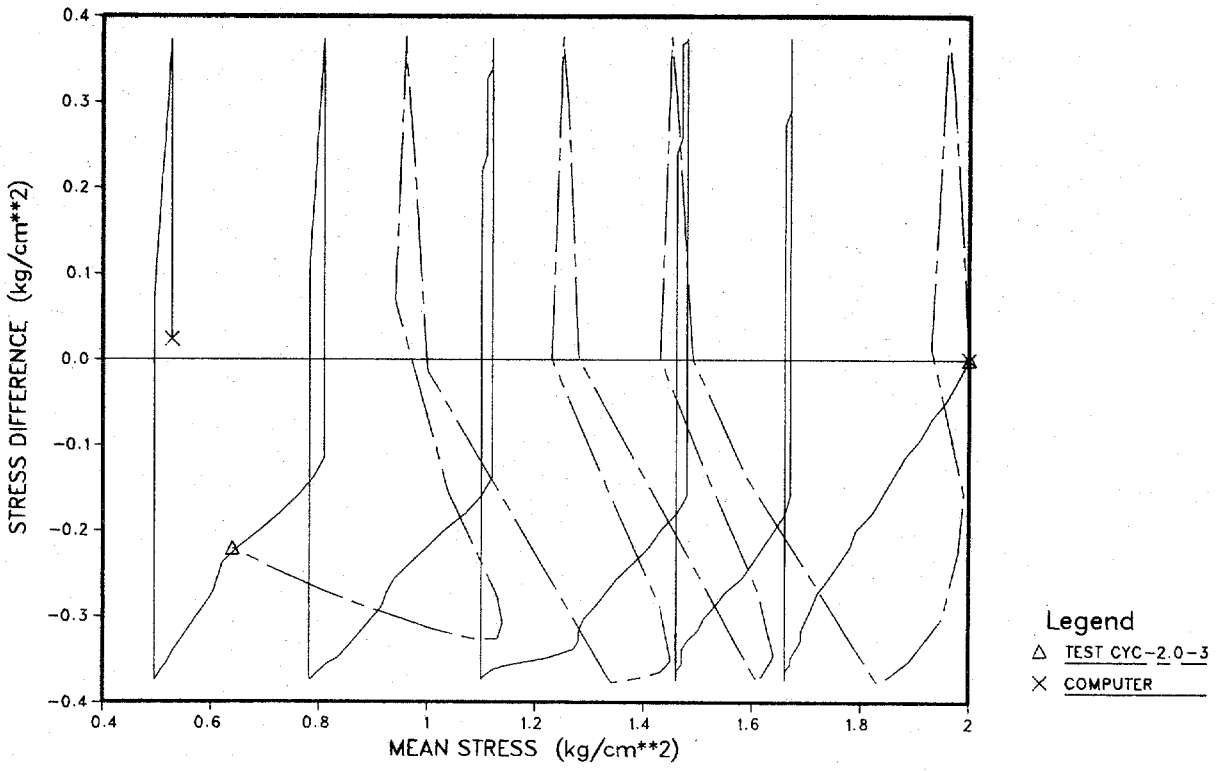

(a) Stress path.

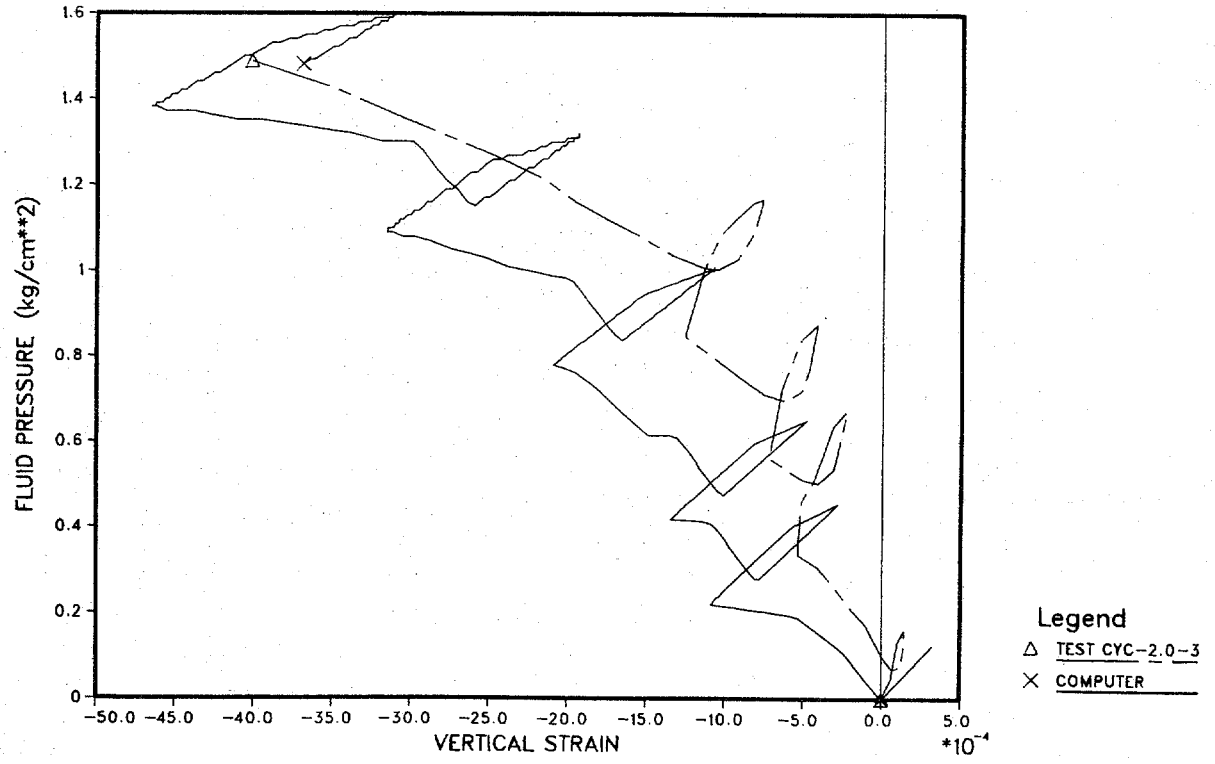

(b) Pore pressure.

Figure 7. Silica sand, undrained cyclic.

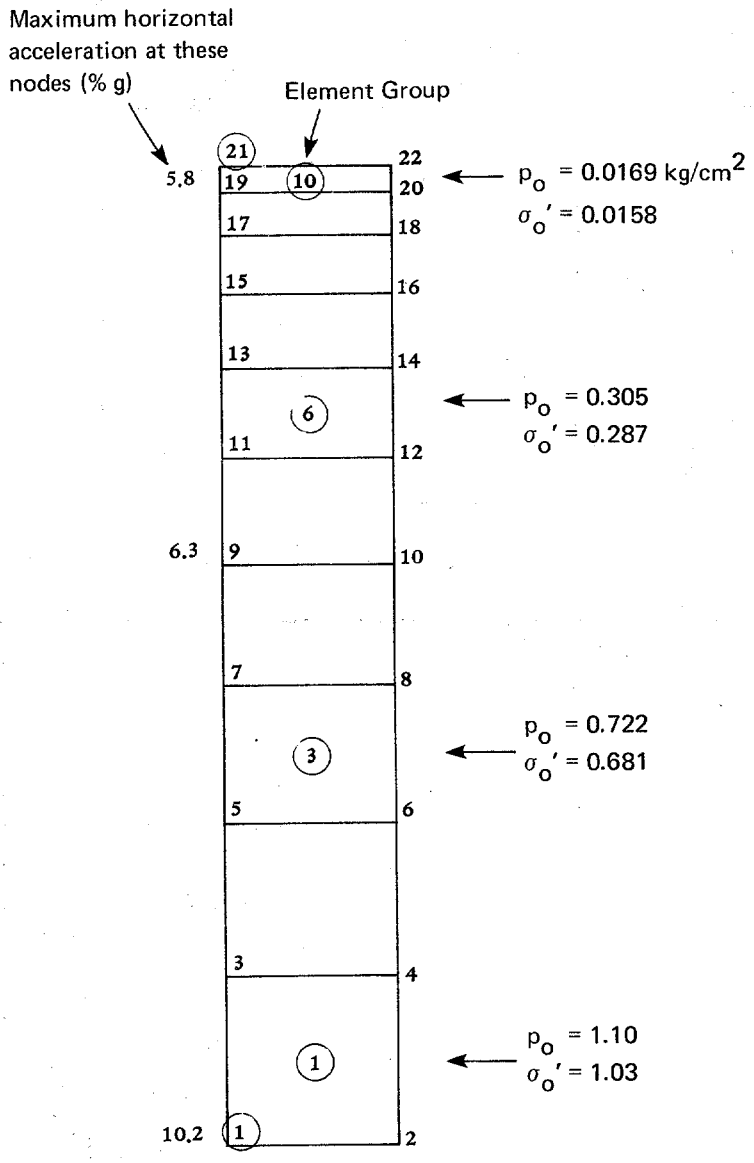

Figure 8. Soil column mesh.

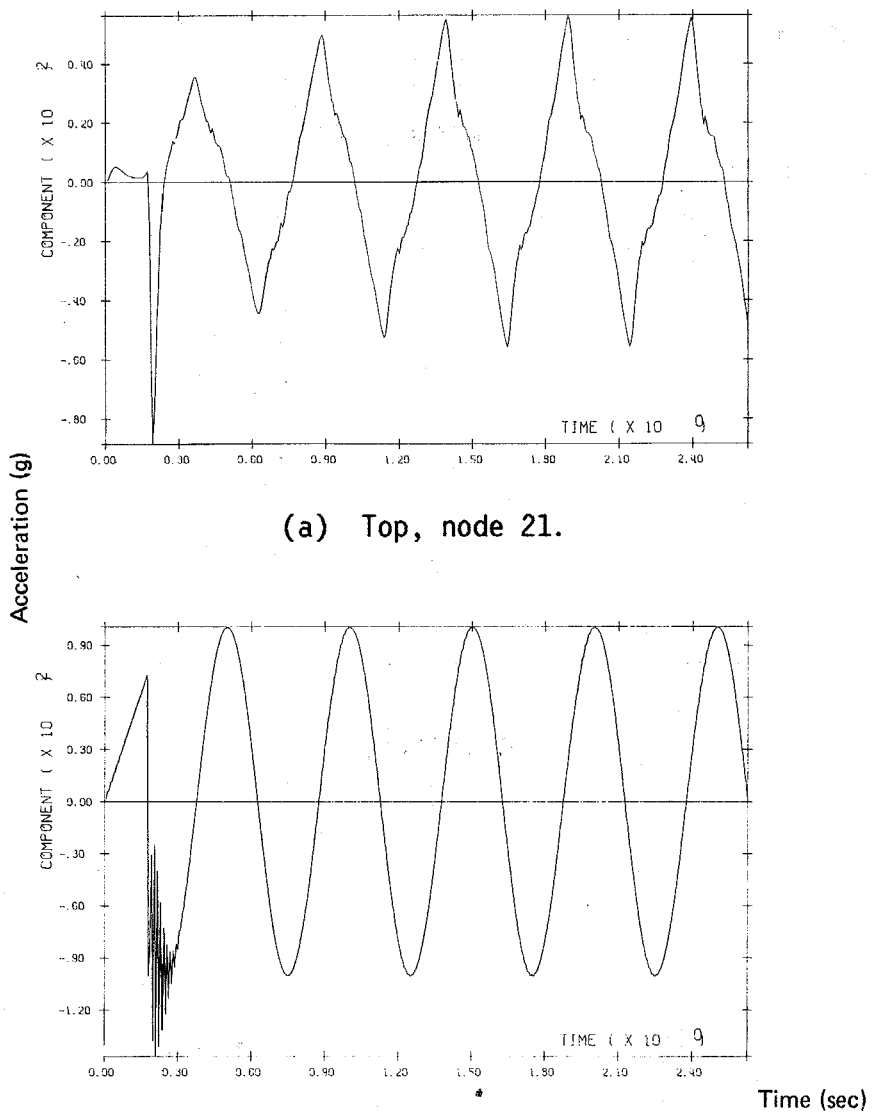

(a) Top, node 21.

(b) Node 9.

(c) Base, node 1.

Figure 9. Acceleration response.

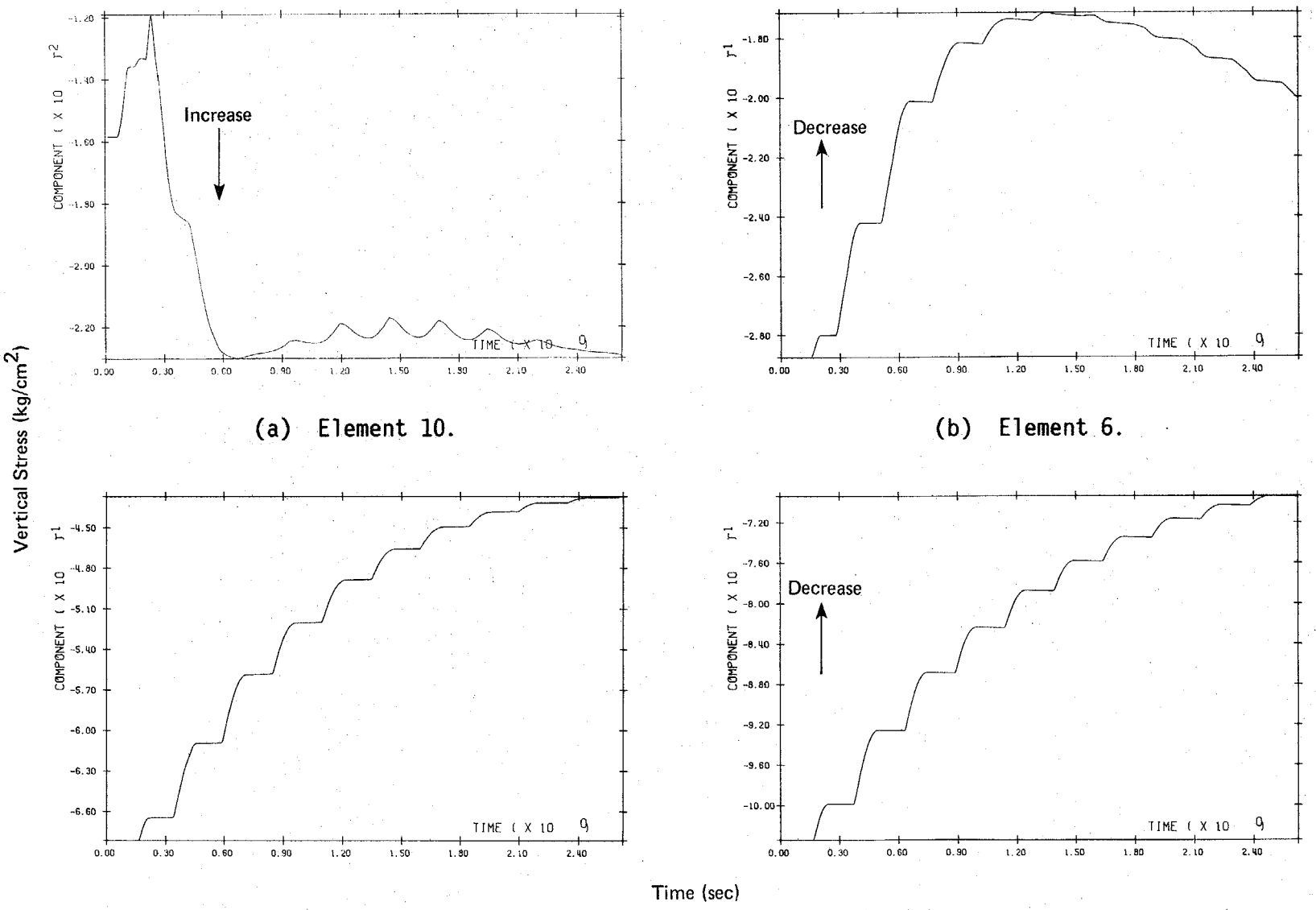

(a) Element 10.

(b) Element 6.

(c) Element 3.

(d) Base, Element 1.

Figure 10. Vertical stress.

Figure 11. Pore fluid pressure.

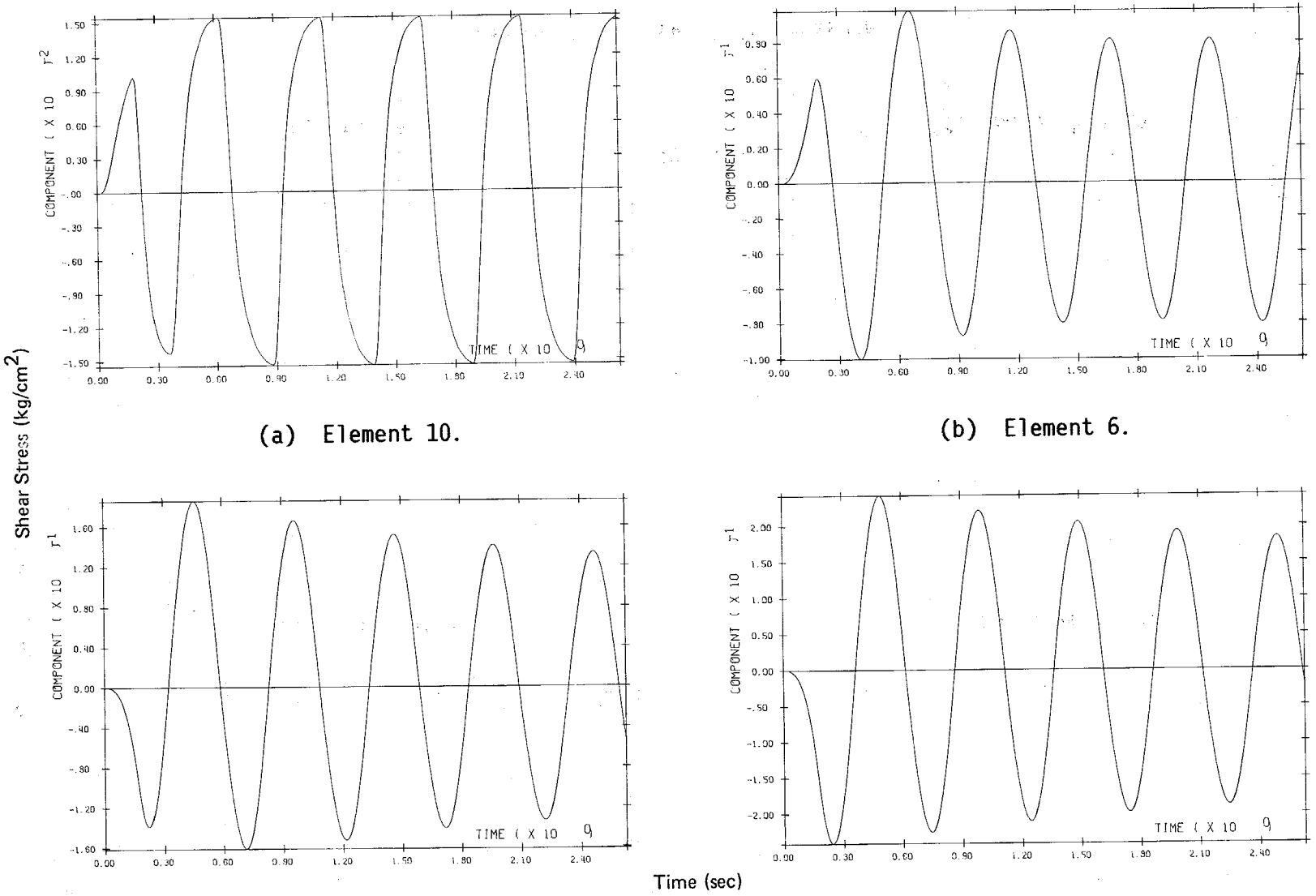

Figure 12. Shear stress.

SOIL-STRUCTURE PROBLEM

Static Analysis

To illustrate a typical soil-structure problem, beam elements were used to represent a structural frame on a soil foundation. Figure 13 shows the mesh. The structure was embedded in the soil resting on the top of the fourth soil layer. Figure 14 illustrates the coupling of the beam elements to the soil field using contact elements. Contact elements were used at the base to permit change from the third degree-of-freedom in the quadrilateral elements (pore pressure) to the third degree-of-freedom in the beam (rotation). Vertical and horizontal contact elements were used along the side of structure -- vertical to allow for frictional forces and horizontal to permit contact/separation with deformation. Figure 15 shows the deformed mesh at steps 5 and 15 of loading. Figure 16 shows the vector velocity at steps 5 and 15. Figure 17 shows the stress path in the element beneath the corner of the structure. Note that as the load is applied, the stress builds up gradually; and, as shown in Figure 18, most of the load is carried by pore pressure. As the pore pressure dissipates (Figure 18a), the effective stress in the soil increases, and deformation also increases (Figure 18b). The high loading produces localized yielding. This is evident in the deformed mesh plots and vector velocity plots (Figures 15 and 16), which show (to an exaggerated scale) the failure of the soil near the structure. Figure 19 shows the pore pressure contours. Pore pressure is at maximum near the lower left corner of the structure because drainage is permitted only at the surface.

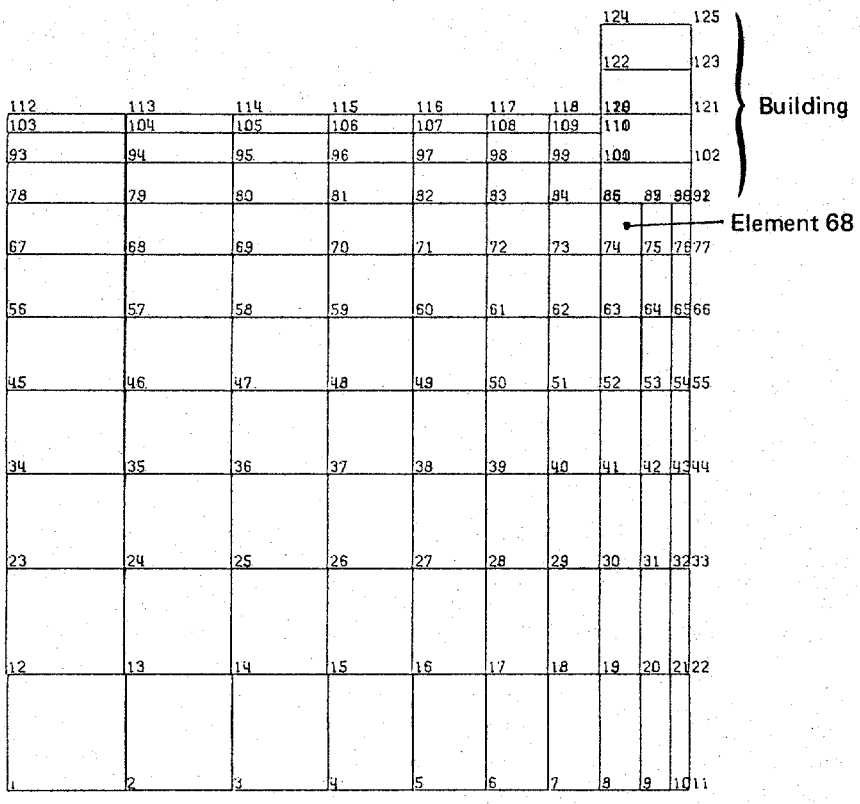

Figure 13. Undeformed mesh - two-dimensional soil field with building.

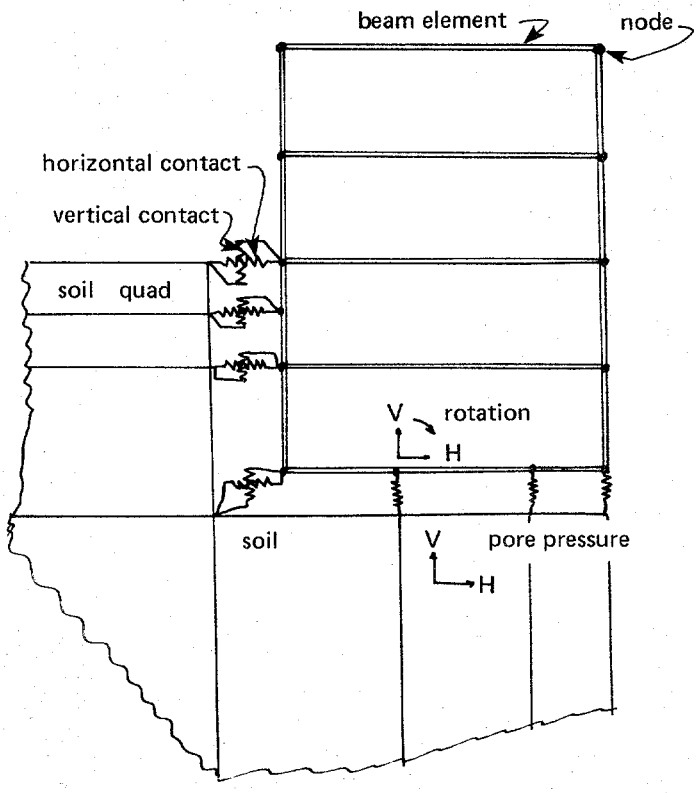

Figure 14. Contact elements at structure interface.

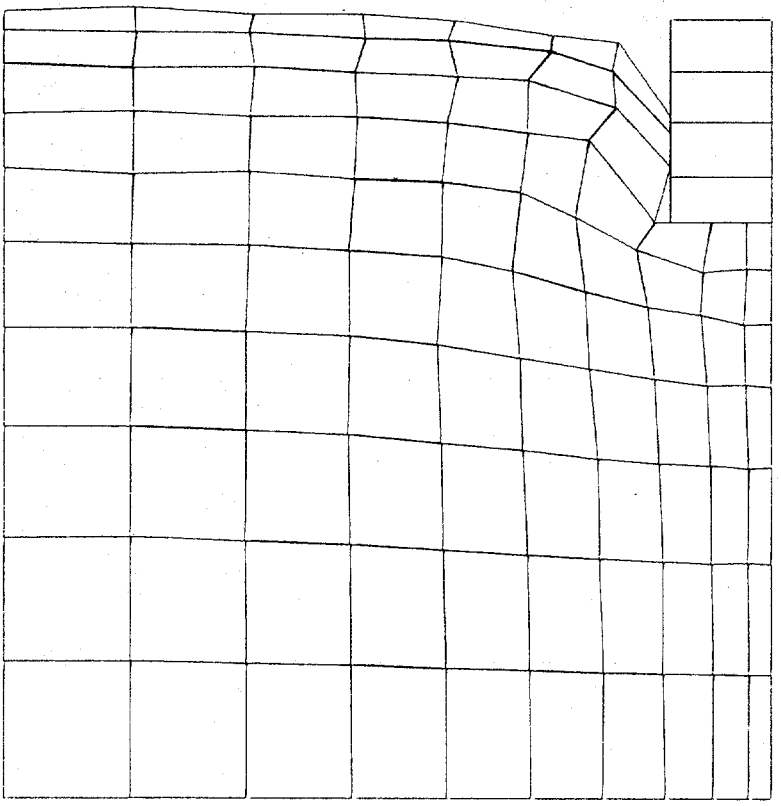

(a) Step 5.

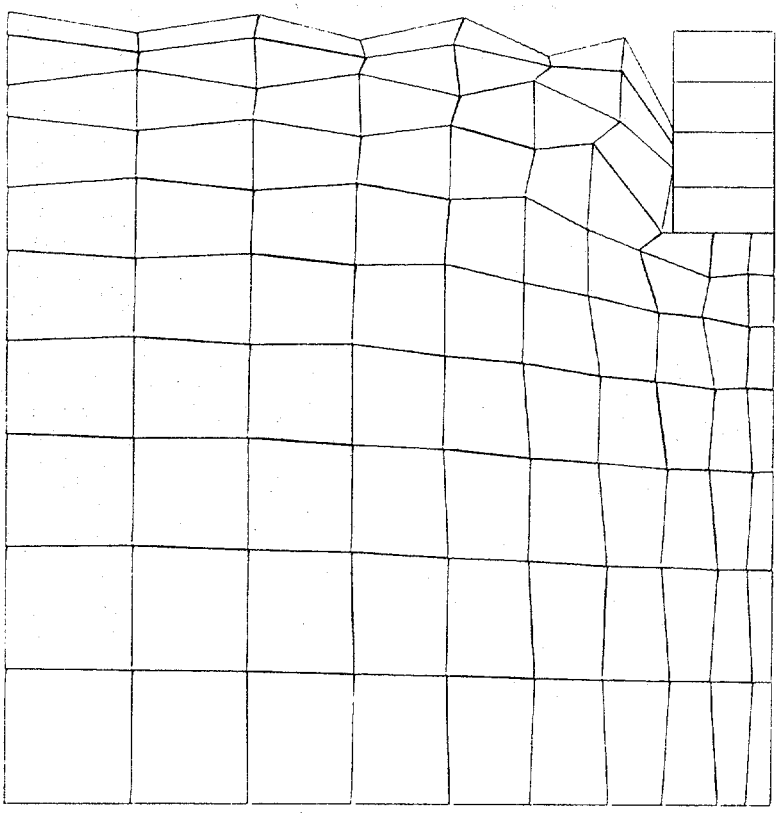

(b) Step 15.

Figure 15. Deformed mesh.

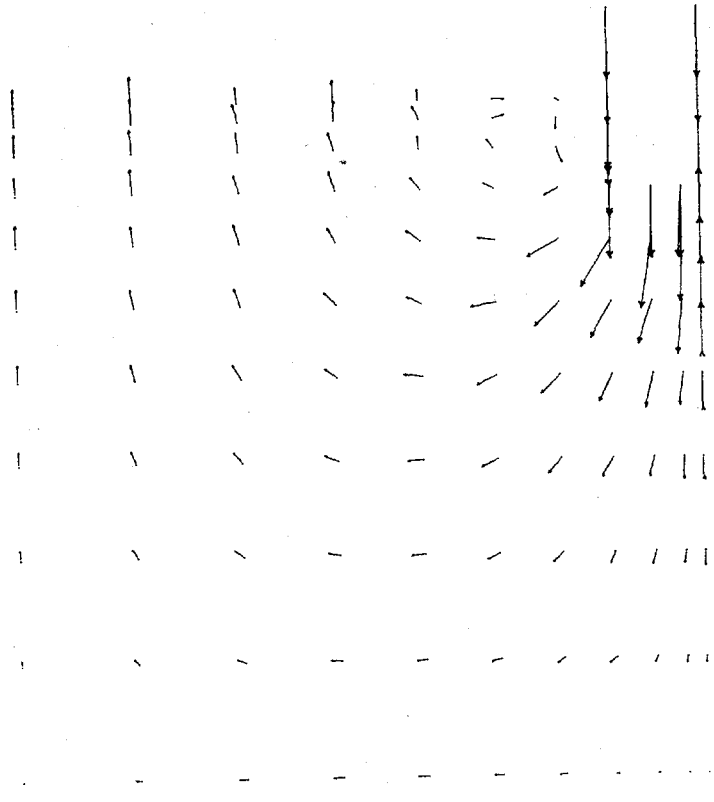

(a) Step 5.

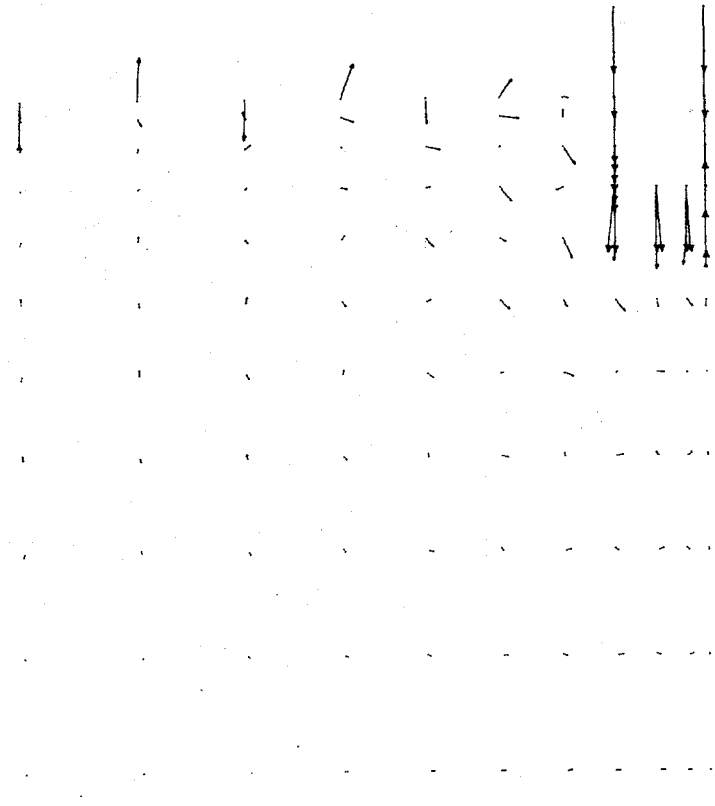

(b) Step 15.

Figure 16. Vector velocity.

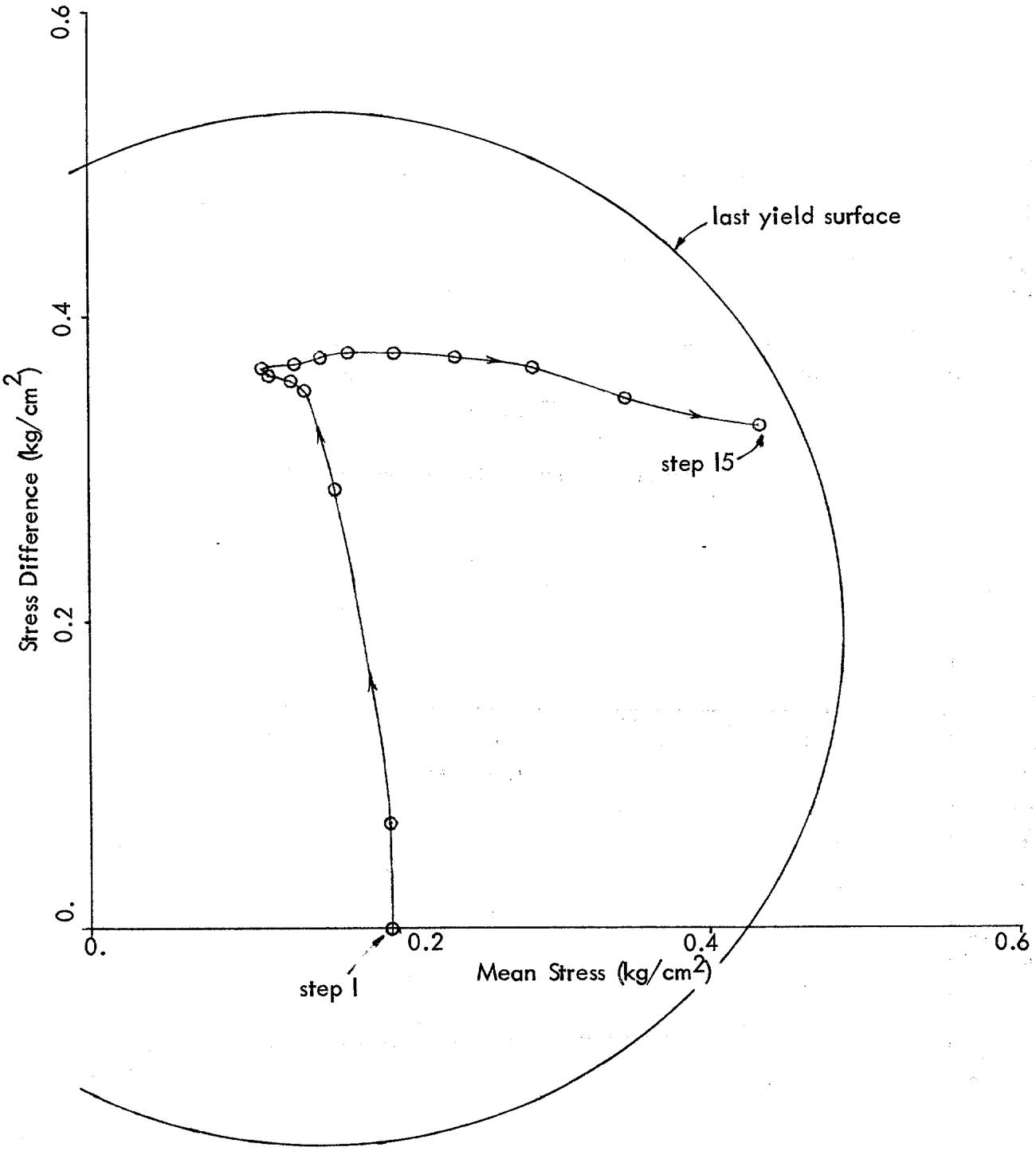

Figure 17. Effective stress path - two-dimensional soil field with building (Element 68).

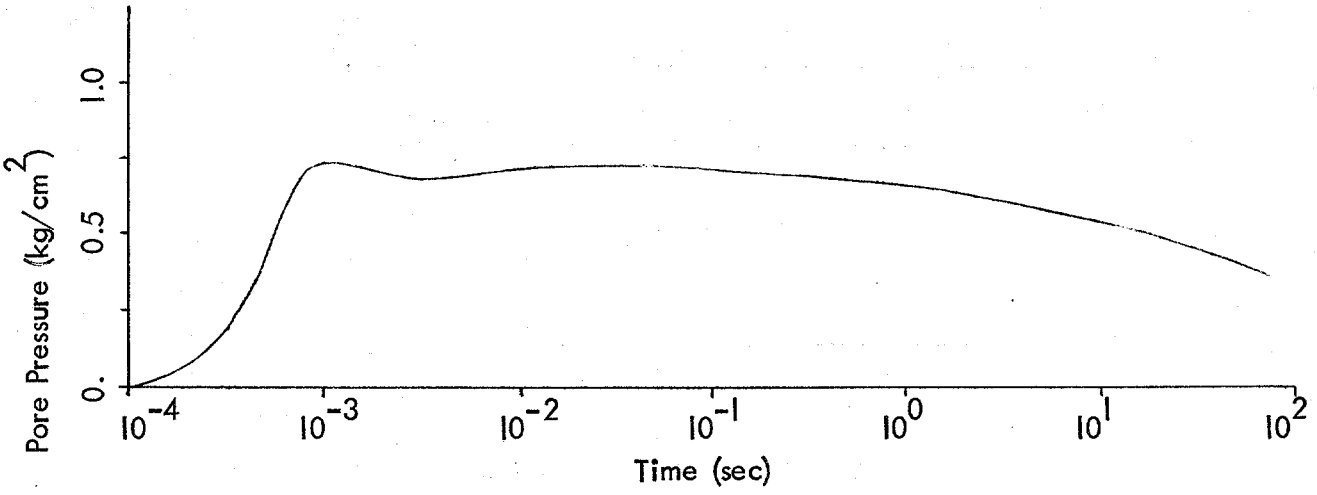

(a) Pore pressure history (Element 68).

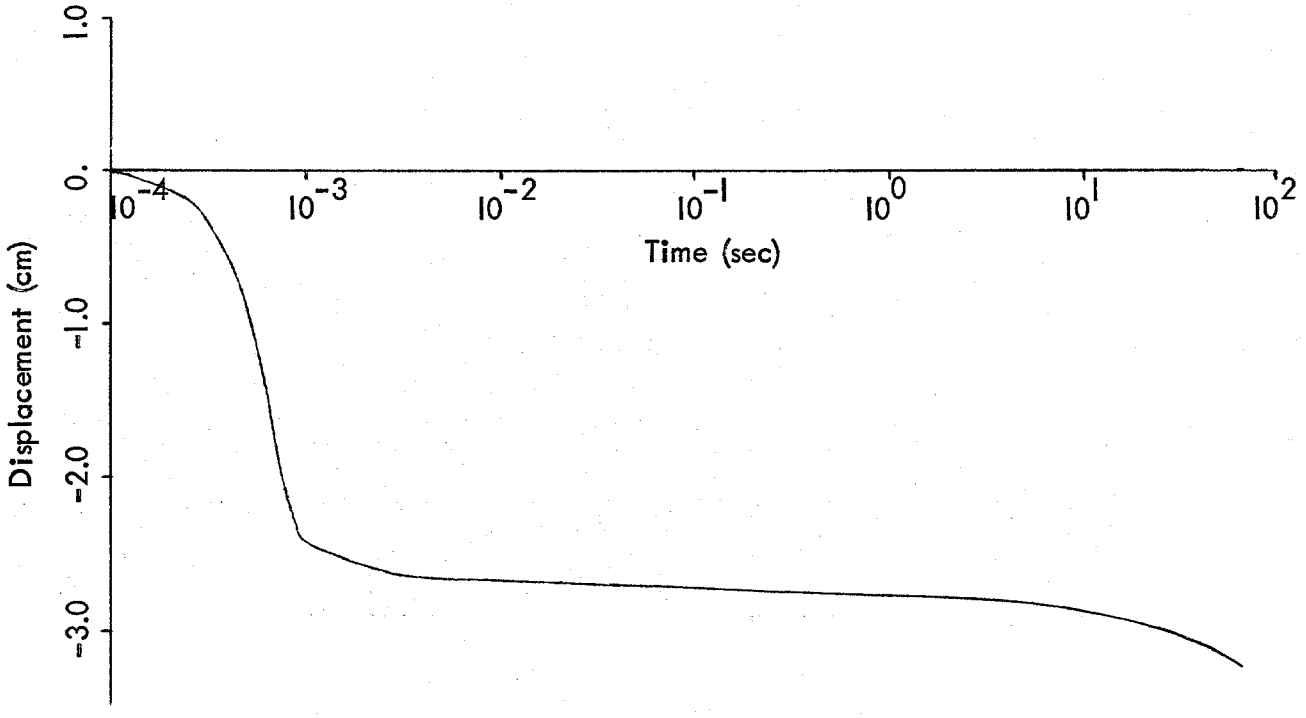

(b) Displacement history (Node 85).

Figure 18. Two-dimensional soil field with building.

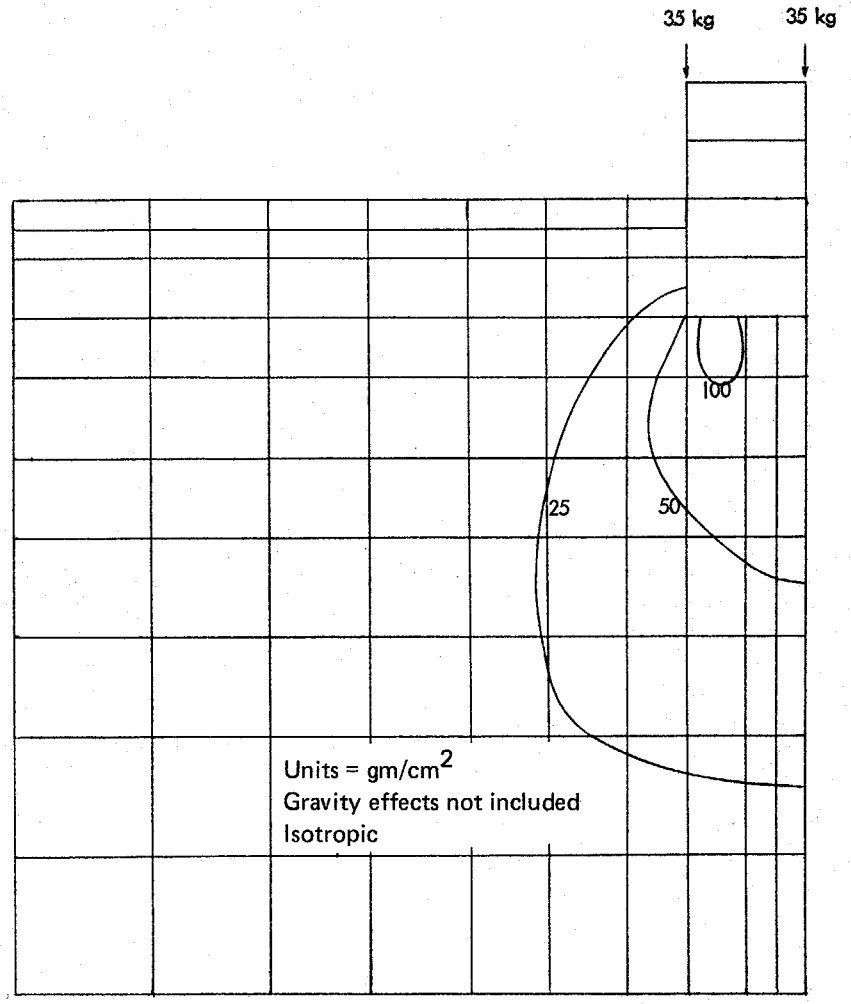

(a) Step 2.

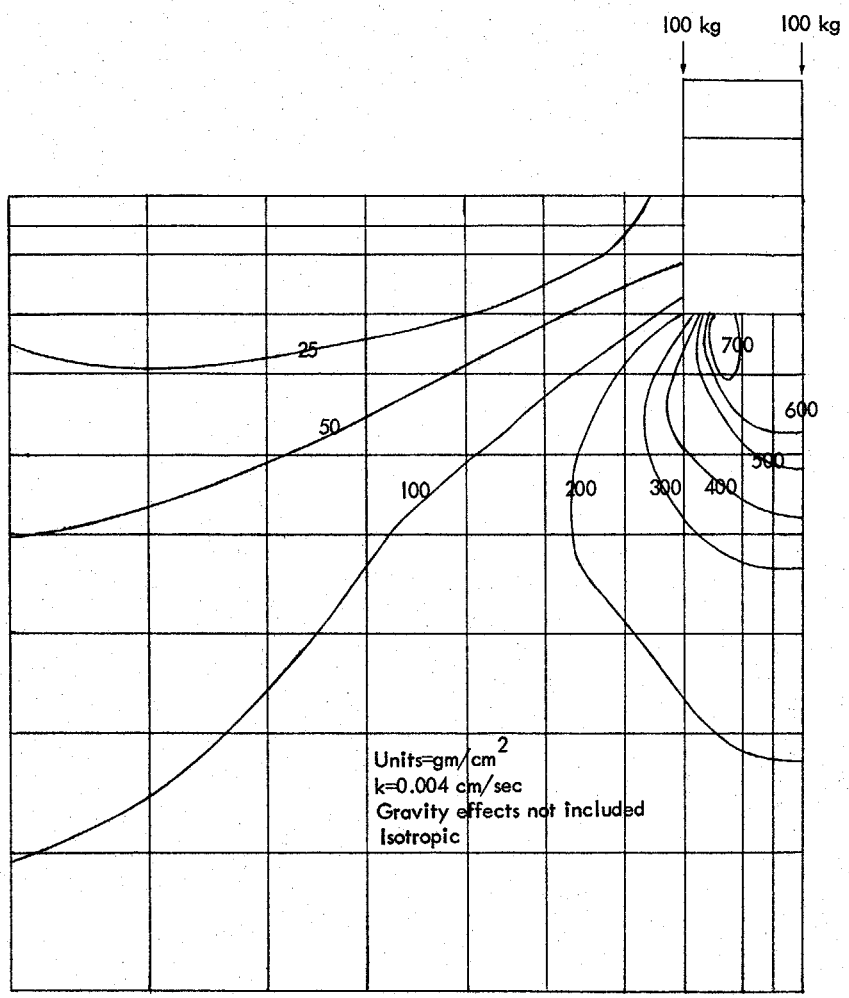

(b) Step 4.

Figure 19. Pore pressure contours - Prevost soil model.

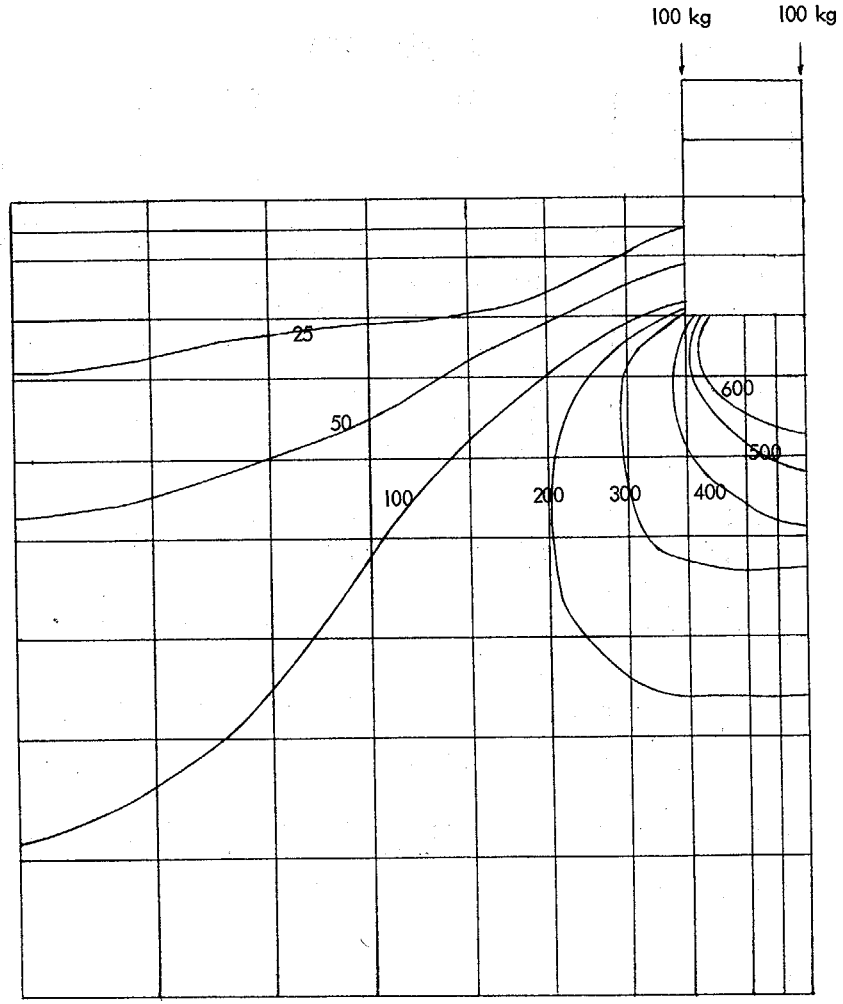

(c) Step 10.

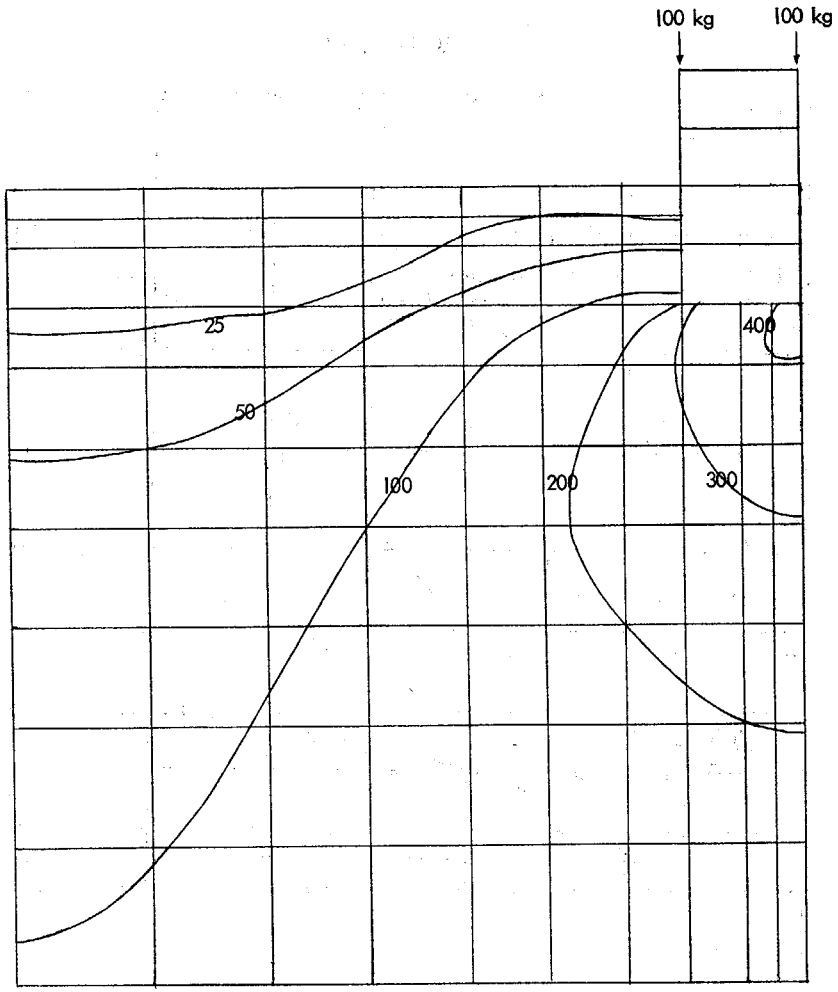

(d) Step 14.

Figure 19. Continued.

Dynamic Analysis

It was of interest to analyze a two-dimensional model of a structure on soil subject to horizontal shaking motion (see Figure 20). A full mesh is utilized to capture asymmetric effects, such as building rocking. The model is composed of 120 quadrilateral elements, 43 beam elements, and 33 nodal contact elements. Five soil layers were used, each composed of a 14-surface model scaled to each layer's center. The Prevost model incorporates an initial stress as a model parameter; gravity was applied from time equal to 0 to offset the initial material stress. The building weight was applied slowly in five steps, and pore pressures from this load were allowed to dissipate to produce an equilibrium static condition as the starting point for dynamic excitation. This solution was performed using the hyperbolic option with integration parameters $\alpha = 1.5$ and $\beta = 1.0$ to produce a highly damped "static" condition. Thus, the first five steps were a static analysis. The solution utilized four degrees-of-freedom per node. The vertical side boundaries were free boundaries for translation, having static gravity nodal forces loads and fluid nodal forces applied horizontally to maintain equilibrium and having nodal dampers to simulate nonreflecting boundaries. The water table was at the ground surface, where drainage was permitted. Figure 21 shows the deformed mesh at the end of the static solution (fifth step).

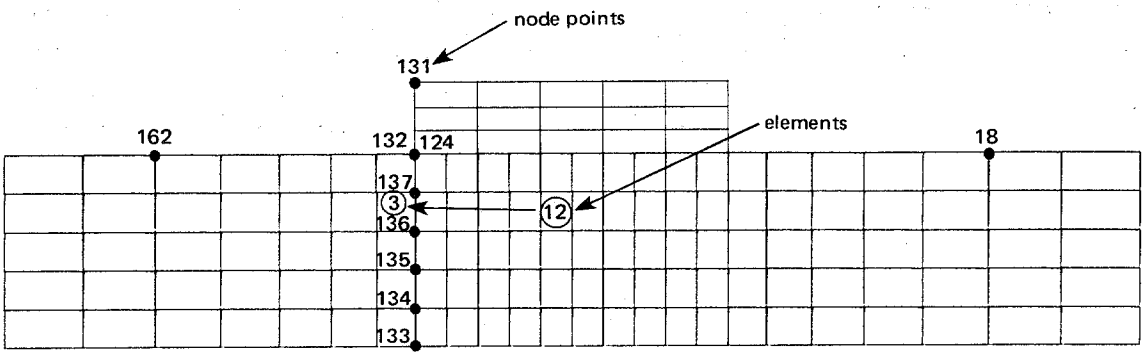

Figure 20. Undeformed mesh.

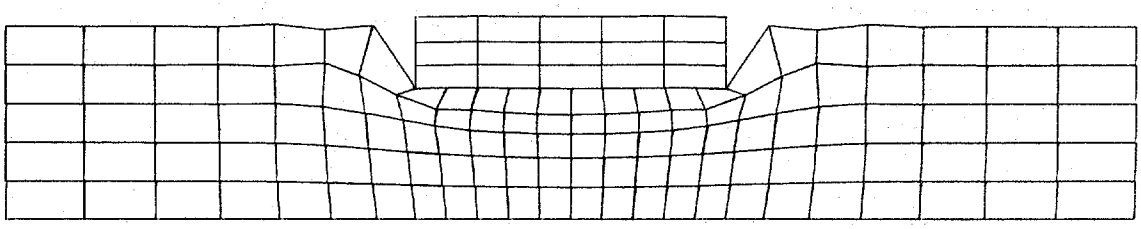

(a) End of static solution, step 5.

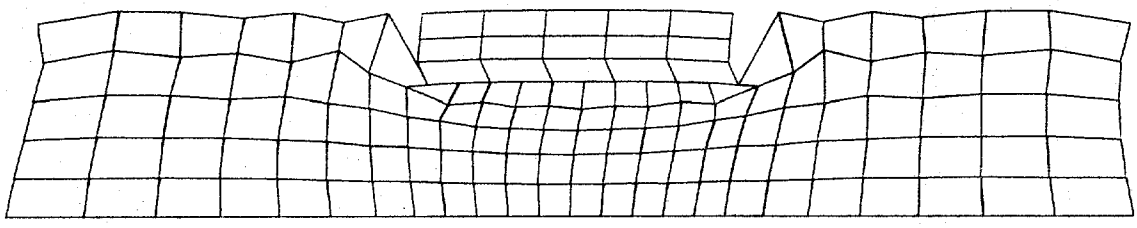

(b) Step 105.

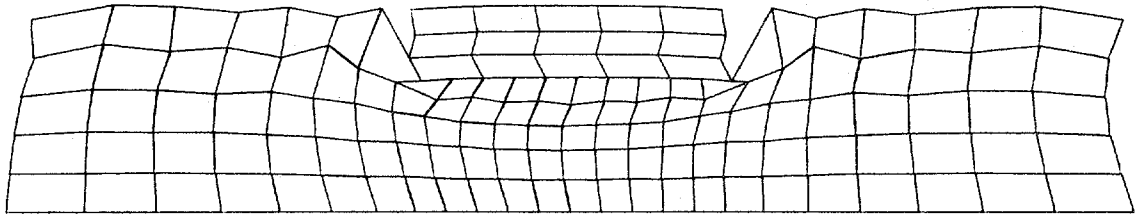

(c) Step 110.

Figure 21. Deformed mesh plots.

At the sixth step, the time increment was changed to a short dynamic increment (0.025 seconds), and the integration parameters α and β were changed to 0.65 and 0.33, respectively, for dynamic damped response. The loading chosen for this case was a sine wave horizontally applied at the base as a displacement function. Since the solution was a continuing solution at the sixth step, initial conditions corresponding to an initial base velocity could not be input during the solution. One approximate technique to eliminate the effect of the initial condition is to merge the desired sinusoidal excitation loading with a cubic function such that derivatives of the function are initially 0.0. To eliminate the fluid pressure buildup at the boundaries, the boundaries were defined to permit flow across them. Fluid forces were computed based on the depth to the center of each element and applied to the nodal points acting on the third degree-of-freedom, as follows:

$$F_w = (\gamma_w \; z \; n) \times \text{element height}$$

where: F_w = total force applied (one-half to each of two boundary nodes' third degree-of-freedom with sign corresponding to direction)

γ_w = unit weight of fluid

z = depth to center of element

n = porosity

The forces active to restrain the vertical boundary from the soil weight were computed and applied to the first degree-of-freedom as follows:

$$F_s = [\gamma_s \; z \; (1 - n)] \times \text{element height}$$

where: F_s = total force applied one-half to each of the two boundary nodes' first degree-of-freedom with sign corresponding to direction

γ_s = unit weight of solids

Figures 21b and 21c presents the deformed mesh, showing the soil field and structure displacement to an exaggerated scale. Figure 22 shows velocity vector plots. Figure 23 shows the out-of-balance forces, which indicate the stability of the solution. The solution reaches a stable level of force imbalance oscillating around 400 kg. Computational stability was not a problem for the time step selected and probably could be continued several fold without increased error. Figures 24 and 25 show acceleration and velocity in the free field, near the structure and at the base (input motion) (Figure 20 shows nodal number locations). The results show minor amplification of motion. Figure 26 shows the mean effective stress after the static solution, step 5. Figure 27 shows the mean effective stress at points in the solution; Figure 28 shows the pore pressure at the same points in time. Figure 29 gives pore pressure and mean stress histories at two locations (see Figure 20).

Results of the analysis show increases in pore pressure around the sides of the structure and beneath the structure with horizontal shaking. The level of increase is consistent with the 0.1g excitation.

The problem was repeated with a base acceleration of 0.25g. In this case, attentuation of ground motion resulted. Pore pressures increased over those of the previous run.

PILE AND PIER FOUNDATIONS

Load Capacity

Piles and piers are used to transmit foundation loads to strata of adequate bearing capacity and to eliminate settlements. Piles also are often used to resist lateral loads or uplift forces. Pile use often determines the type of pile chosen: timber piles are well-suited for use as friction piles in granular materials; steel piles are best for endbearing on rock; concrete cast-in-place piles are economical to use; and concrete-filled steel piles offer high bending resistance. Depending on the type of pile used, piles are either driven or cast-in-place. Deep foundations utilize piers that resemble large cast-in-place piles to transmit the loading.

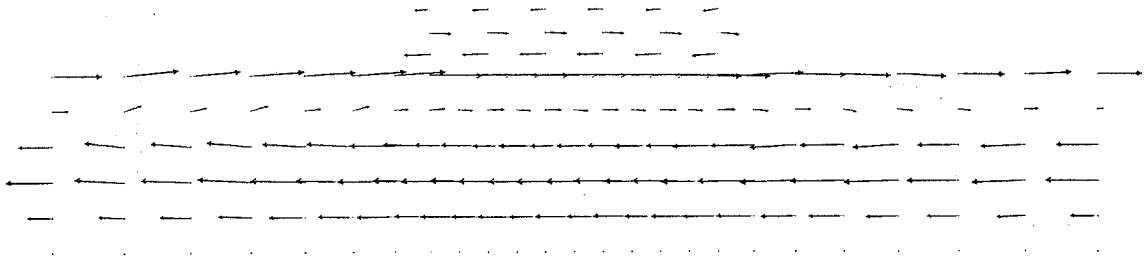

(a) Step 105 (scale factor 18.537).

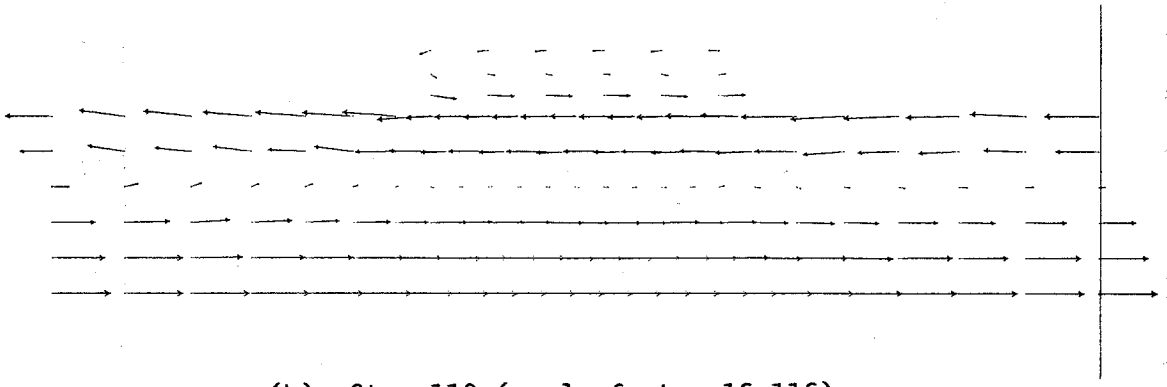

(b) Step 110 (scale factor 16.116).

Figure 22. Velocity vector plots.

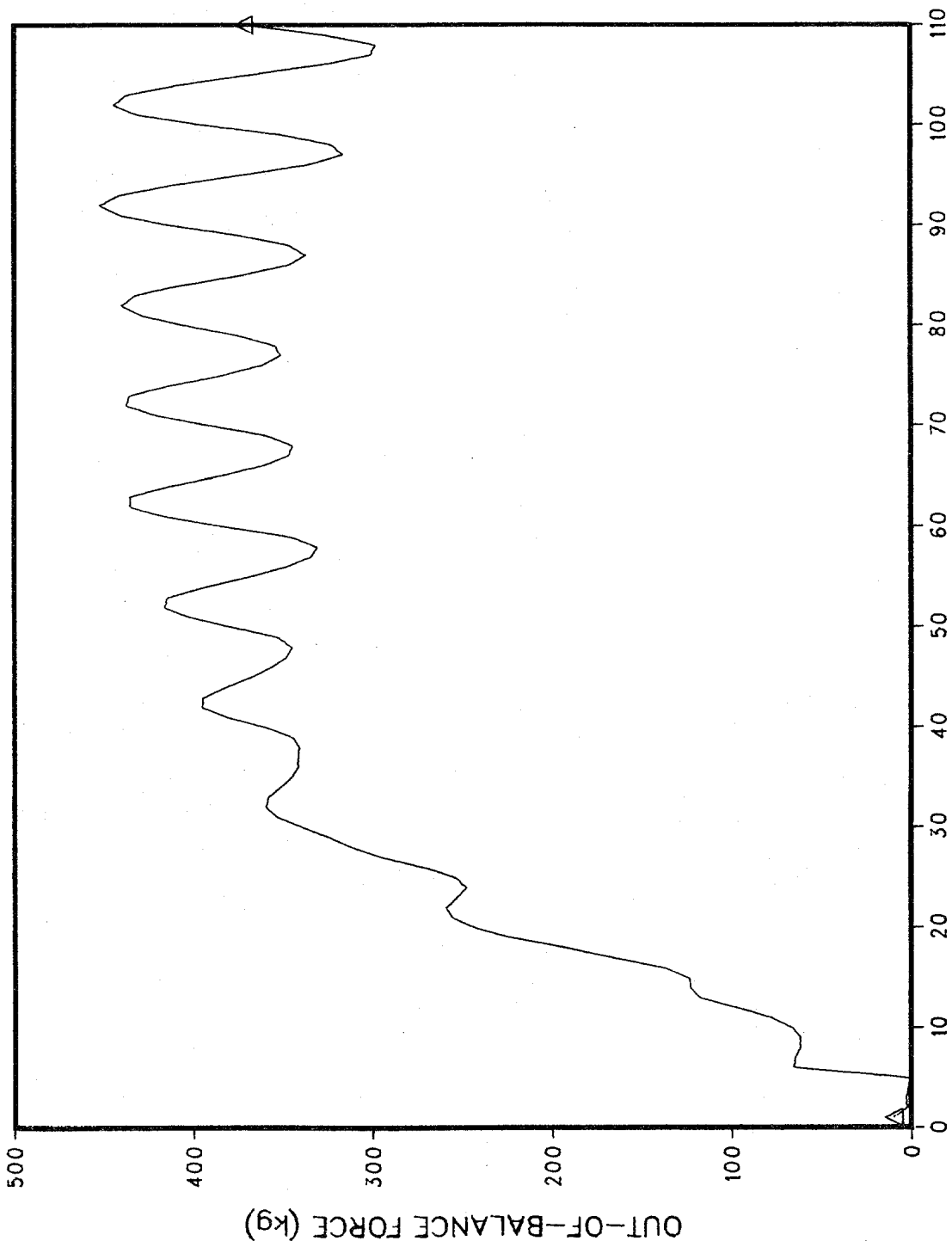

Figure 23. Out-of-balance forces.

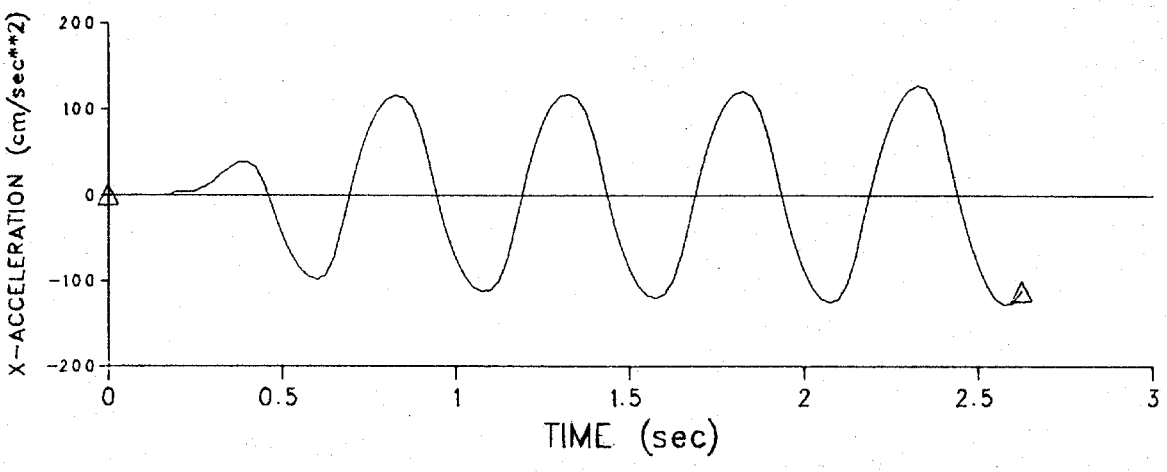

(a) Node 162.

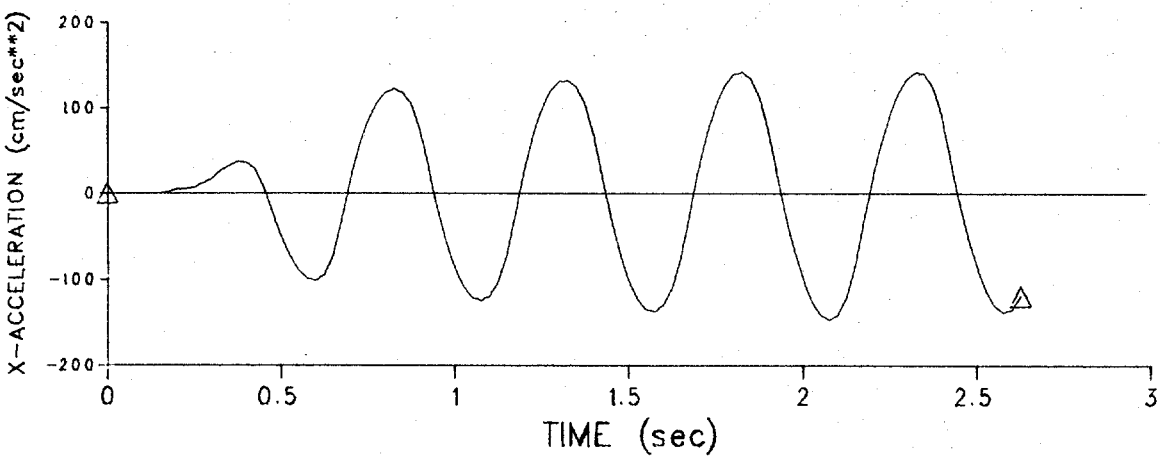

(b) Node 132.

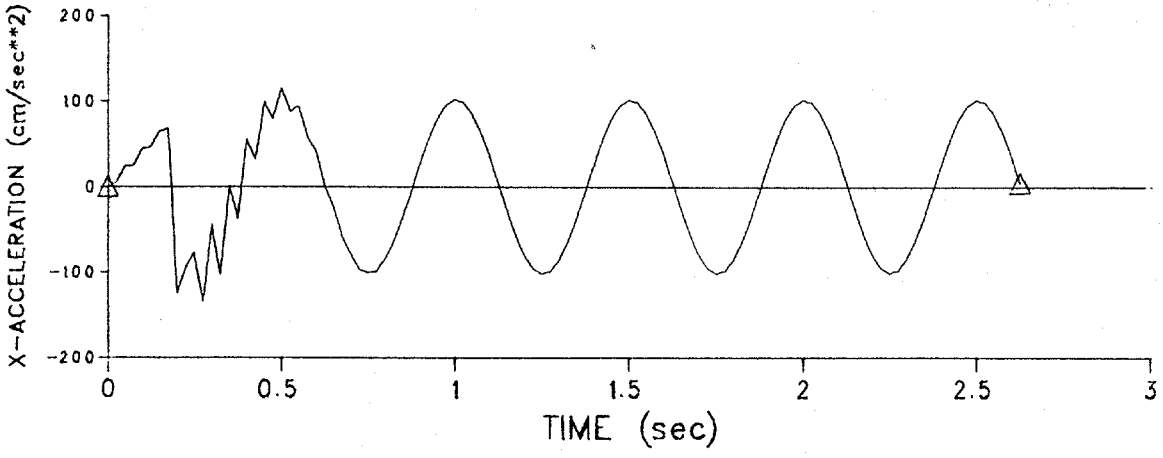

(c) Node 133.

Figure 24. Nodal acceleration.

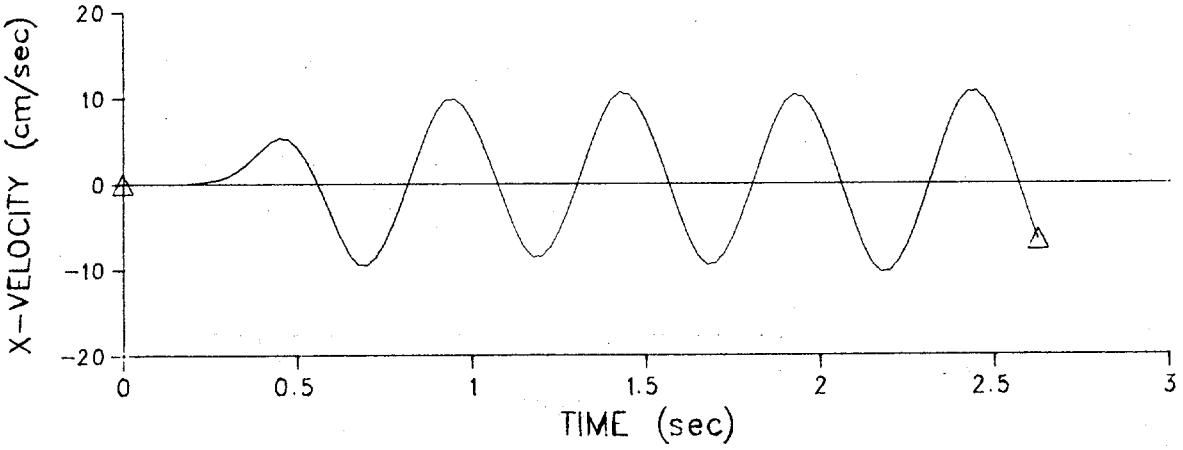

(a) Node 162.

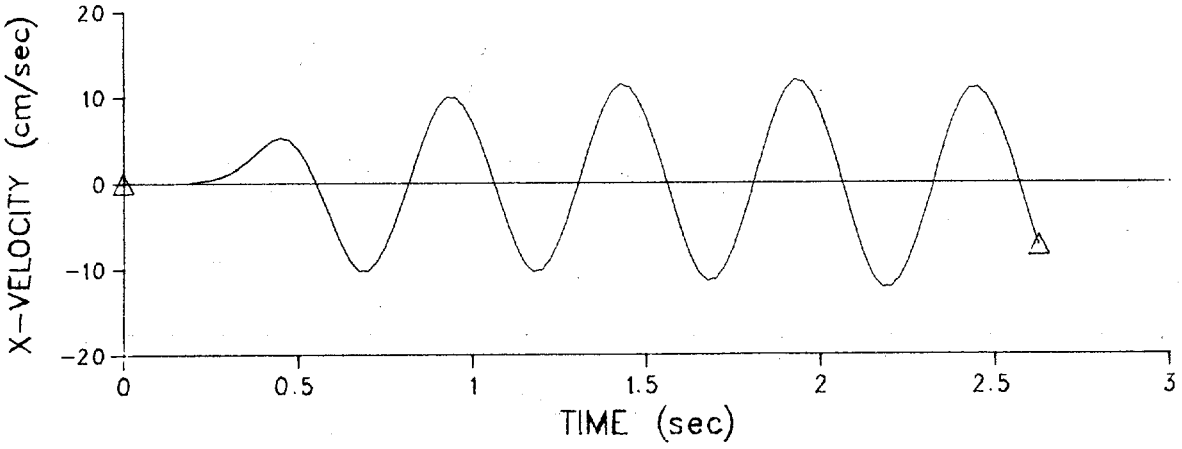

(b) Node 132.

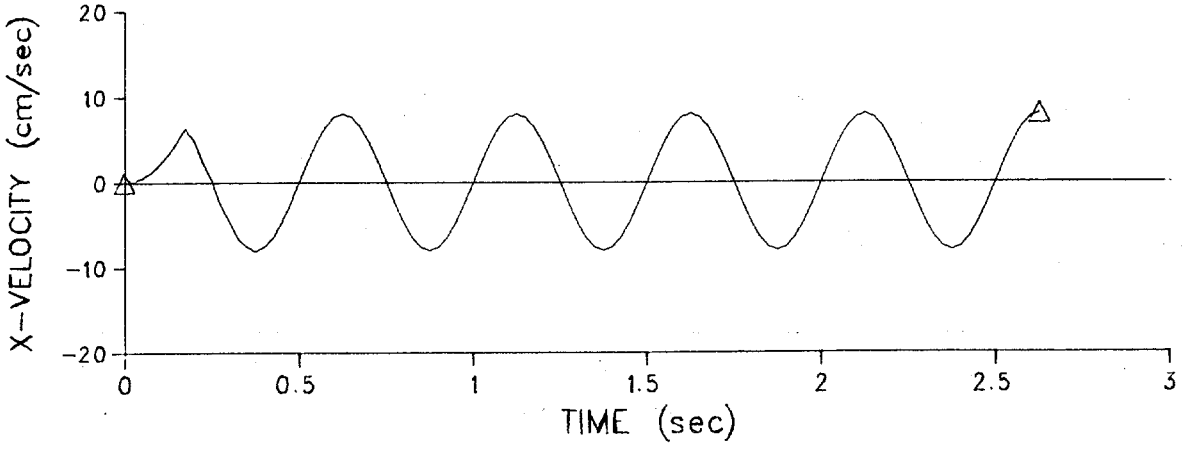

(c) Node 133.

Figure 25. Nodal velocity.

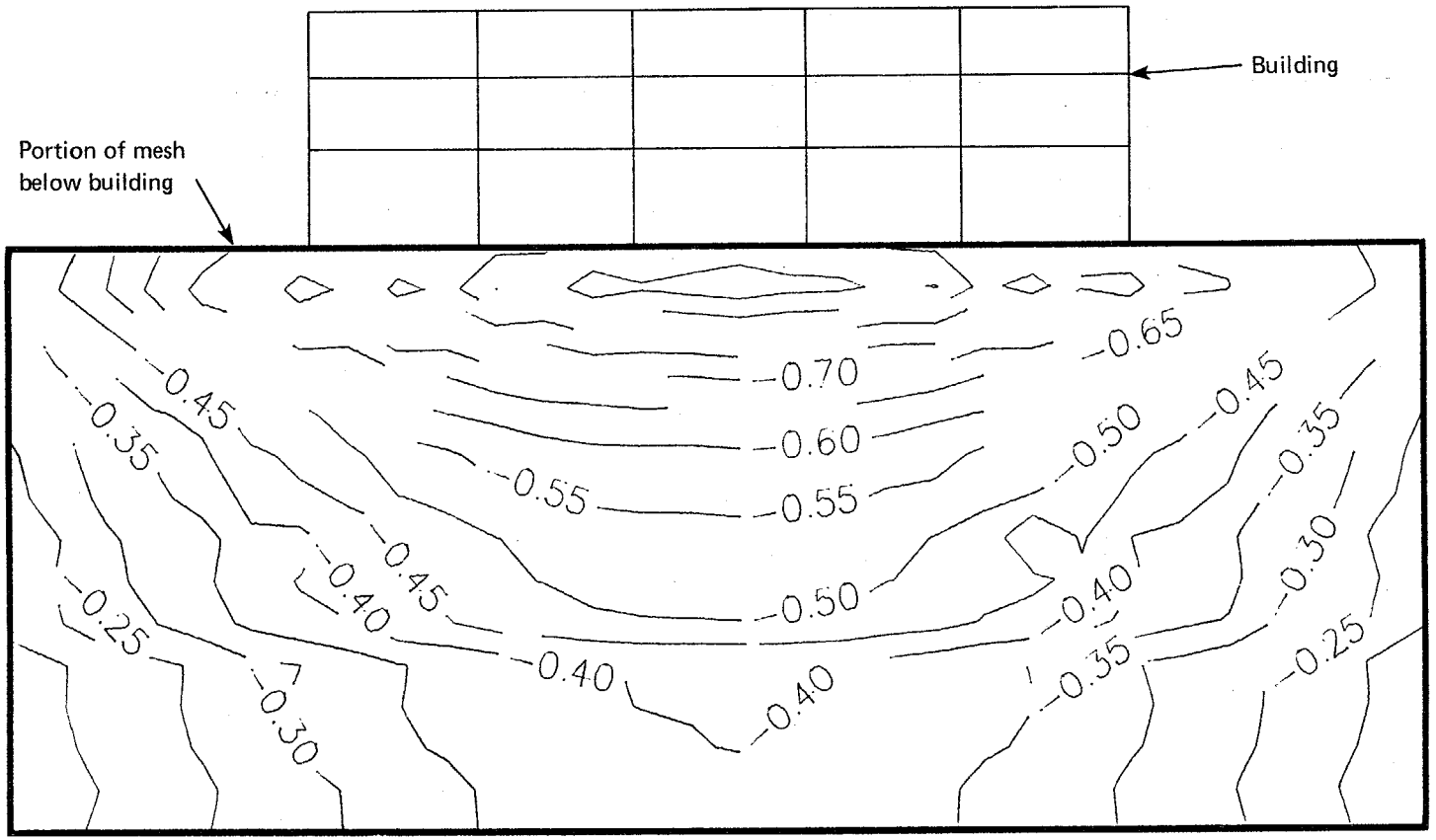

Figure 26. Mean stress (kg/cm^2) after static building load with free field gravity stresses removed.

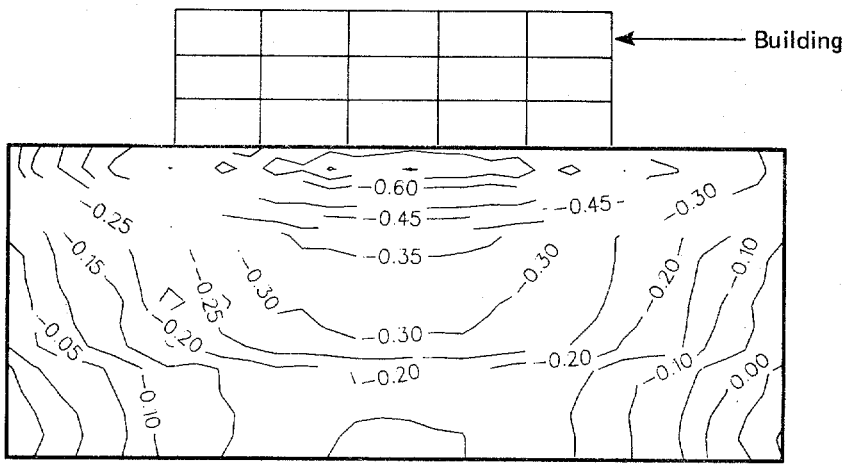

(a) Step 95.

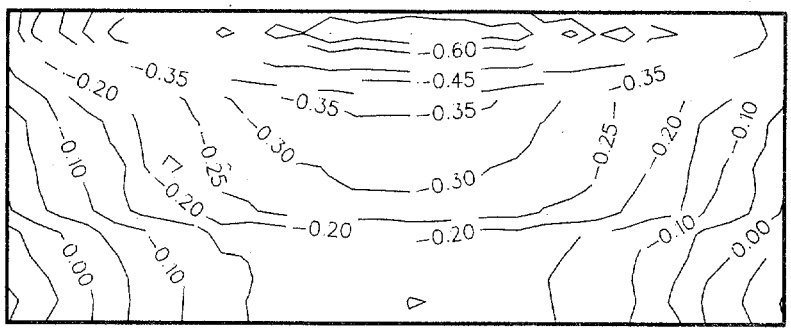

(b) Step 100.

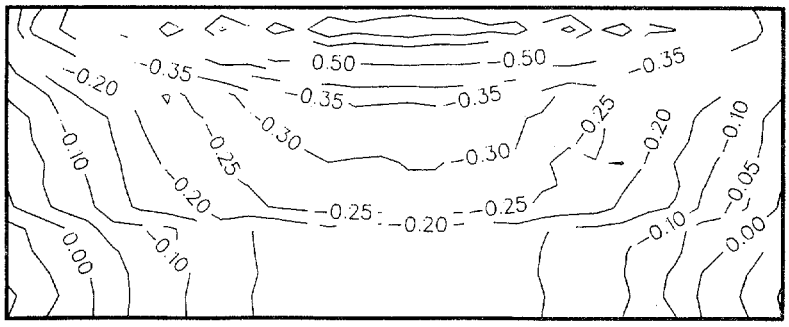

(c) Step 105.

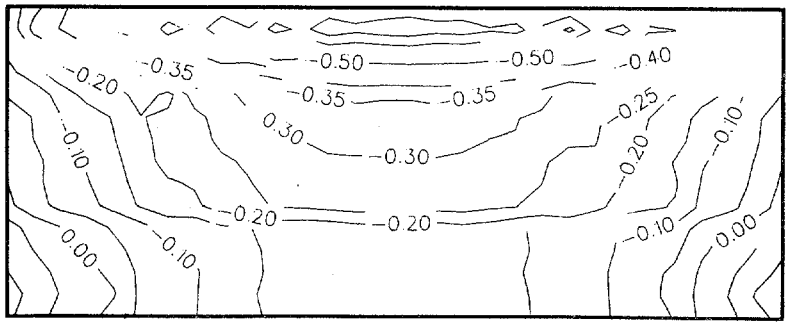

(d) Step 110.

Figure 27. Mean effective stress, kg/cm^2.

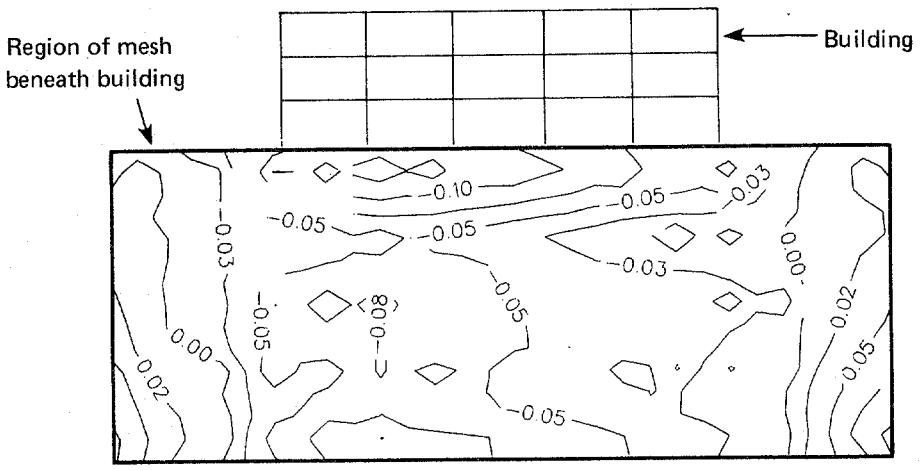

(a) Step 95.

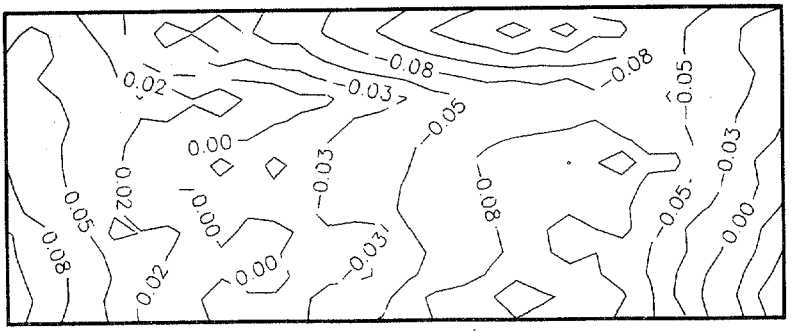

(b) Step 100.

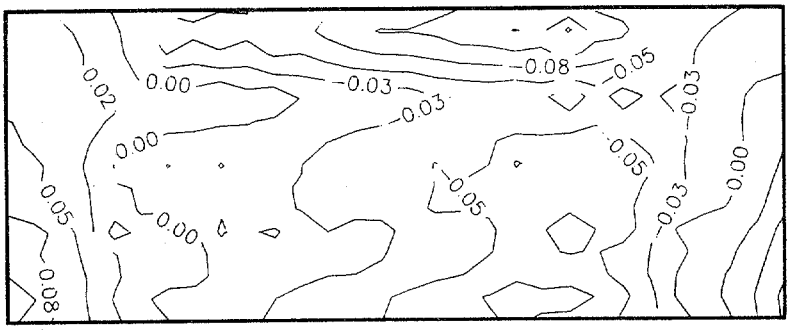

(c) Step 105.

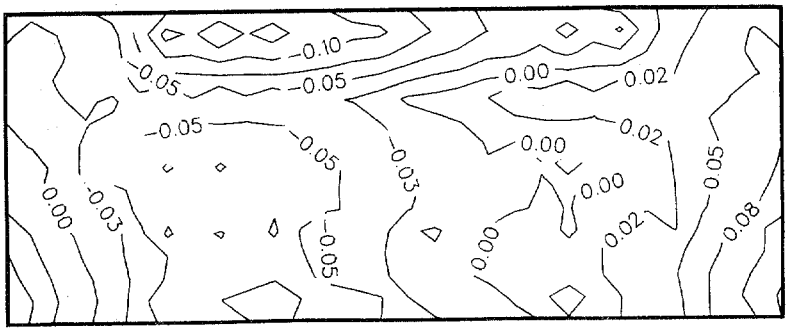

(d) Step 110.

Figure 28. Pore pressure beneath bulding, kg/cm^2.
Note: Gravity effects removed (minus indicates below original condition).

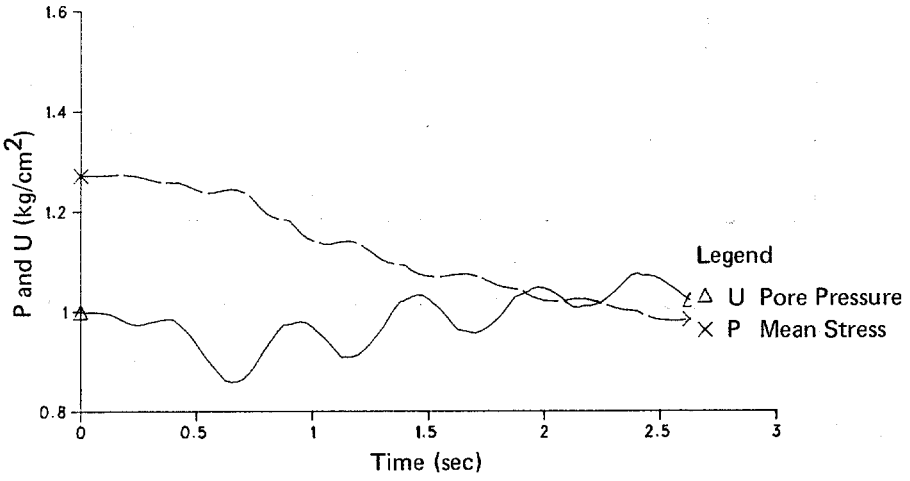

(a) Element 3.

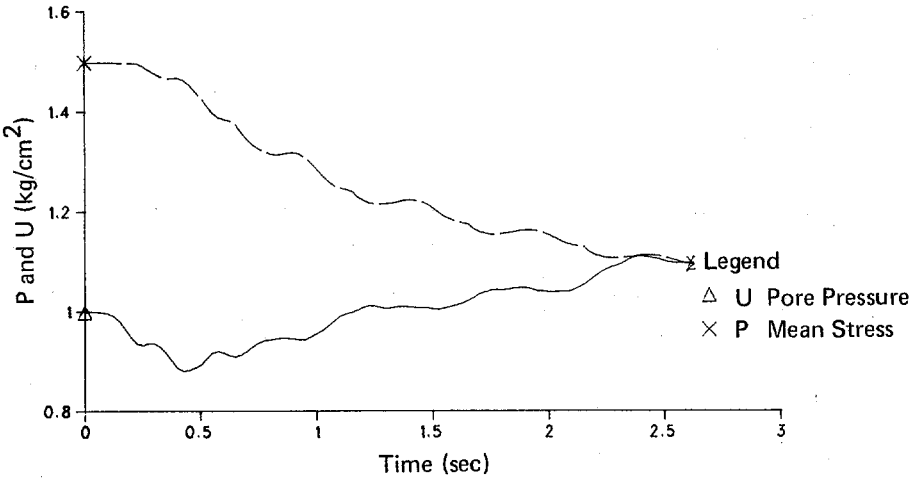

(b) Element 12.

Figure 29. Pore pressure time histories.

This discussion will consider only straight piles driven into homogeneous deposits of cohesionless materials. Experience has shown that when piles are driven into sand, the soil near the pile is compacted to a distance of a few pile diameters. In a homogeneous sand the point resistance and average skin friction increase with depth of penetration up to a critical depth. Beyond the critical depth, the point resistance and skin friction remain almost constant; generally, this is caused by soil compressibility, crushing, and arching. The empirical approach to prediction of pile behavior has proven more satisfactory than an analytical bearing capacity approach.

The load transfer mechanism between the pile and the surrounding soil governs the behavior of the pile. The design of a pile requires determination of the proportion of load transferred to the soil by adhesion and friction between the pile and the soil and that transferred by end bearing. This is influenced by the flexibility of the pile, the stiffness of the soil, and the nature of the transfer mechanisms between pile surface and soil.

Through use of instrumented field and model studies, the design of piles and piers has been better understood. Figure 30 illustrates use of pile-driving resistance formulas to estimate individual allowable pile loads. Figure 31 illustrates the calculation of ultimate load capacity of piles in cohesive soils, and Figures 32 and 33 illustrate the calculation of load capacity of piles for cohesionless soils. However, these conventional ultimate design approaches assume the simultaneous and full mobilization of pile shear resistance and base bearing, which is not well-founded. Studies have shown that movement of a pile must be present to mobilize its load-carrying capacity.

Reese and O'Neill (Ref 11) show the division of load between pier and base for a pier on stiff clay (Figure 34). The first two load increments show that almost all the load is carried by friction; as the load increases, more is carried by end bearing. Above 80 tons, any additional load is taken by end bearing. Note how curve C simply translates to form curve D, indicating additional load is taken by end bearing. With the information in Figure 34, a typical load transfer relationship can be obtained showing side friction (Figure 35). From

the slope in Figure 34, it is evident that frictional effects are greatest in the middle (depth) of the pile; and a reduction in the rate of load transfer occurs in the lower part, particularly just above the base. The distribution of frictional forces depends upon the soil type. Modifications to ultimate strength formulations have been suggested by Reese and O'Neill (Ref 11). Factors include an effective depth concept in lateral earth pressure calculation for granular soils and a friction reduction factor for ultimate resistance in cohesive soils.

A theoretical solution of the load transfer phenomenon can provide considerable insight. For instance, a soil-structure problem would be one in which the nature and mechanism of load transfer is of considerable importance. Solution of this problem must focus on the stress-strain characteristics of the soil and the behavior of the interface between pile and soil. Use of a linear-elastic constitutive model would be a gross simplification of the real material properties. The Prevost soil model offers an opportunity to explore nonlinear relationships.

Several approaches have been used to model the contact problem. Peterson (Ref 13) treats the two contacting surfaces as separate and distinct and joins them mathematically by use of Lagrange multipliers. However, this does not allow pre-slip deformation. Herrmann (Ref 14, 15, and 16) defines three behavior modes: nonslip, slip, and separation. A compatibility model combining compatibility and equilibrium is used. The compatibility model involves linking the two surfaces with fictitious bond springs, and the frictional forces are applied as surface tractions. This allows a pre-slip deformation that would not otherwise be computed.

Another approach simply links two nodes, initially overlapping with nonlinear springs. The procedure has the advantage of simplicity of operation but, unfortunately, may produce undesirable numerical characteristics when distinct rapid changes occur in stiffness.

Prevost has formulated a contact element in the DYNAFLOW code. The contact element may be used to impose inequality constraints between nodes. Either perfect friction (i.e., "stick") or frictionless (i.e., "slip") conditions may be achieved.

Basic pile driving formulas

For drop hammer	For single-acting hammer	For double-acting differential hammer
$Q_{all} = \frac{2WH}{s+1}$	$Q_{all} = \frac{2WH}{s+0.1}$ {Use when driven weights are smaller than striking weights.	$Q_{all} = \frac{2E}{s+0.1}$ {Use when driven weights are smaller than striking weights.
	$Q_{all} = \frac{2WH}{s+0.1\frac{W_D}{W_S}}$ {Use when driven weights are larger than striking weights.	$Q_{all} = \frac{2E}{s+0.1\frac{W_D}{W_S}}$ {Use when driven weights are larger than striking weights.

Q_{all} = allowable pile load in pounds.
W = weight of striking parts of hammer in pounds.
H = the effective height of fall in feet.
E = the actual energy delivered by hammer per blow in foot-pounds.
s = average net penetration in inches per blow for the last 6 in. of driving.
W_D = driven weights
W_S = weights of striking parts
} Note: Ratio of driven weights to striking weights should not exceed 3.

Modifications of basic pile driving formulas

A. For piles driven to and seated in rock as high capacity end-bearing piles:

Drive to refusal (approximately 4 to 5 blows for the last quarter inch of driving). Redrive open end pipe piles repeatedly until resistance for refusal is reached within 1 in. of additional penetration.

B. Piles driven through stiff compressible materials unsuitable for pile bearing to an underlying bearing stratum:

Add blows attained before reaching bearing stratum to required blows attained in bearing stratum (see example).

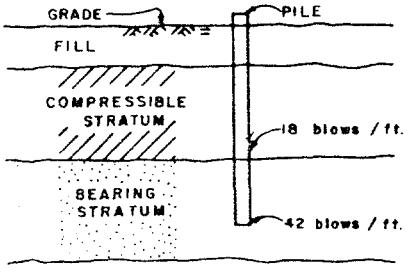

Example: required load capacity of pile Q_{all} = 25 tons
hammer energy E = 15,000 ft-lb

$$\frac{W_D}{W_S} < 1$$

Penetration(s) as per basic formula = $\frac{1}{2}$" or 2 blows per inch (24 blows/ft).

Required blows for pile 24 + 18 = 42 blows/ft.

C. Piles driven into limited thin bearing stratum, drive to predetermined tip elevation. Determine allowable load by load test.

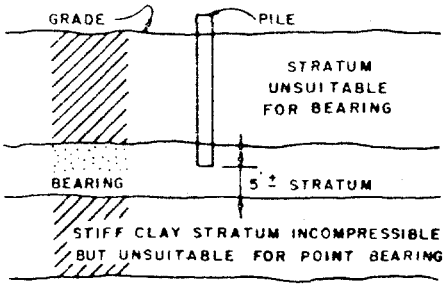

Figure 30. Application of pile-driving resistance formulas (Ref 11).

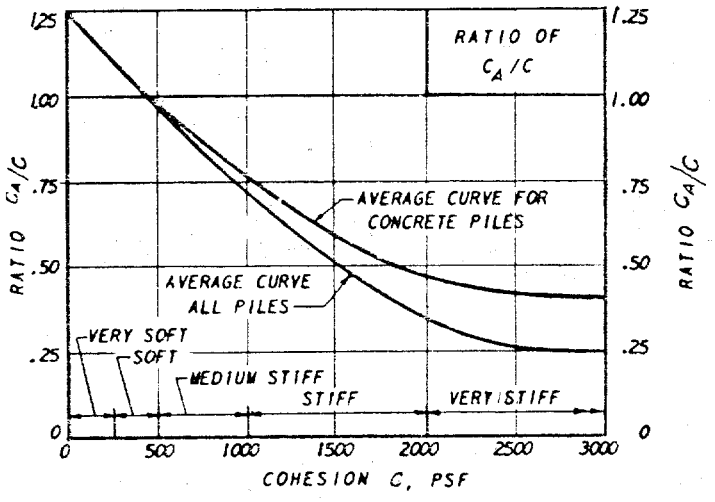

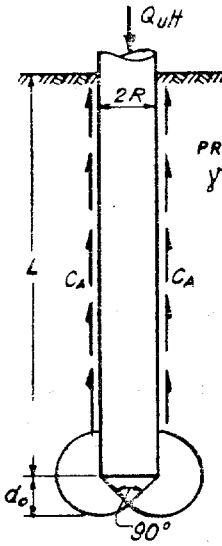

SOIL PROPERTIES $\gamma_T, C, \phi = 0$

POSITION OF GROUND WATER HAS NO EFFECT ON ULTIMATE LOAD CAPACITY UNLESS COHESION IS CHANGED.

Q_{ult} IS APPLIED LOAD ONLY. PILE WEIGHT IS BALANCED BY WEIGHT OF OVERBURDEN AND IS NOT CONSIDERED.

RECOMMENDED VALUES OF ADHESION

PILE TYPE	CONSISTENCY OF SOIL	COHESION, C PSF	ADHESION, C_A PSF
TIMBER AND CONCRETE	VERY SOFT	0 - 250	0 - 250
	SOFT	250 - 500	250 - 480
	MED. STIFF	500 - 1000	480 - 750
	STIFF	1000 - 2000	750 - 950
	VERY STIFF	2000 - 4000	950 - 1300
STEEL	VERY SOFT	0 - 250	0 - 250
	SOFT	250 - 500	250 - 460
	MED. STIFF	500 - 1000	460 - 700
	STIFF	1000 - 2000	700 - 720
	VERY STIFF	2000 - 4000	720 - 750

ULTIMATE LOAD CAPACITY

$$Q_{ult} = cN_{cs}\pi R^2 + C_A 2\pi RL$$

PULLOUT CAPACITY

$$T_{ult} = C_A 2\pi RL$$

T_{ult} UNDER SUSTAINED LOAD MAY BE LIMITED BY OTHER FACTORS.

ULTIMATE LOAD FOR BUCKLING OF STEEL PILES IN SOFT CLAY.

$$Q_{ult} = \lambda (C E I)^{1/2}$$

λ = 8 FOR VERY SOFT CLAY, 10 FOR SOFT CLAY (DIMENSIONLESS)

C = SOIL SHEAR STRENGTH

I = MOMENT OF ENERTIA OF CROSS SECTION

E = MODULUS OF ELASTICITY OF STEEL.

} POUND AND INCH UNITS

FORMULA APPLIES TO SLENDER STEEL PILES. GENERALLY HEAVY STEEL PILES OR TIMBER OR CONCRETE PILES ARE NOT SUBJECT TO BUCKLING IF EMBEDDED IN SOIL FOR THEIR ENTIRE LENGTH.

Figure 31. Ultimate load capacity of piles in cohesive soils (Ref 11).

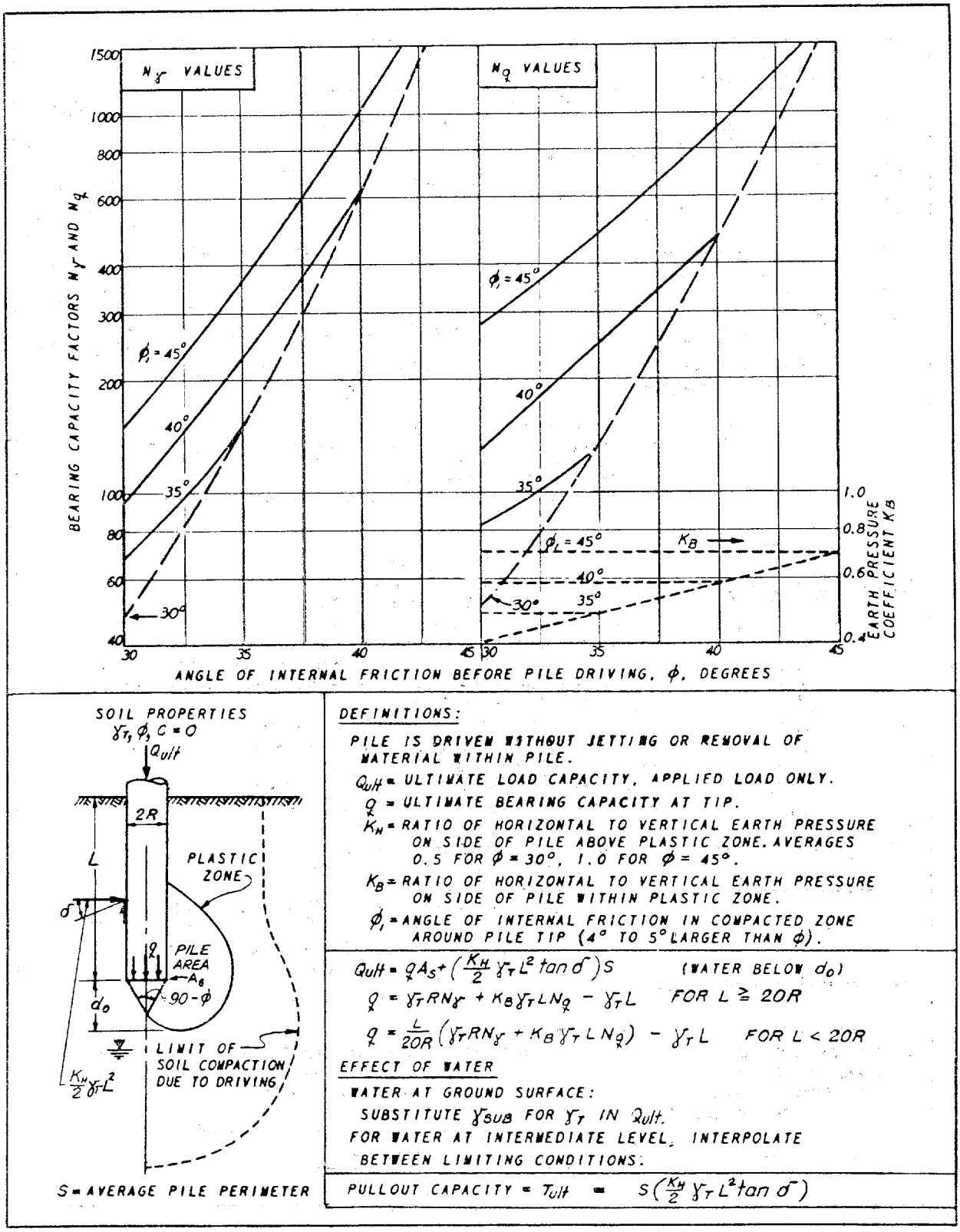

Figure 32. Ultimate load capacity of piles in cohesionless soil (for alternative method, see Figure 33) (Ref 11).

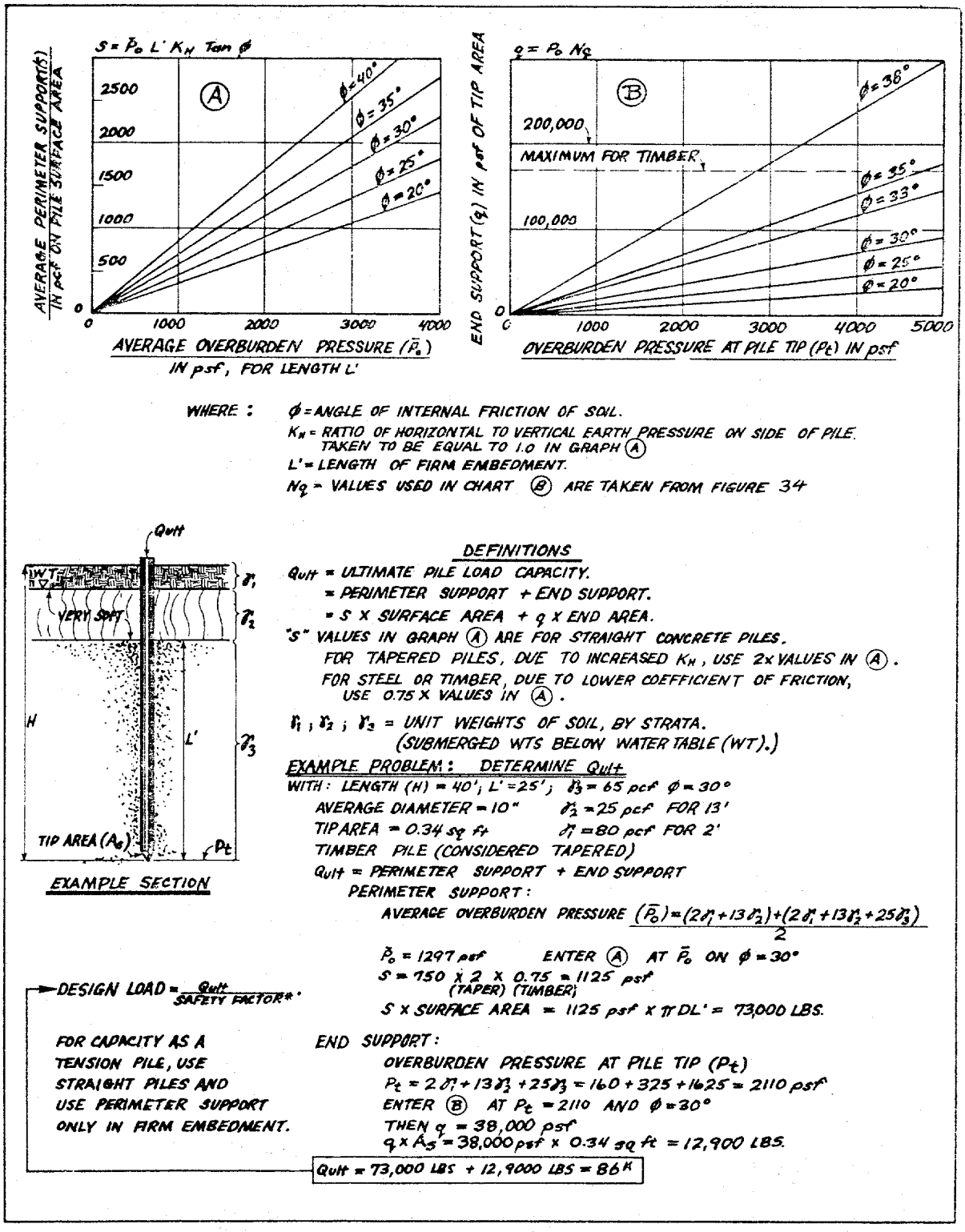

Figure 33. Ultimate load capacity of driven piles in cohesionless soils (alternative method to Figure 32) (Ref 11).

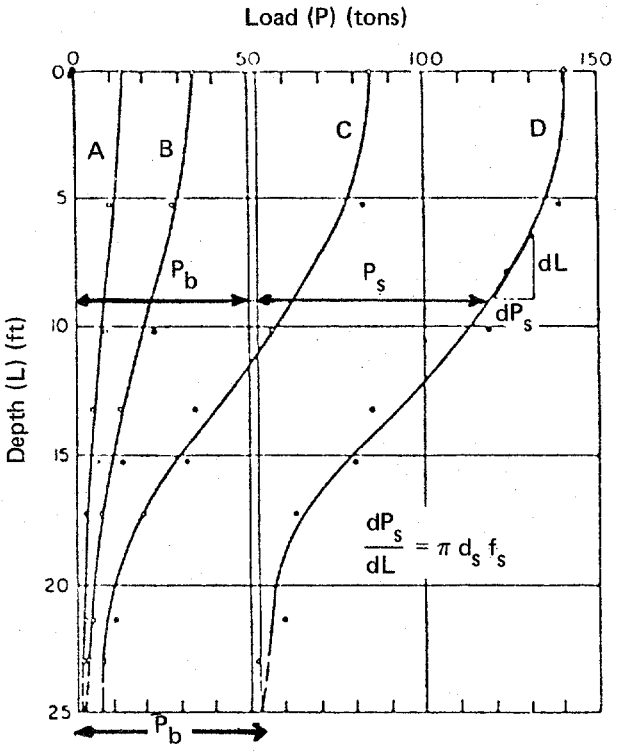

Figure 34. Load distribution in a 25-foot-long straight-shaft pier drilled into stiff clay.

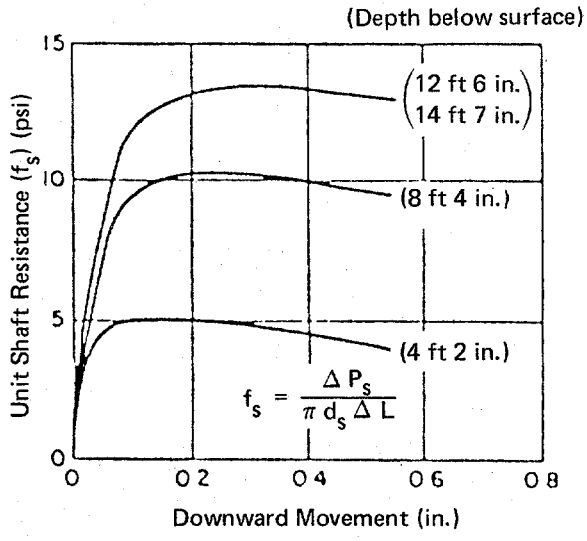

Figure 35. Load transfer to shaft segment (ΔL) versus downward movement of segment.

A contact element is defined by two nodes: a spring constant or "penalty parameter," k, and a fixed direction vector, $\underset{\sim}{n}$. The present location of node A ($\alpha = 1, 2$) is given by $\underset{\sim}{x}_A + \underset{\sim}{d}_A$, where $\underset{\sim}{x}_A$ is the initial position vector and $\underset{\sim}{d}_A$ is the displacement vector. The contact plane passes through the point $\underset{\sim}{x}_A + \underset{\sim}{d}_A$ and is perpendicular to $\underset{\sim}{n}$ (Figure 36a). The contact/release condition is defined as follows:

$\sigma > 0$ release

$\sigma \leqq 0$ contact

where: $\sigma = \underset{\sim}{\ell} \cdot \underset{\sim}{n}$

$\underset{\sim}{\ell} = \underset{\sim}{x}_B + \underset{\sim}{d}_B - \underset{\sim}{x}_A - \underset{\sim}{d}_A$

The quantity σ is a measure of the distance between $x_B + d_B$ and the contact plane. When contact is noted, a contact element stiffness and out-of-balance force are added to the global equations.

If $k > 0$ is sufficiently large, the point $\underset{\sim}{x}_B + \underset{\sim}{d}_B$ will be forced to lie (approximately) on the contact plane. In subsequent steps, only the stiffness is assembled, and the decision to remain in contact or to release is made on the basis of the sign of σ, as above.

For interpreting output, the contact element "displacement" is defined as σ, and the "force" is given by:

$k\sigma$ if $\sigma < 0$

0 if $\sigma \geqq 0$

In addition to the contact element, Prevost has defined a slide element. The slide-line element may be used to impose inequality constraints between nodes. Either perfect friction (i.e., stick) or frictionless (i.e., slip) conditions may be achieved.

A slide-line element is defined by three nodes and a spring constant or penalty parameter, k. The connection from node A to node B defines the slide-line direction, and node C is the contact node (Figure 36b).

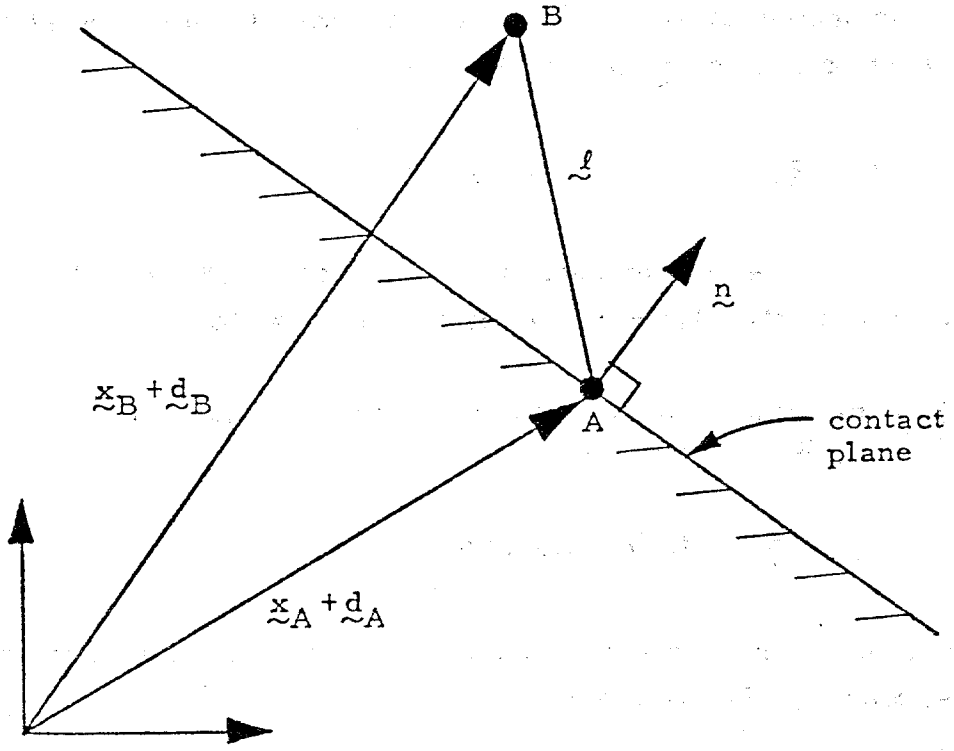

(a) Contact element.

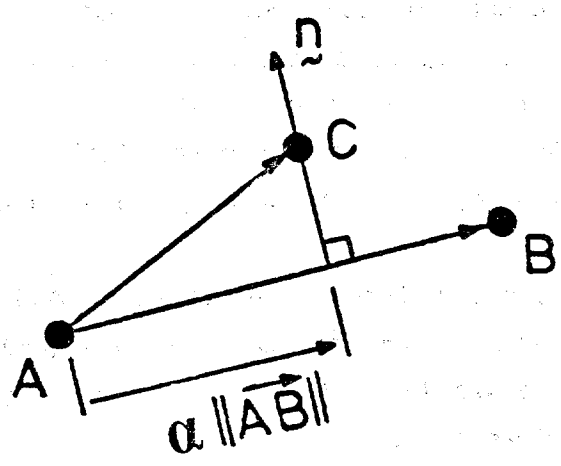

(b) Slide element.

Figure 36. Program DYNAFLOW.

The projected distance of node C to node A onto the slide-line direction is denoted by α and is given by:

$$\alpha = \vec{AB} \cdot \vec{AC} / AB^2 \qquad 0 \leqq \alpha \leqq 1$$

where $\cdot$ is the the dot product of two vectors. The direction of the unit vector $\vec{n}$ to the slide-line direction is given by:

(1) in two dimensions by rotating $\vec{AB}$ as an angle + $\pi/2$
(2) in three-dimensions by

$$\vec{n} = (\vec{AB} \times \vec{AC}) \times \vec{AB} / \left|(\vec{AB} \times \vec{AC}) \times \vec{AB}\right|$$

where x denotes the cross product of two vectors. The local contact stiffness matrix $\underset{\sim}{k}$ is given by:

$$\underset{\sim}{k} = k \begin{bmatrix} (1-\alpha)^2 & \alpha(1-\alpha) & -(1-\alpha) \\ \alpha(1-\alpha) & \alpha^2 & -\alpha \\ -(1-\alpha) & -\alpha & 1 \end{bmatrix}$$

where the rows and columns are arranged such that the first, second, and third rows (columns) correspond to nodes A, B, and C, respectively. The contact/release condition is defined as follows: (1) in two-dimensions, if $0 \leqq \alpha \leqq 1$ and $\vec{AB} \cdot \vec{n} \leqq 0$, then contact (otherwise, release); and (2) in three-dimensions, if $0 \leqq \alpha \leqq 1$, then contact (otherwise, release).

If k is sufficiently large, the point C will be forced to lie (approximately) on the slide-line AB. In subsequent steps, only the contact stiffness is assembled, and the decision to remain in contact or not is made as described above.

Cyclic Behavior of Piles

Poulos (Ref 17) concludes that ultimate load capacity and cyclic stiffness decrease with increasing numbers of cycles and increasing cycle load level. This becomes more significant when the cyclic load approaches one-half the static ultimate load. The cyclic degradation appears to begin at the top of the pile and progresses downward, resulting in a gradual transfer of load to the lower position of the pile. The crucial factor in determining the amount of cyclic degradation is the shear strain for skin friction.

Poulos (Ref 18) conducted a limited investigation of an effective stress approach to determine pore pressure increases with cyclic loading and the resulting modulus degradation factors. Possibly, a lack of data prevented further development. Figure 37 shows a compilation of observations (Ref 17) showing degradation as a function of strain ratio, where:

$$\gamma_{ss} = (0.10 \text{ to } 0.25)\ \gamma_s$$

and

γ_s = static shear strain to failure

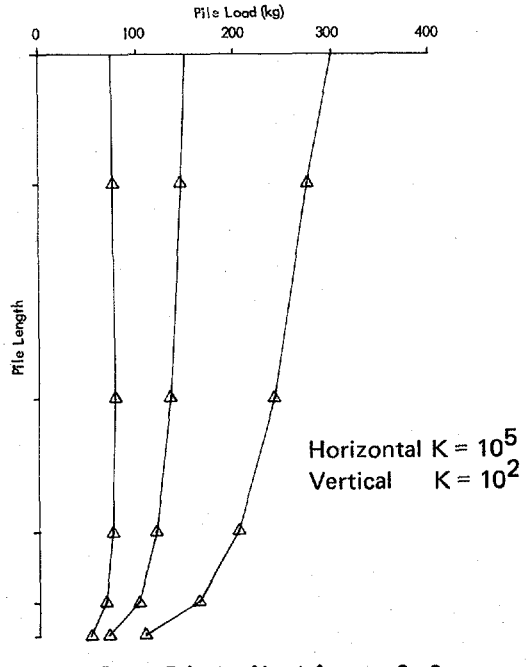

Figure 37. Distribution of force within pile, 75, 150 and 300 kg loads.

Poulos (Ref 16) reports that "one-way" cyclic loading (i.e., cyclic loading between zero minimum load and a specified maximum) produces significantly less degradation of pile capacity than would occur with "two-way" loading (i.e., loading alternating between tension and compression with zero as a mean value). He points out that degradation will occur at different rates along the pile, depending on local stress level. Even in initially homogeneous soil, a nonuniform distribution of soil modulus and skin friction will result from cyclic loading because nonuniformity of stress distribution occurs along the pile. Degradation occurs in the ultimate skin friction along the length of the pile and also in the ultimate base resistance. The major problem in a cyclic response is determining how the degradation factors vary with strain and number of cycles.

The cyclic shear strain in the soil adjacent to the pile, γ_c, can be estimated as:

$$\gamma_c = \frac{2 P_c}{\xi d}$$

where: P_c = cyclic displacement of pile at a point on the pile shaft

d = pile diameter

$\xi = \ell n [5\Psi (1 - \mu_s) L/d]$

Ψ = 1.0 homogeneous infinitely deep soil and
0.5 modulus increases with depth

μ_s = Poisson's ratio

L = embedded pile length

The cyclic base strain can be estimated from the above assuming $\mu_s = 0.5$, $L/d = 100$.

$$\gamma_c = \frac{0 \cdot 4 P_{bc}}{d_b}$$

where P_{bc} is the cyclic displacement of pile base and d_b is the diameter of pile base.

It is important to note that the above is based on the assumptions of elastic behavior. Typical predictions for pile settlement take the form of Figure 38. Also shown in Figure 38 is the ultimate cyclic load as a function of number of cycles. The settlement problem is the major concern for piles in cohesionless materials.

Friction Between Calcareous Sand and Building Materials

Calcareous sediments have proven troublesome to offshore facilities. Piles driven into calcareous sands have been noted to penetrate and to be extracted with much less effort than predicted by conventional techniques. A research program was previously conducted at NCEL (Ref 19) in which calcareous sediments were collected from three environments: a deep-ocean site, a shallow-ocean site, and coralline sand from an atoll beach. The coefficients of friction of these sands and of a quartz sand used as a standard were measured against surfaces of rough and smooth steel and mortar. Volume changes were measured as a function of sliding displacement.

Experience has caused engineers to reduce pile capacities in calcareous materials. This usually results in load capacity reductions to one-fourth that of piles in normal materials. In the past, it was not clearly understood why calcareous materials exhibit inferior pile support. Measured angles of internal friction -- a measure of strength -- are high: 34 degrees or greater. Part of the problem was identified as the low increase in soil effective stress during pile driving, which is thought to result from a crushing or collapse of a cemented soil structure or from the breakup of individual carbonate grains. This lack of increase in effective stress results in a relatively lower shear strength in the soil mass surrounding the pile. Further, it was thought that the coefficients of friction might be substantially less between calcareous materials and piles. Valent (Ref 18) conducted a test program using a modified direct shear test machine in which the lower half of the apparatus contained the building material and the upper half the soil sample. Table 2 summarizes his results.

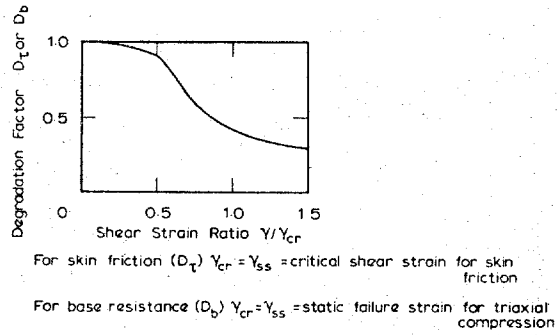

(a) Degradation.

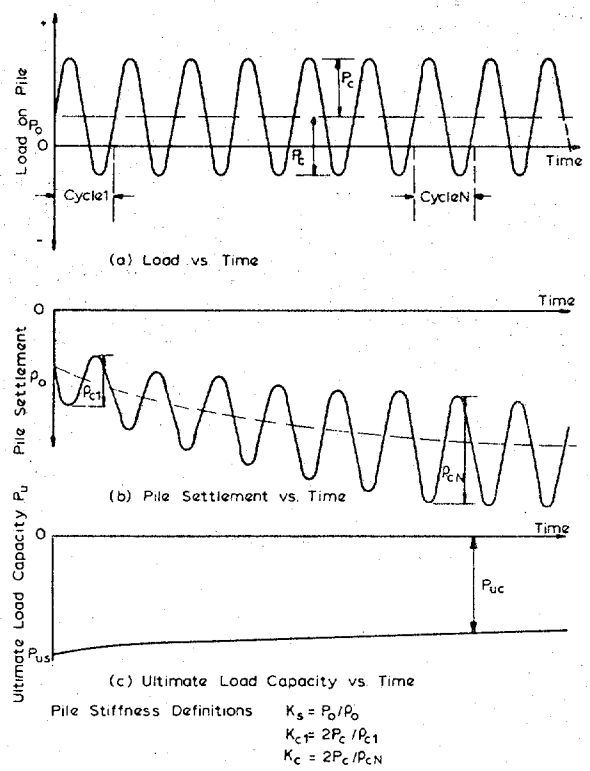

(b) Cyclic loading.

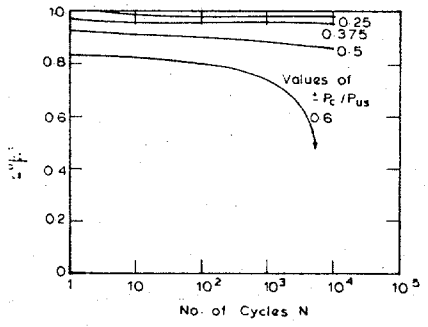

(c) Number of cycles.

Figure 38. Pile degradation with cyclic loading (Ref 18).

Table 2. Summary of Friction Test Results (Ref 18)

Test No.	Soil Material	μ_{peak} [a]	$\mu_{residual}$ [a]
Base Material[b]: Sand[c]			
1	Quartz sand	0.67[d]	0.54
2	Coralline sand	0.66	0.56
3	Coralline sand	0.68[d]	0.57
4	Oolitic sand	0.77	0.61
5	Oolitic sand	0.81[d]	0.62
6	Foram sand-silt	0.64	0.58
Base Material[b]: Smooth Steel			
7	Quartz sand	0.27[d]	0.19
8	Coralline sand	0.20	0.17[e]
9	Coralline sand	0.20	0.18
10	Coralline sand	0.21[d]	0.17
11	Oolitic sand	0.15	0.13
12	Oolitic sand	0.32	0.31
13	Foram sand-silt	0.40	0.37
Base Material[b]: Rough Steel			
14	Quartz sand	0.60	0.54
15	Coralline sand	0.63	0.55
16	Oolitic sand	0.54	0.51
17	Oolitic sand	0.58[f]	0.50
18	Foram sand-silt	----[f]	0.66
Base Material[b]: Smooth Concrete			
19	Quartz sand	0.60	0.54
20	Coralline sand	0.63	0.56
21	Oolitic sand	0.59	0.52
22	Oolitic sand	0.58[f]	0.54
23	Foram sand-silt	----[f]	0.67
Base Material[b]: Rough Concrete			
24	Quartz sand	0.69	0.57
25	Coralline sand	0.66	0.59
26	Oolitic sand	0.74	0.57

[a] For direct shear tests, $\mu = \tan \phi$ where ϕ = angle of internal friction; for friction tests, $\mu = \tan \delta$ where δ = angle of sliding friction.

[b] Soil in bottom shear ring for direct shear tests, or building material in friction tests.

[c] Base material same as soil material for direct shear tests.

[d] These tests run with mechanical measurement system; i.e., proving ring and manual recording of data.

[e] Low value for μ reached shortly after μ_{peak}, thereafter μ increased with displacement to end of test.

[f] No peak μ reached, μ increasing through end of test.

In general, the results show that the low friction forces in calcareous sediments are not the result of low achievable coefficients of friction between calcareous sediments. Since the coefficients of friction of calcareous sands are comparable to other sands, low friction, then, must be attributable to low normal force. Deep-ocean sand (foraminiferal sand-silt) exhibits one possible cause for low developed normal force. The volume change during testing indicated a considerable volume decrease during development of resisting friction force, probably due to crushing of the skeletal structures and shell fragments. Penetration of a pile in such a material would crush the hollow shell material with only a minimal increase in effective stress of the surrounding material.

Quoting from Valent (Ref 19):

> 1. The calcareous sediments tested, and presumably calcareous sediments in general, develop coefficients of friction against steel and concrete building materials that are comparable to those developed by quartz-type sands. Thus, the possibility of low coefficients of friction being responsible for the observed low friction forces on driven piling and other penetrators in calcareous materials is ruled out.
>
> 2. The observed large volume decreases during shear of the foraminiferal sand-silt are probably responsible for the low developed friction forces in these hollow-shelled materials. Such large volume decreases at nonincreasing normal load imply densification in the field without accompanying increases in normal stress on the penetrator surface.
>
> 3. Low developed friction forces in other calcareous materials may arise from a similar mechanism involving a hypothesized loose, but cemented, structure for the soil material. The application of shear stresses during penetration would cause collapse of this structure to a denser, but still loose, arrangement.

Piles in Calcareous Sands

Calcareous sands, as discussed, are noted for loose arrangement of particles lightly cemented to form a structure to support other layers without compacting. However, upon shearing, the structure is destroyed,

breaking the cement bonds; the loose-grained structure then compacts and densifies. The sand (Lade sand) is a very loose sand (30% relative density) and, as such, is a "manufactured" sand that would not occur in nature. The properties of this material might qualitatively be expected to represent the constitutive behavior of a calcareous sand.

To analyze a pile's load capacity using the effective stress soil model, the mesh in Figure 39 was used. This mesh simulates a pile already in place (i.e., not the driving of the pile). Horizontal and vertical springs were used to join the pile to the soil field to simulate the interface and allow for pile movement. Unfortunately, DYNAFLOW permits only elastic springs at this time.

The soil properties used were those of Lade sand. The material properties simulate the condition of the soil after placement of the pile. No densification occurs, since the pile is in place at the start of the analysis. A prediction of pile capacity was made by using conventional techniques found in Figures 32 and 33 adjusted to the problem conditions but without densification. Results indicated a pile resistance in normal average cohesionless sand of at least 1,500 kg with about 150 kg of that in side friction and the remainder in end bearing.

Load Settlement of the Pile. Figure 40 shows the load settlement of the pile. Several values were tried for the spring constants. Results show the pile experiences large settlements between 300 and 400 kg. Figure 37 shows the distribution of force within the pile for three load levels. Note that most of the increase in load is due to skin friction. Figure 41 shows the distribution of force along the pile at a point in the loading having a force of 300 kg applied at the top of the pile. The results in Figure 41 show about one-half to two-thirds of the load is taken in skin friction. The skin friction portion of the load agrees with the predicted values; however, the end bearing is substantially less. It is important to note that the sand used (Lade sand) had a relative density of only 30% which is so loose it does not occur in nature but is "manufactured" in the laboratory. The level of loading is about one-fourth that of a pile in normal sand, which is the

level expected from experience in calcareous sands. Figure 42 shows contours of principal stress around the pile at a typical load step. These show typical patterns, as expected; the level of stress below the pile tip would be on the last surface at yield.

Results show that the order of magnitude of the pile capacity in calcareous materials is predicted correctly. Further, the friction developed on the sides of the pile is at the expected level, not substantially reduced from normal sands. The amount of end bearing is slightly dependent on the vertical spring constant. Use of nonlinear springs would have allowed slip to occur, transferring more load into end bearing when exceeding some local slip level.

Pile Behavior Under Cyclic Loading. Next, pile behavior under cyclic loading was examined. The applied loading consisted of cyclic variation of the vertical load on the pile. In one case, the loading was cycled in "one-way" loading (zero minimum and specified maximum) and in "two-way" loading (alternating compression and tension). The first example was at a relatively low level of loading for the model pile (about one-seventh of yield). Figure 43 shows the stress beneath the pile tip for one-way loading (0 to 50 kg); Figure 44 shows the shear stress contours around the pile. Figure 45 shows the stress beneath the pile tip for two-way loading (-50 to 50 kg); the shear stress plot is similar to that of Figure 46. Note that the tip forces reduce with loading, transferring more to friction to maintain load levels. Figure 46 shows the typical contact element force, a measure of friction between the soil and pile. Note the gradual buildup in the two-way loading case.

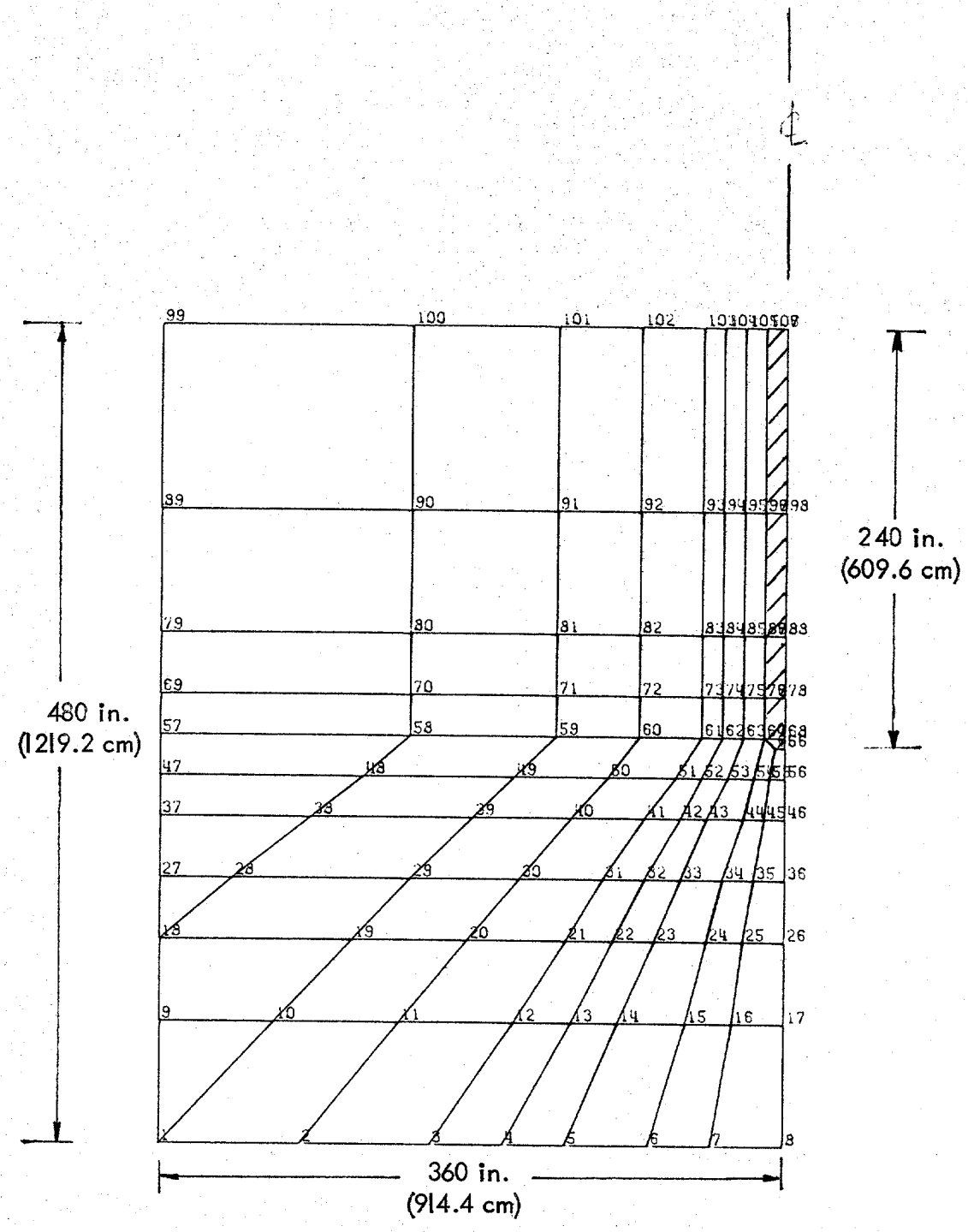

Figure 39. Mesh of pile in soil field.

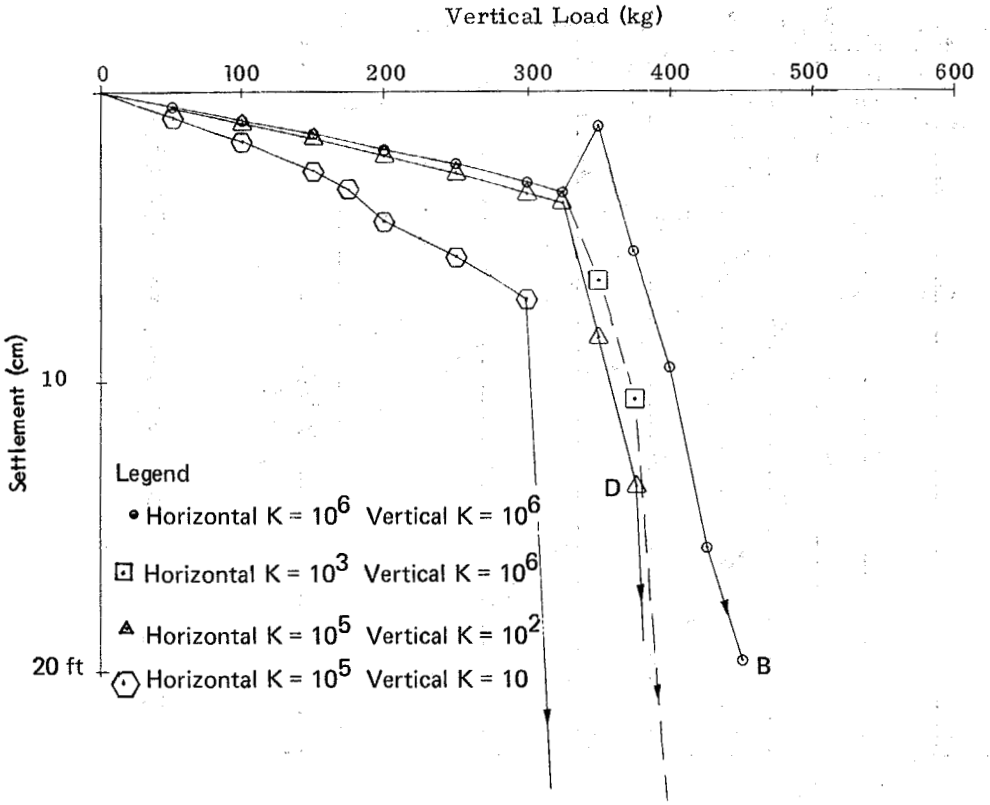

Figure 40. Load - settlement of pile.

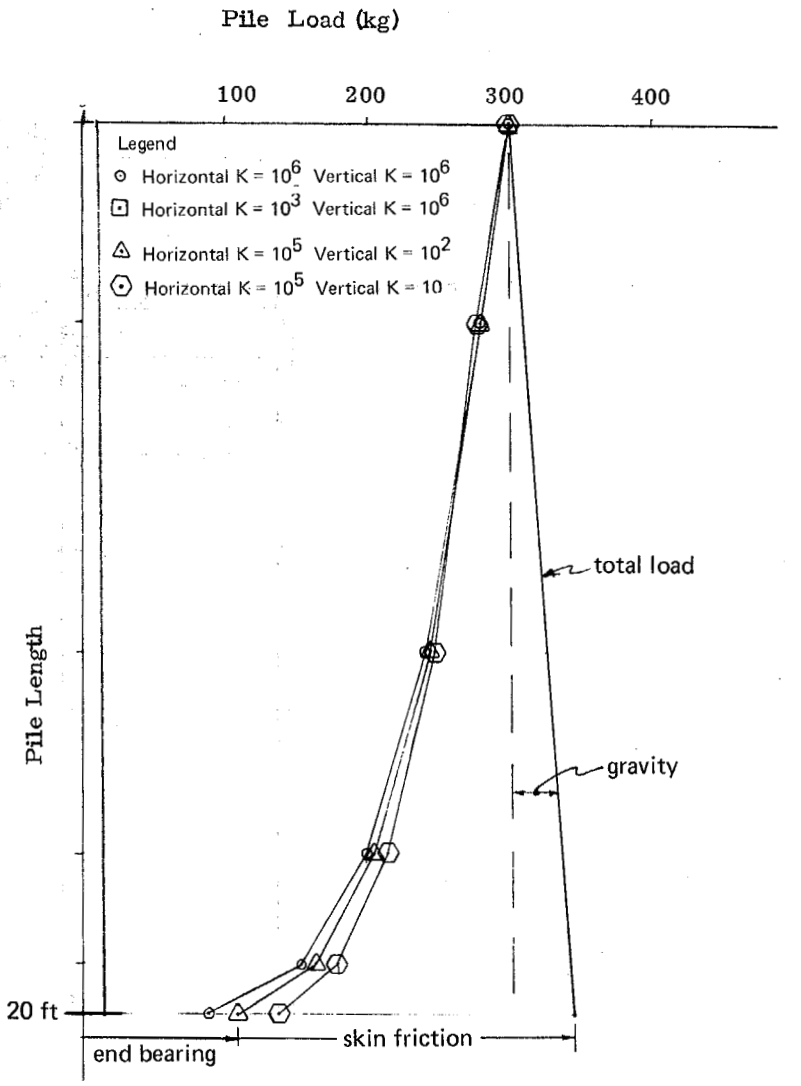

Figure 41. Distribution of force within pile.

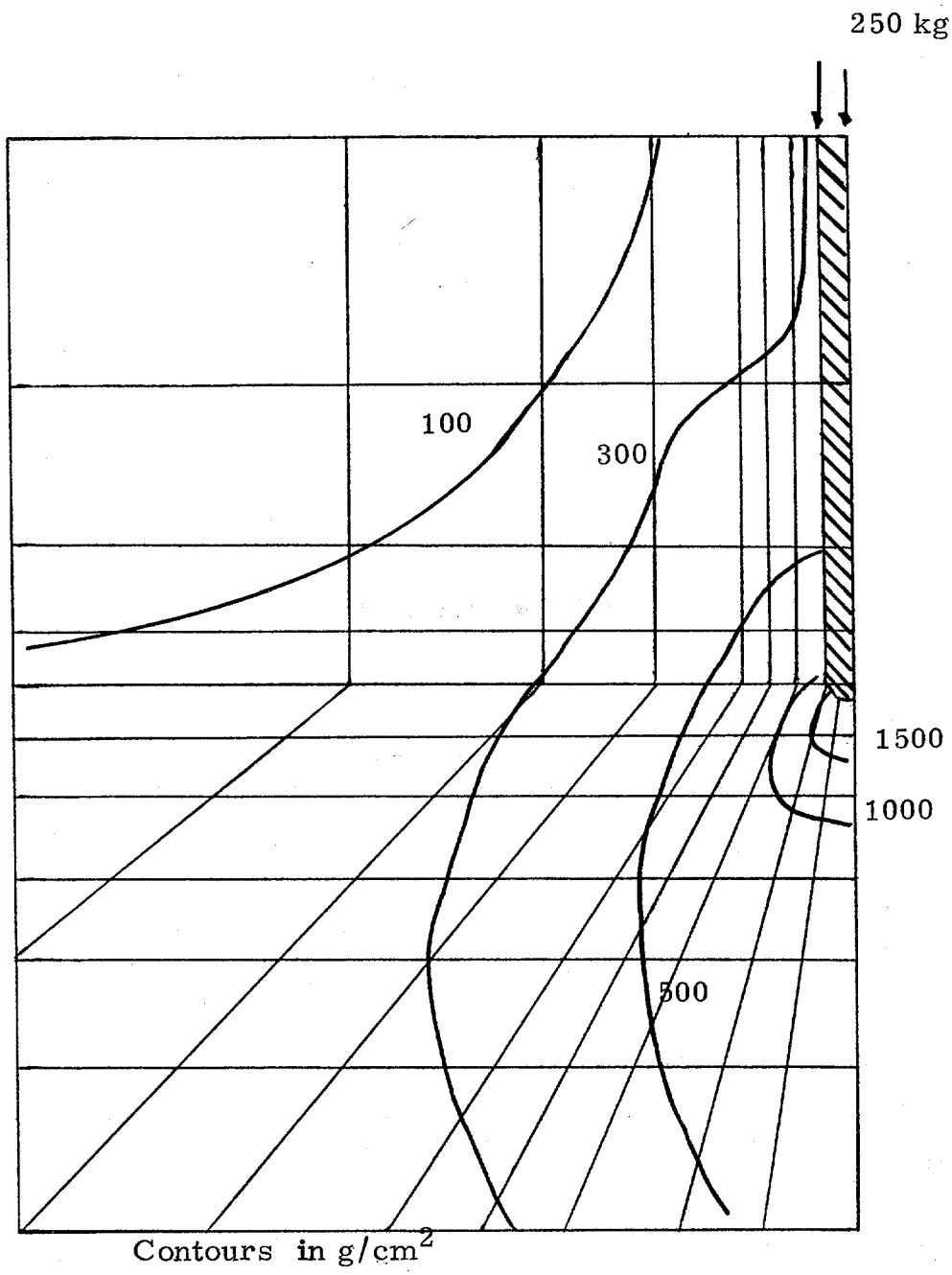

Figure 42. Contour of principal stress around pile.

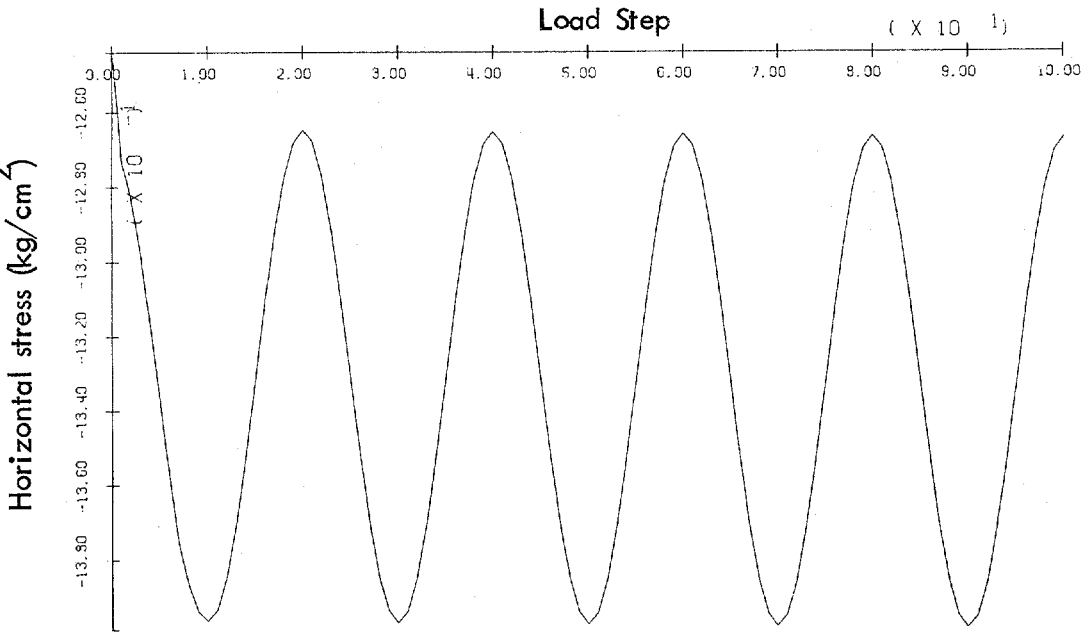

(a) Horizontal stress.

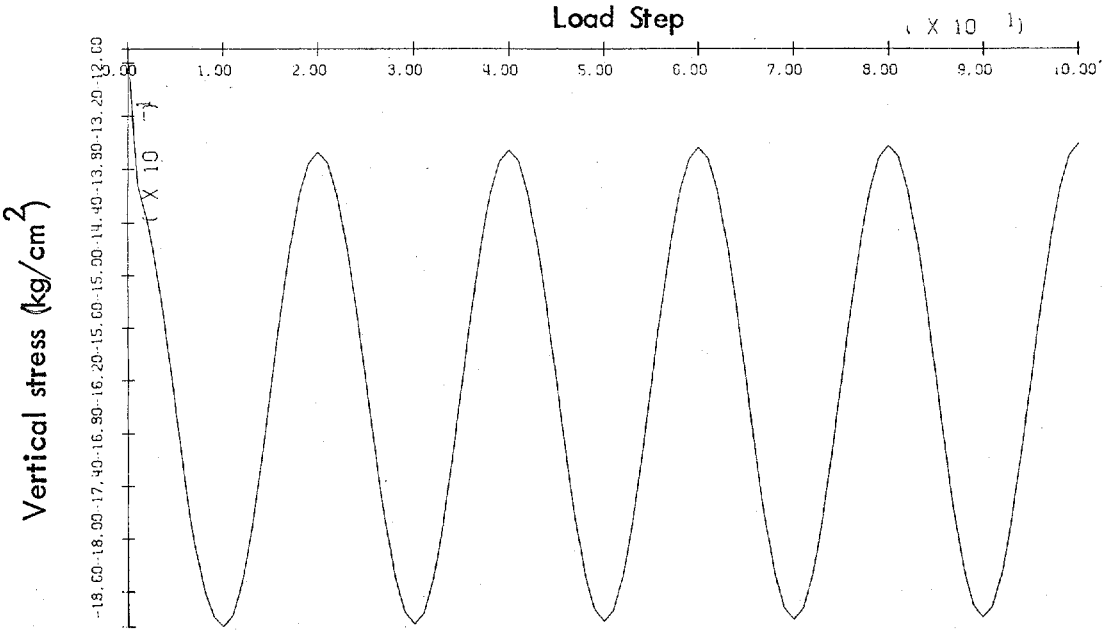

(b) Vertical stress.

Figure 43. Horizontal and vertical stress of pile in soil field - cyclic load, 0 to 50 kg (soil element beneath pile tip).

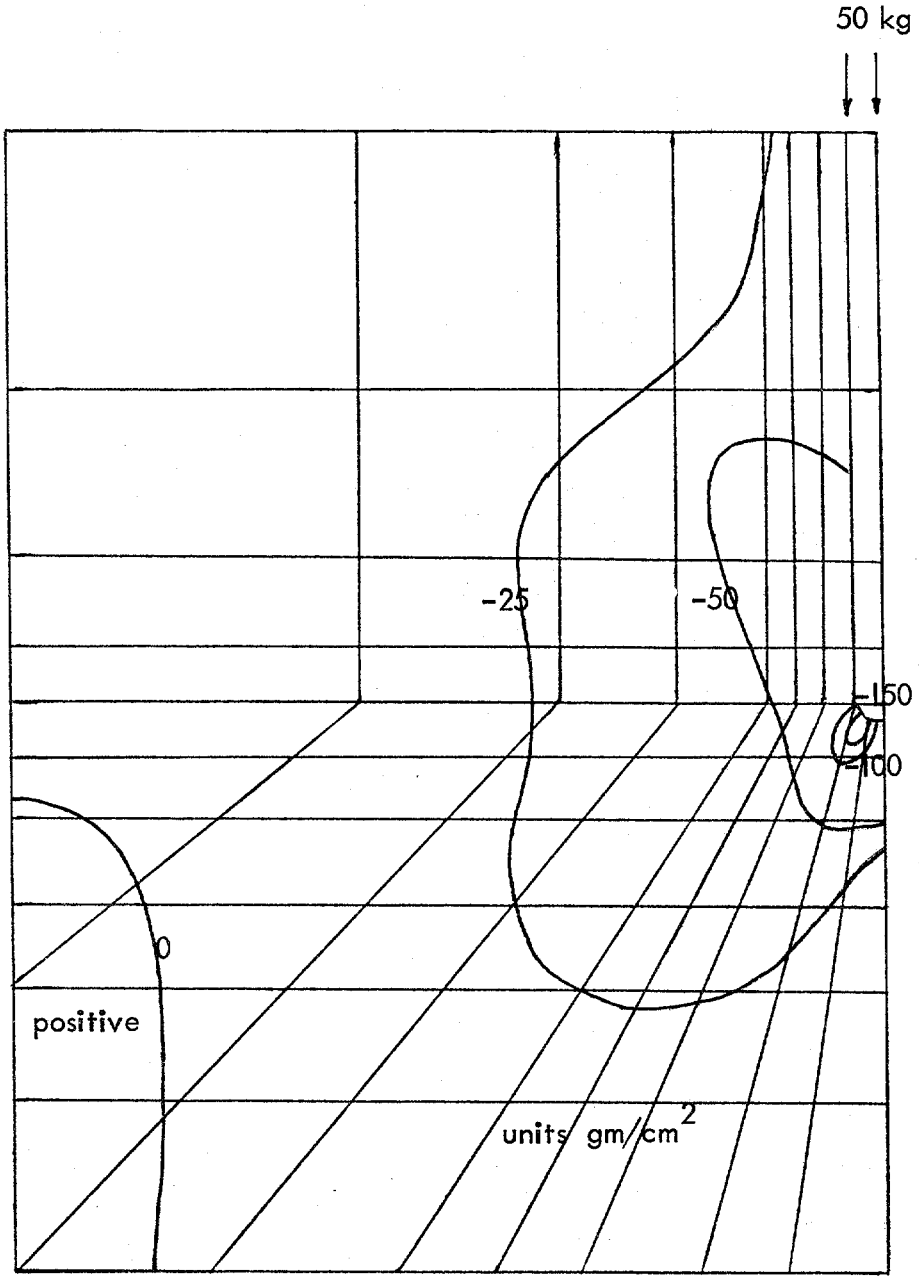

Figure 44. Shear stress contours of pile in soil field - cyclic load, 0 to 50 kg.

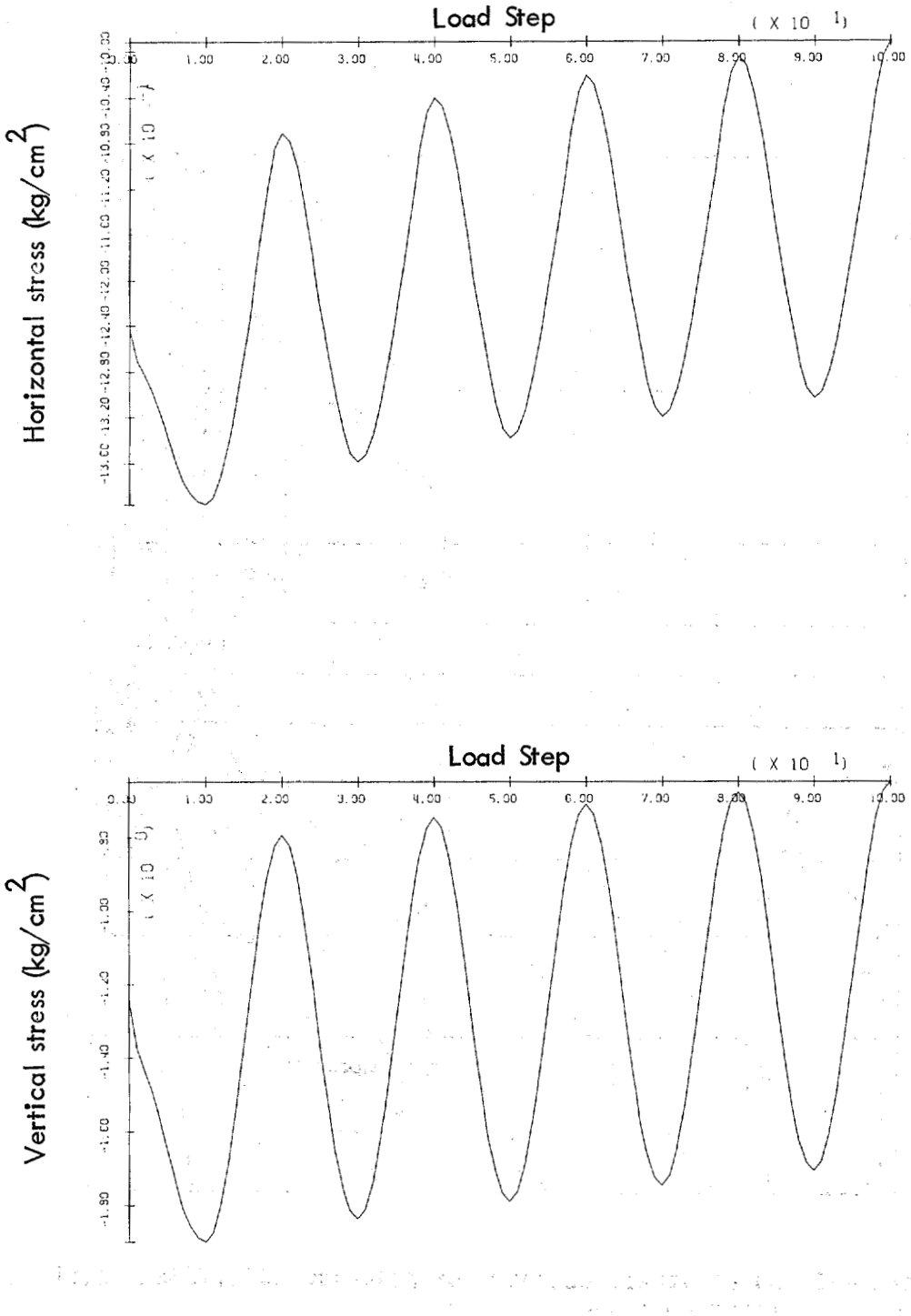

Figure 45. Horizontal and vertical stress of pile in soil field - cyclic load, -50 to 50 kg (soil element beneath pile tip).

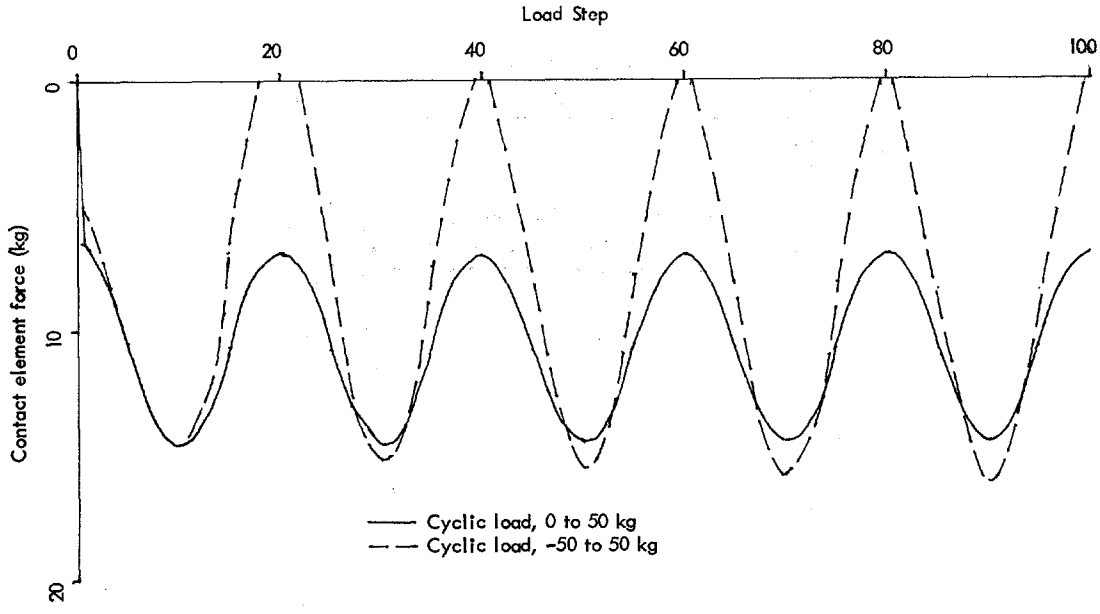

Figure 46. Friction force in pile in soil field with cycle loads of 0 to 50 and -50 to 50 kg.

The loading was increased to about 40% of yield. Figure 47 shows the distribution of force within the pile for both one-way and two-way loading for the first and fifth cycles. Note the increase in friction loading in the pile with two-way loading, showing the degradation with cyclic loading. Note also that for both cases the friction increases more in the lower half of the pile. Figure 48 composes the typical contact element force, again showing the increase in friction with each cycle. Figures 49 and 50 show the stress beneath the pile tip. Both drop off with each cycle; however, the two-way loading does so at a faster rate. Figure 51 shows the pile settlements for both cases. Note that the change in settlement between the first and fifth cycle is over four times greater for the two-way loading. Figure 52 shows the deformed mesh for the one-way loading; the mesh would be similar for the two-way loading.

The loading was increased to 80% of pile capacity, and the one-way loading case was tried. This load exceeds the friction capacity by itself, so two-way loading could not be used. Figure 53 shows the stress beneath the pile tip, and Figure 54 shows the deformed mesh. Failure occurs between steps 70 and 80. Figure 55 shows the shear stress contours around the pile at steps 10 and 70. More stress is transferred from tip end bearing to side friction.

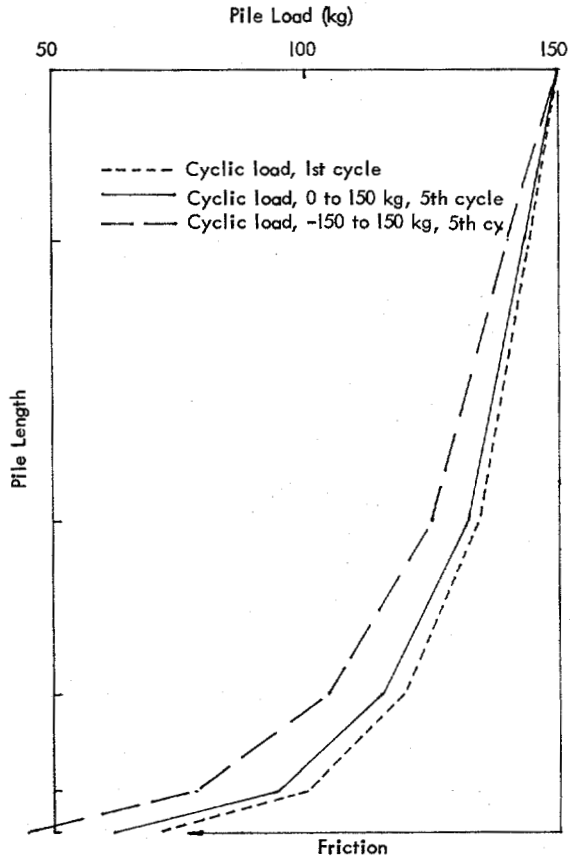

Figure 47. Distribution of force within pile, first and fifth cyclic loads.

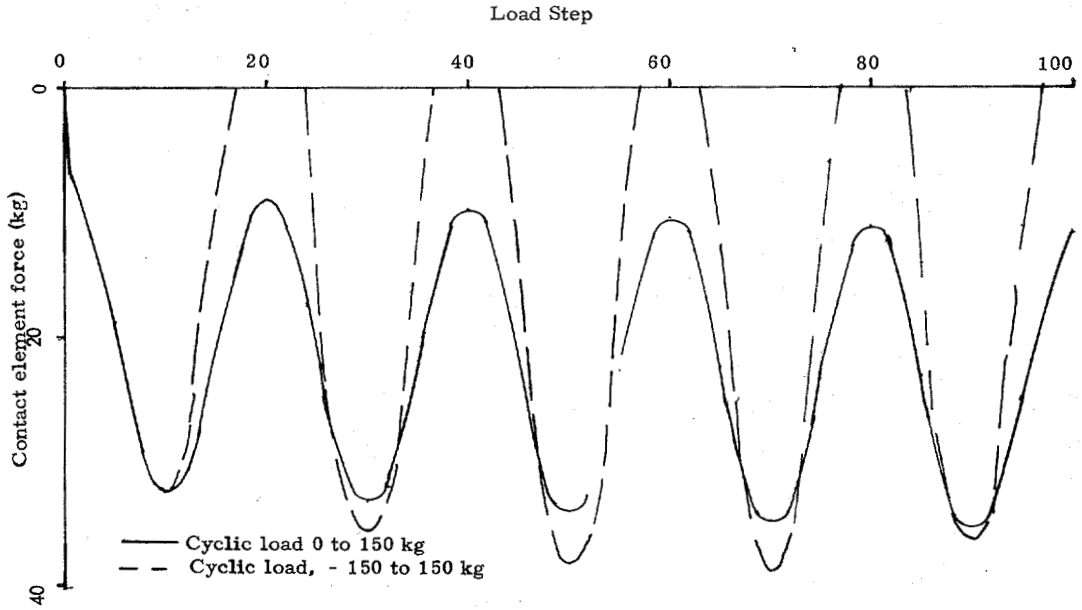

Figure 48. Friction force in pile in soil field with cyclic loads of 0 to 150 and -150 to 150 kg.

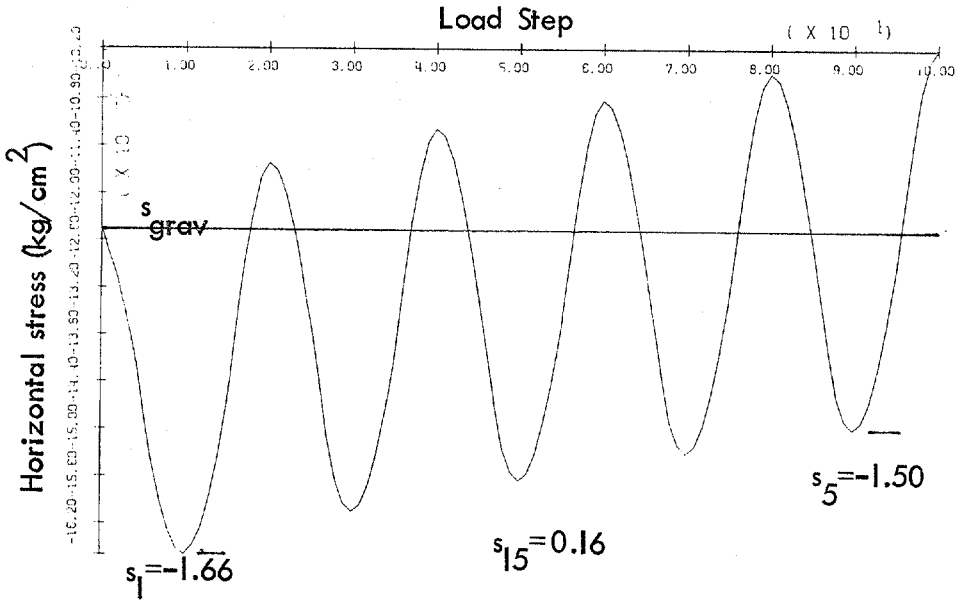

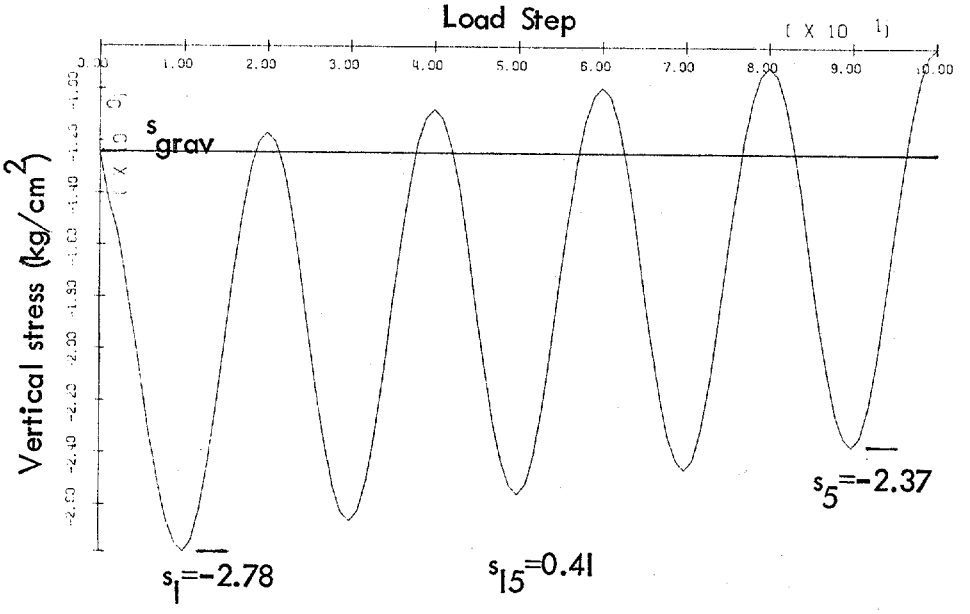

Figure 49. Pile in soil field - cyclic load, 0 to 150 kg (soil element beneath pile tip).

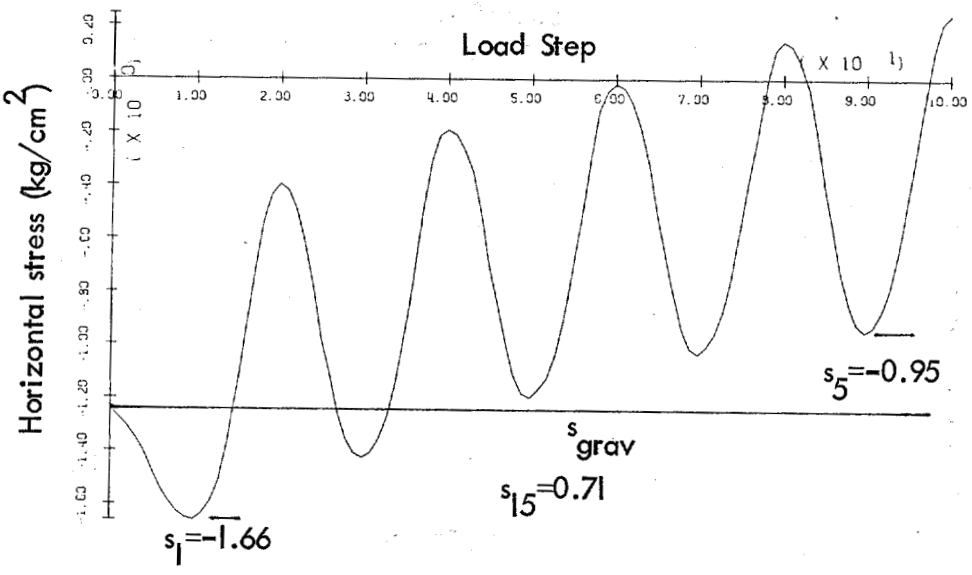

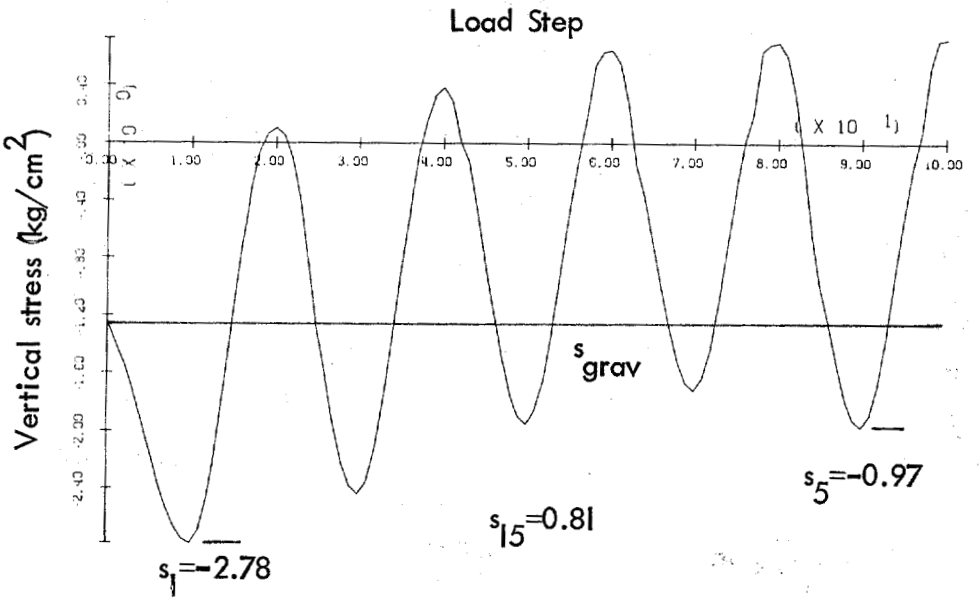

Figure 50. Pile in soil field - cyclic load, -150 to 150 kg (soil element beneath pile tip).

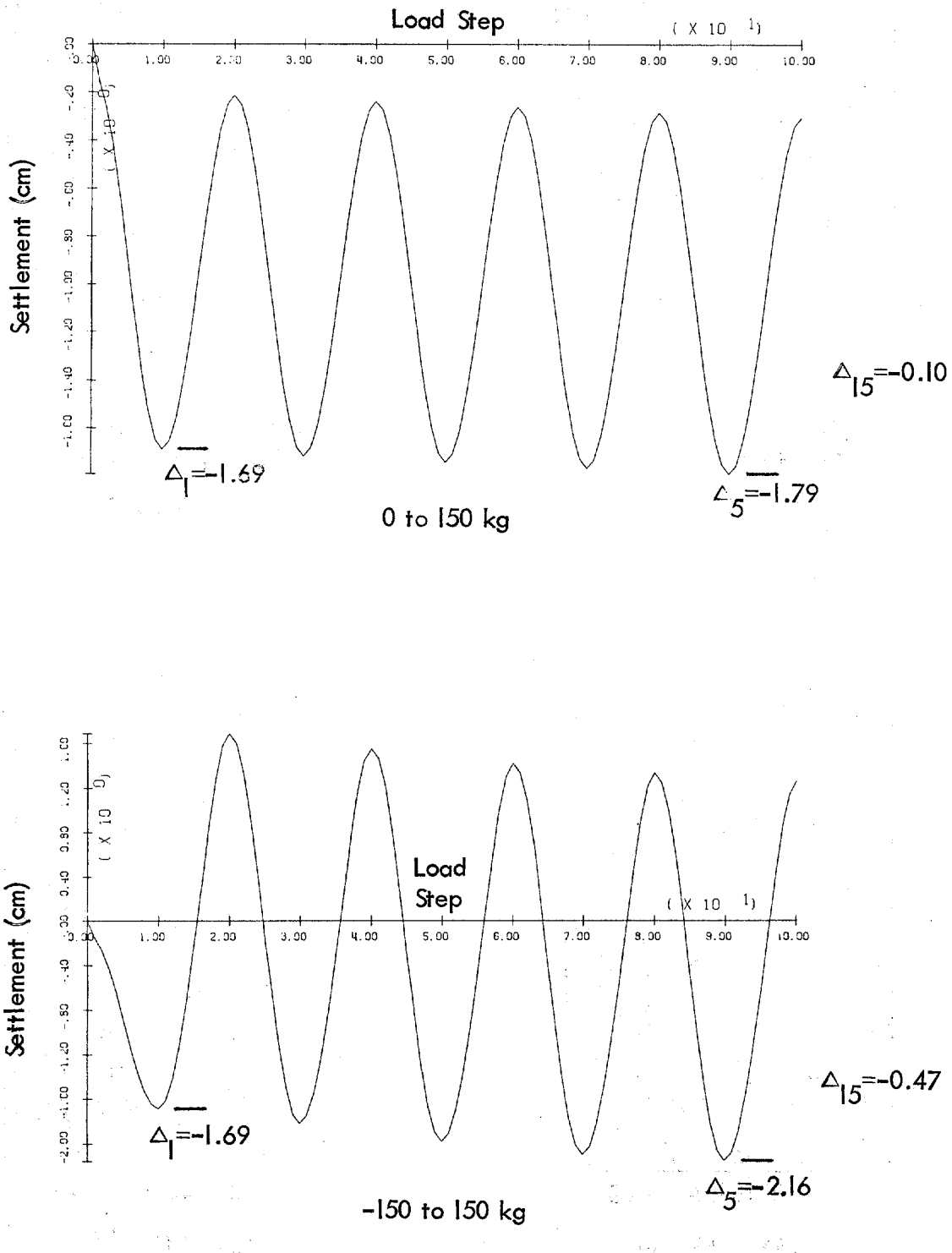

Figure 51. Pile in soil field - cyclic load (pile settlement).

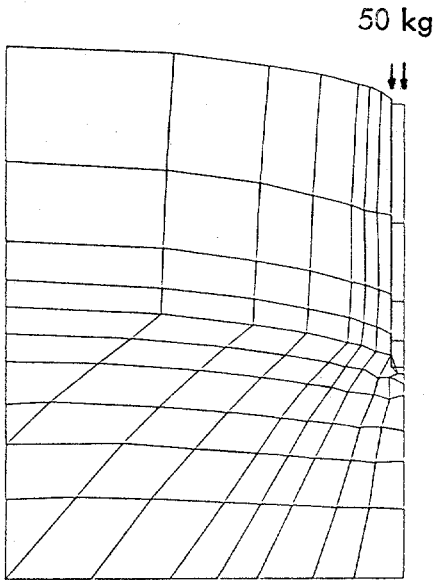

Scale factor = 1.25

(a) Step 10.

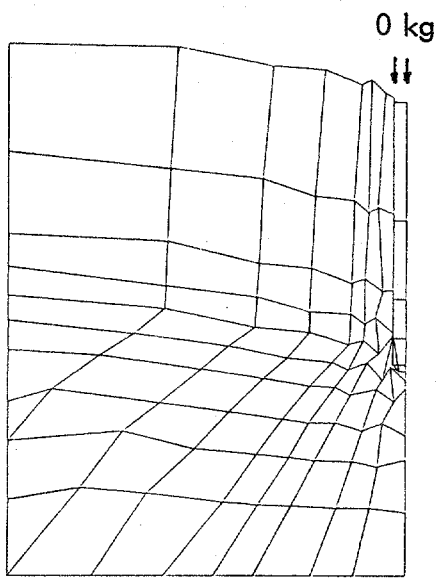

Scale factor = 0.25

(b) Step 20.

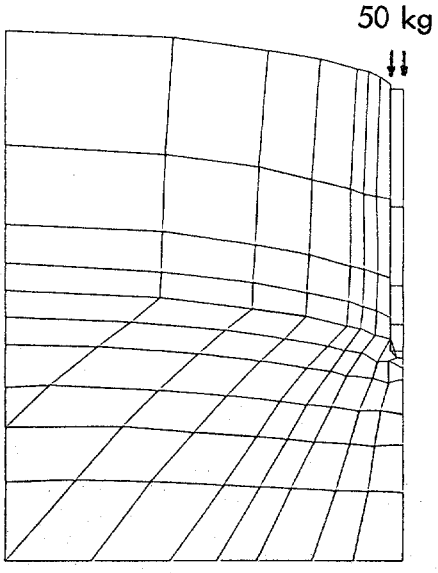

Scale factor = 1.25

(c) Step 30.

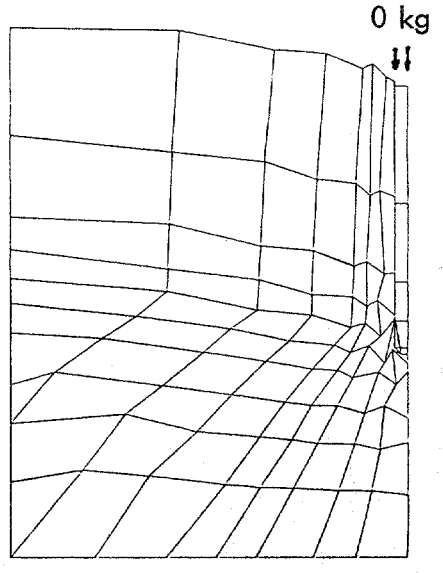

Scale factor = 0.25

(d) Step 40.

Figure 52. Deformed mesh - cyclic load, 0 to 50 kg.

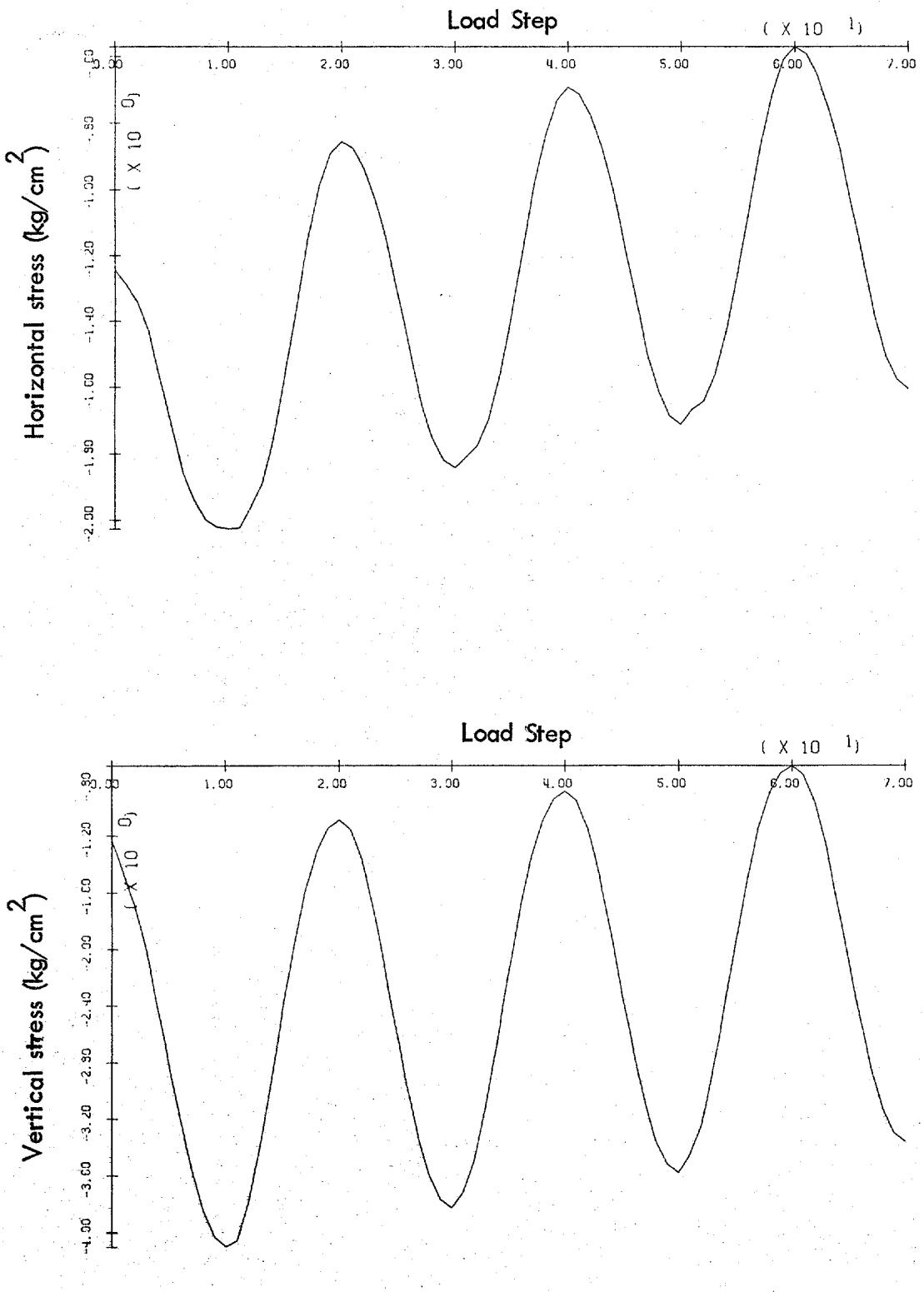

Figure 53. Pile in soil field - cyclic load, 0 to 300 kg (soil element beneath pile tip).

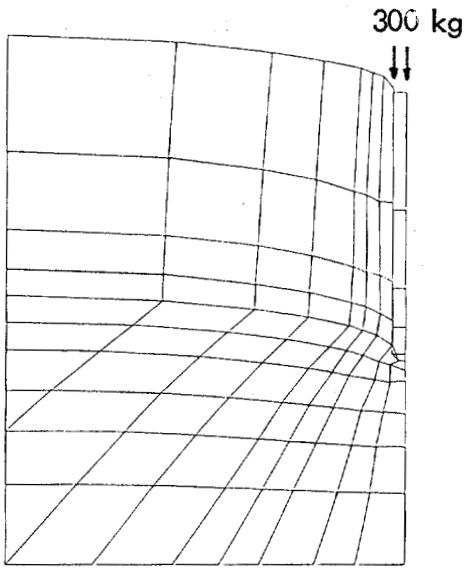

Scale factor = 7.05

(a) Step 10.

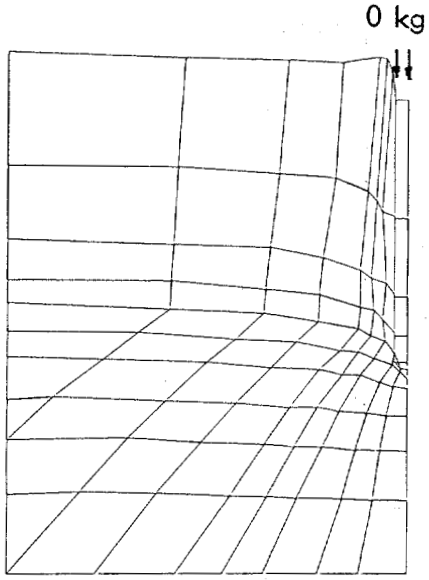

Scale factor = 1.13

(b) Step 20.

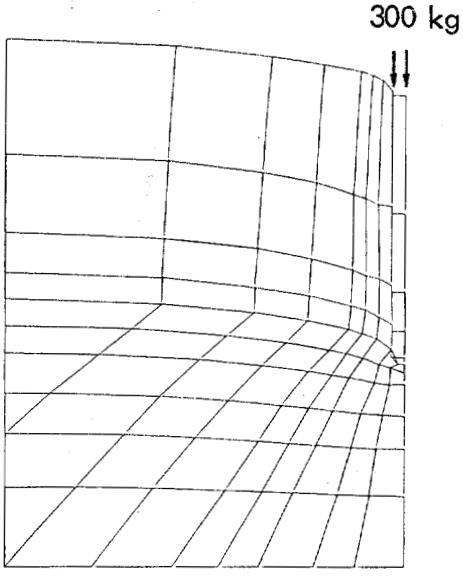

Scale factor = 7.36

(c) Step 30.

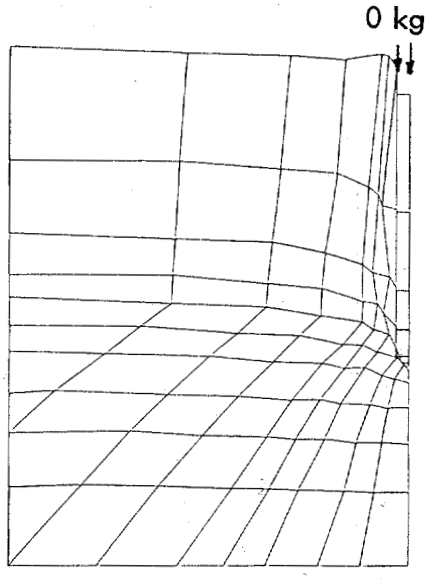

Scale factor = 1.33

(d) Step 40.

Figure 54. Deformed mesh - cyclic load, 0 to 300 kg.

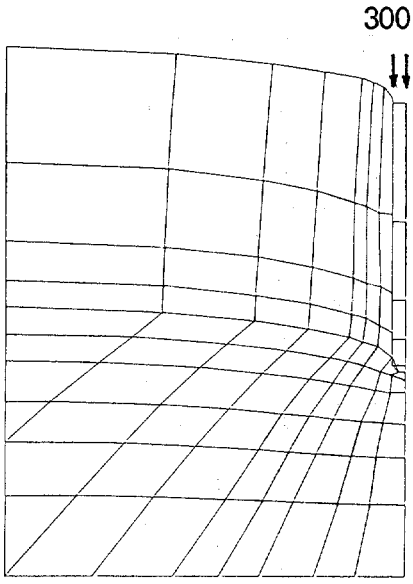

Scale factor = 7.58

(e) Step 50.

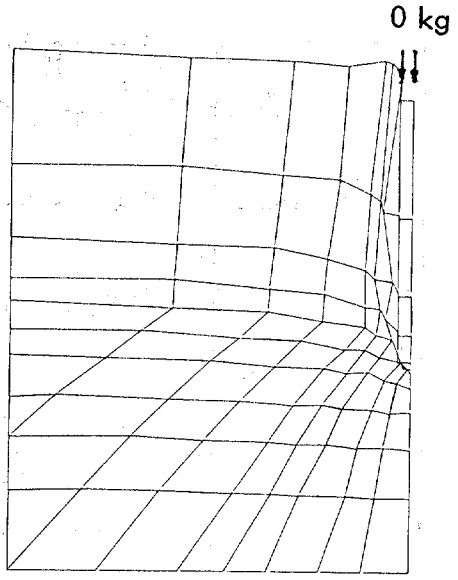

Scale factor = 1.52

(f) Step 60.

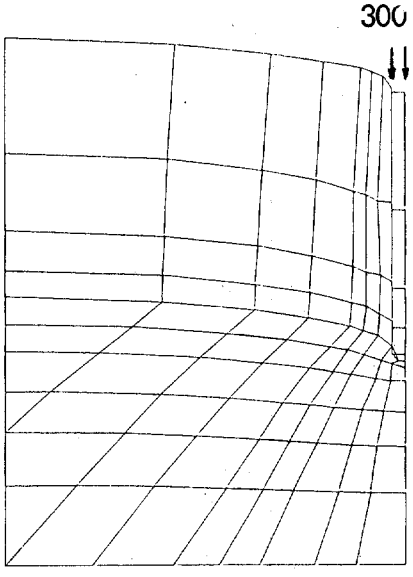

Scale factor = 7.79

(g) Step 70.

Failure

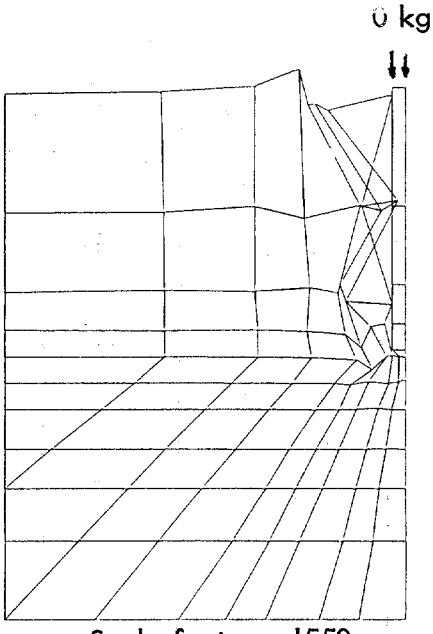

Scale factor = 1550

(h) Step 80.

Figure 54. Continued.

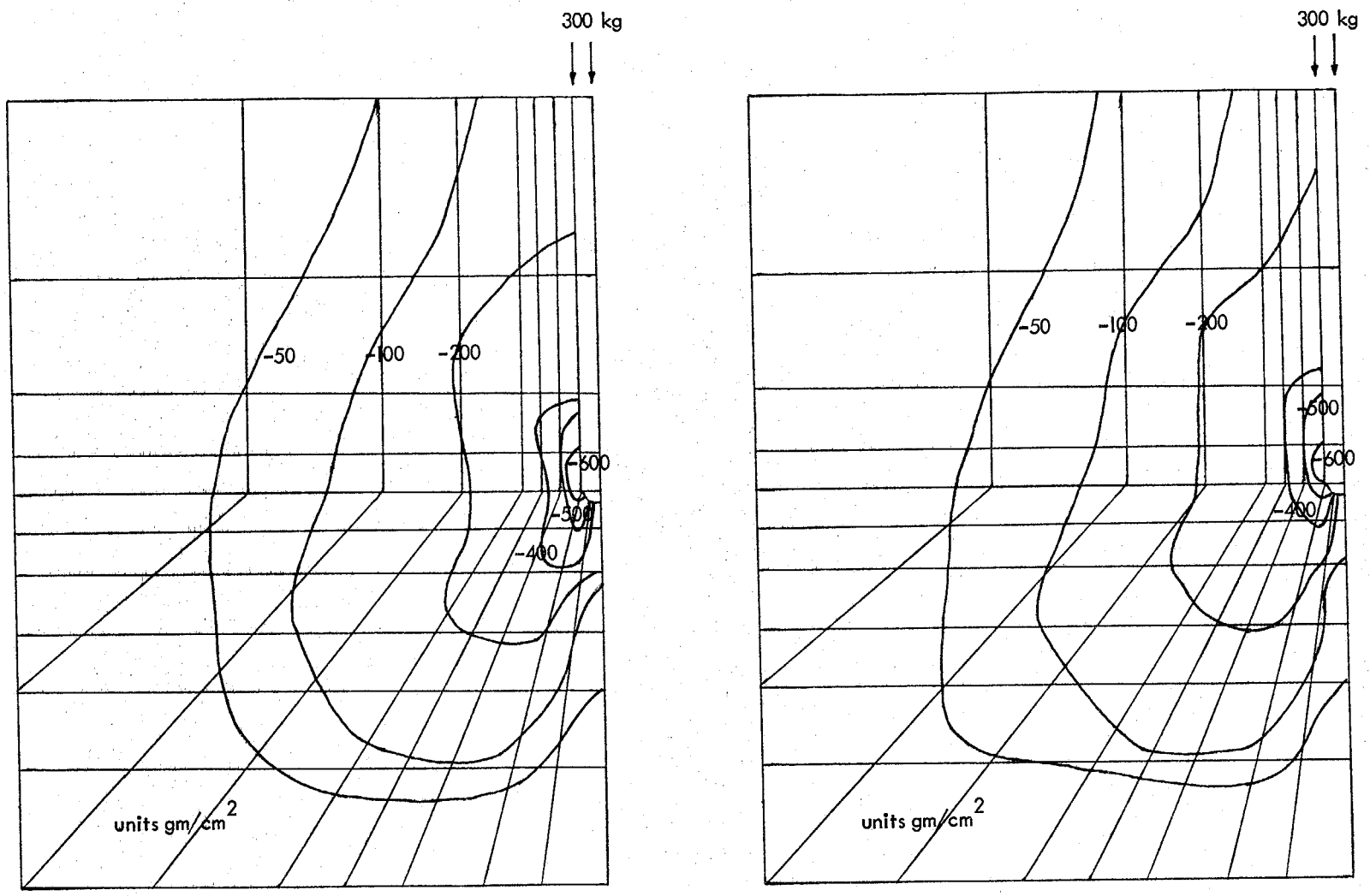

(a) Step 10.

(b) Step 70.

Figure 55. Pile in soil field - cyclic load, 0 to 300 kg, shear stress contours.

The cyclic results clearly show the degradation of the pile under cyclic loading. Results show the two-way loading causes more degradation, as expected. The model appears to be performing well in predicting the qualitative pile behavior, particularly the settlements (Figures 37 and 51).

The pile problems were repeated for the undrained case in which the water table was at the surface. Figure 56 shows the load settlement curve. The original load increment used in the drained problem above was too coarse for the undrained problem and produced an instability at yielding. The load step was reduced, and the solution proceeded in a satisfactory manner. The pile capacity was about 250 kg, lower than the 350 kg in the drained case. The loading was cycled in one-way and two-way conditions. Figure 57 presents the distribution of force within the pile, showing the increase in friction with cycling, as with the drained case. Friction is slightly greater in this case. Figures 58 and 59 show the soil stress beneath the pile. The end bearing stress drops off with cycling, showing the shift to friction. The two-way loading has a faster degradation, as clearly shown in Figure 60, which shows the settlement. The two-way loading produces a more permanent settlement differential after the fifth cycle. Figure 61 shows the pore pressure in the soil beneath the pile tip. The pore pressure rises to about three-quarters of the continuing stress and then drops off as the load is shifted to friction on the sides. Figure 62 shows the friction force. Note the degradation effects with cycling as load drops off with each cycle.

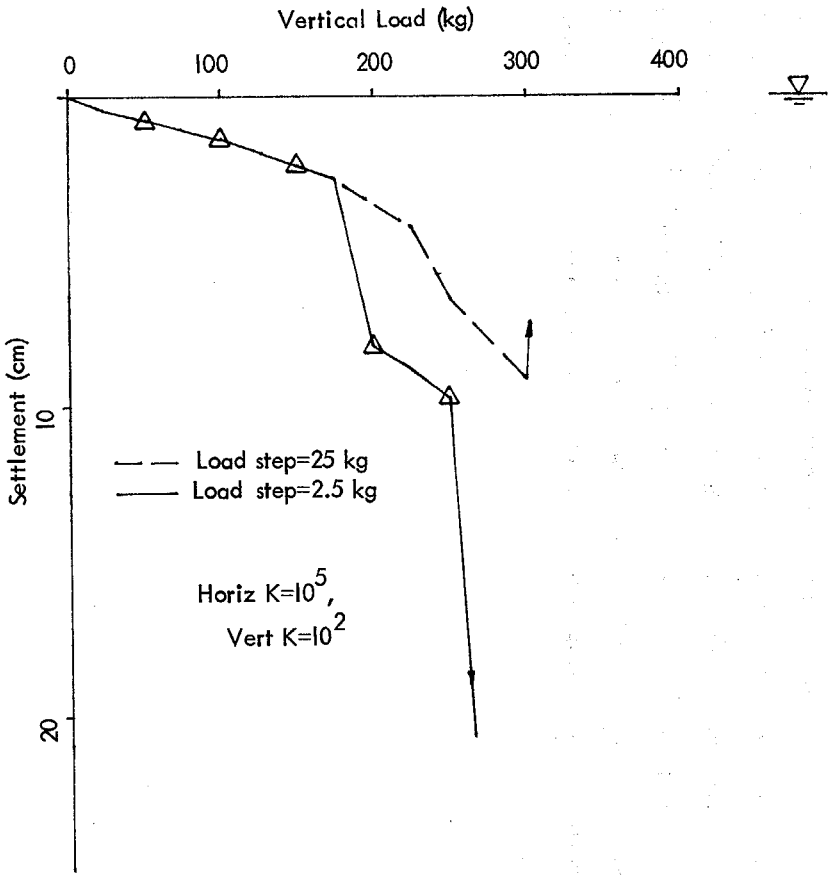

Figure 56. Load-settlement of pile (with water table).

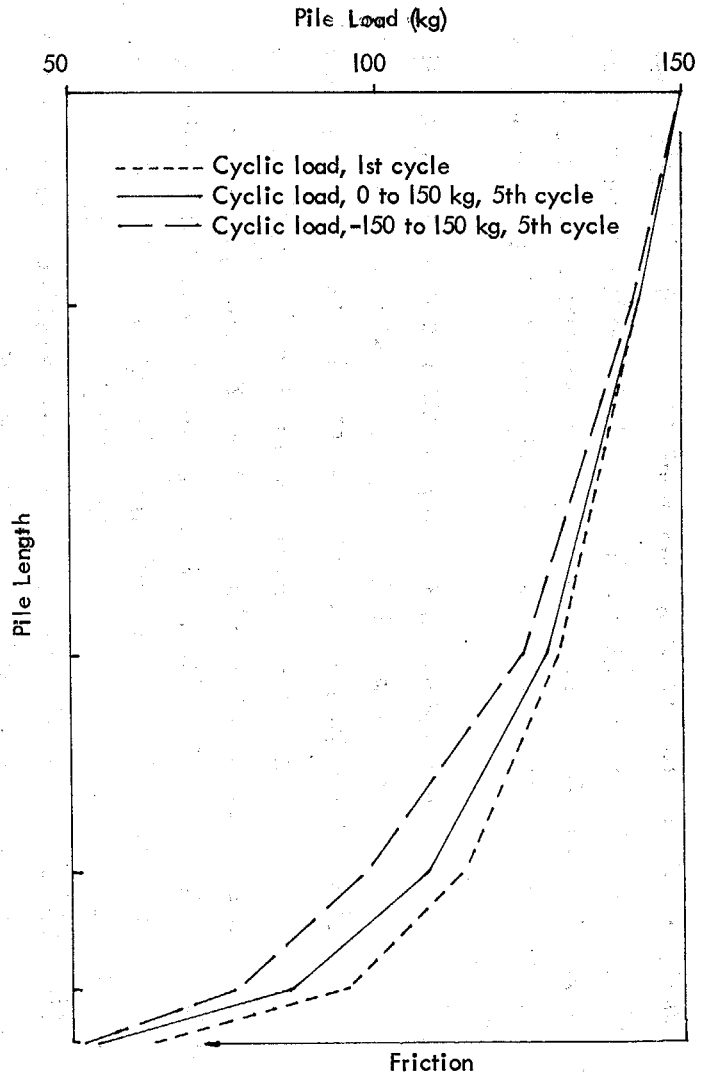

Figure 57. Distribution of force within pile, cyclic load (with water table).

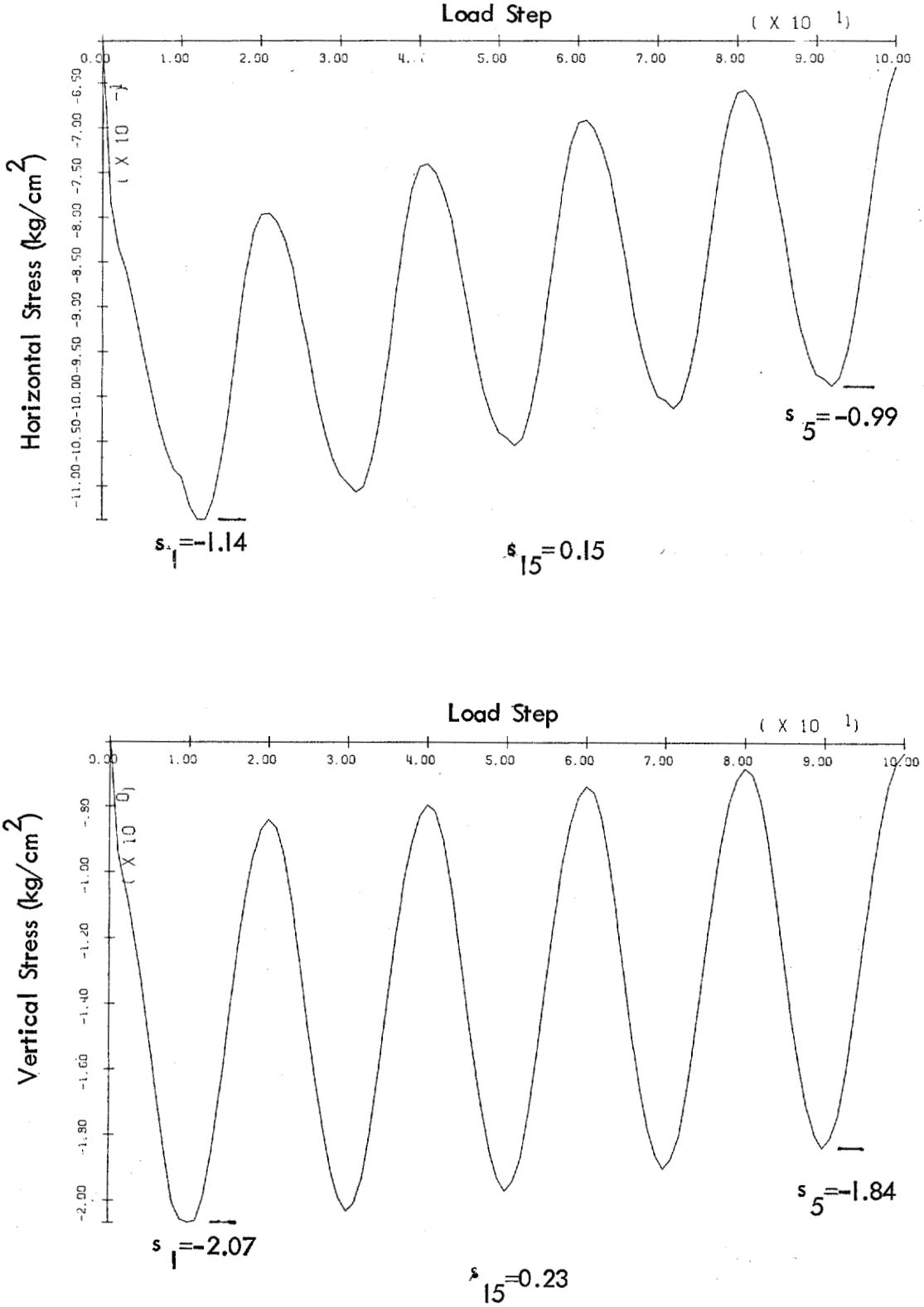

Figure 58. Pile in soil field - cyclic load, 0 to 150 kg (soil element beneath pile tip) (with water table).

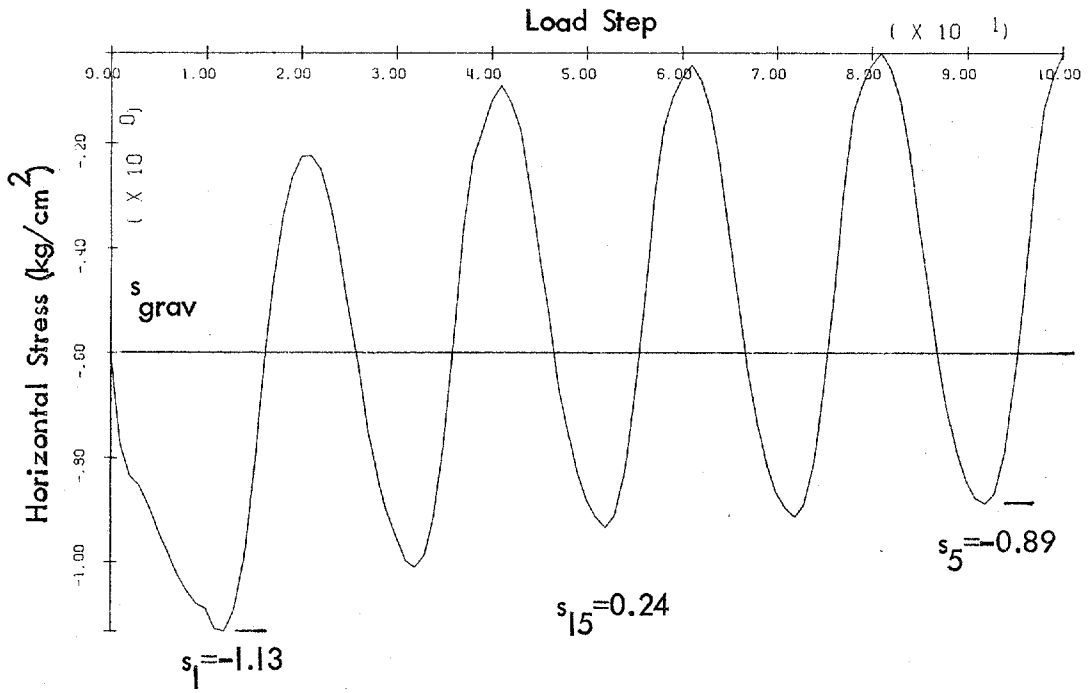

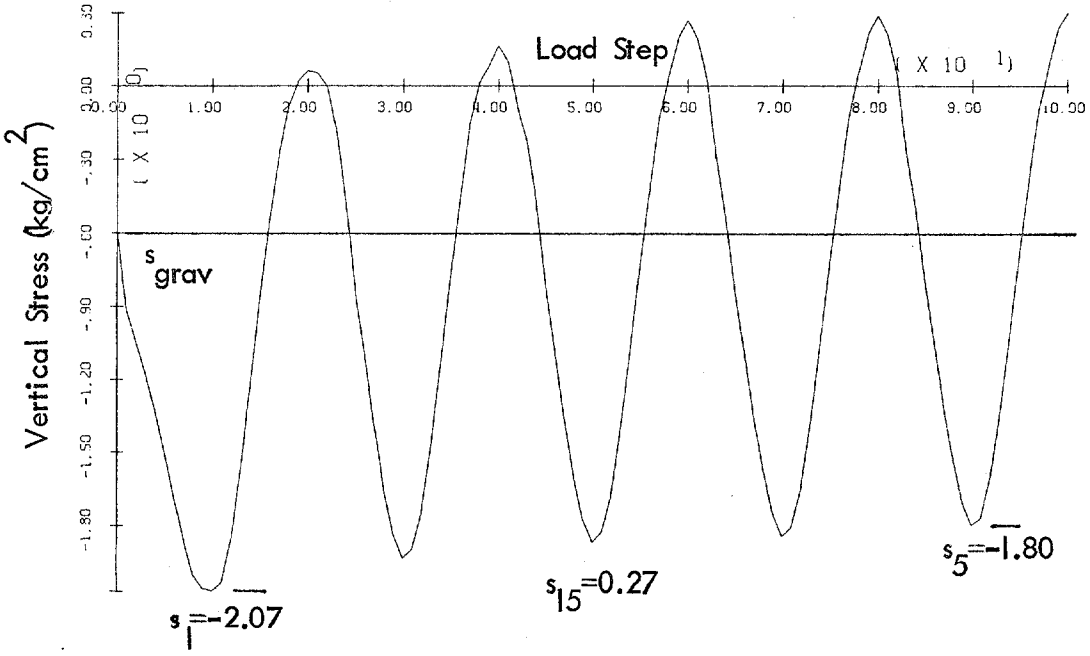

Figure 59. Pile in soil field - cyclic load, -150 to 150 kg (soil element beneath pile tip) (with water table).

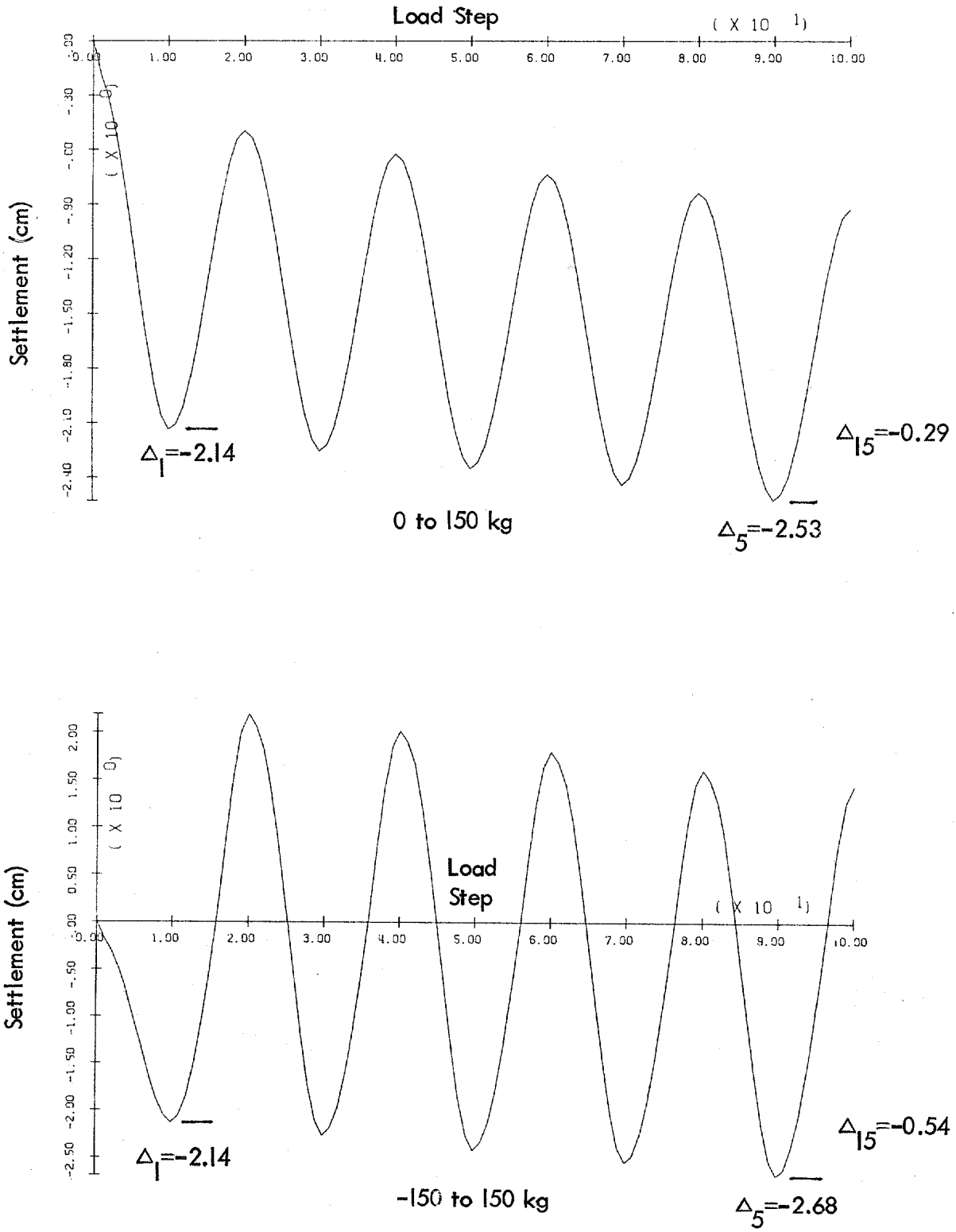

Figure 60. Pile in soil field - cyclic load (pile settlement) (with water table).

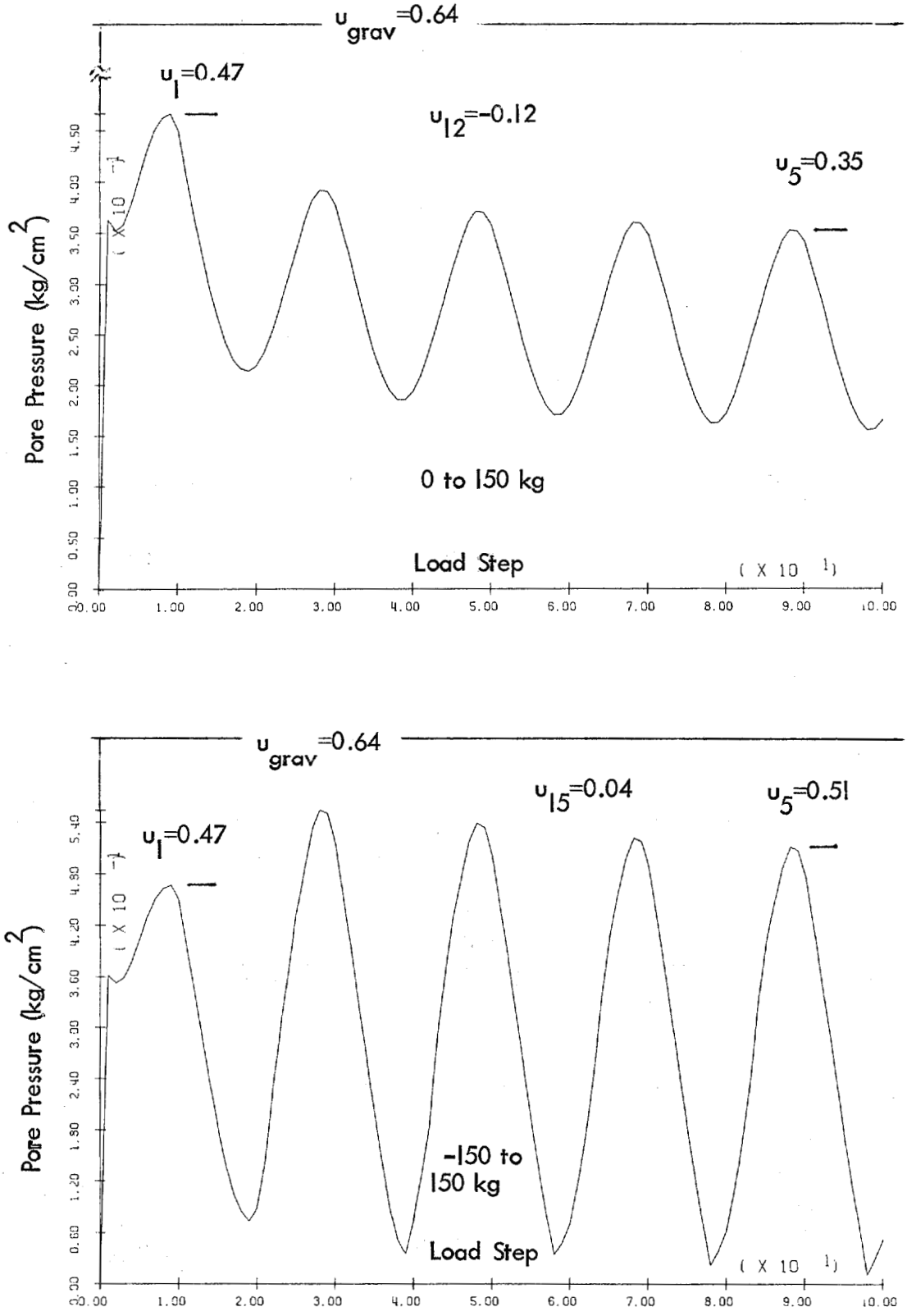

Figure 61. Pile in soil field - cyclic load (soil element beneath pile tip) (with water table).

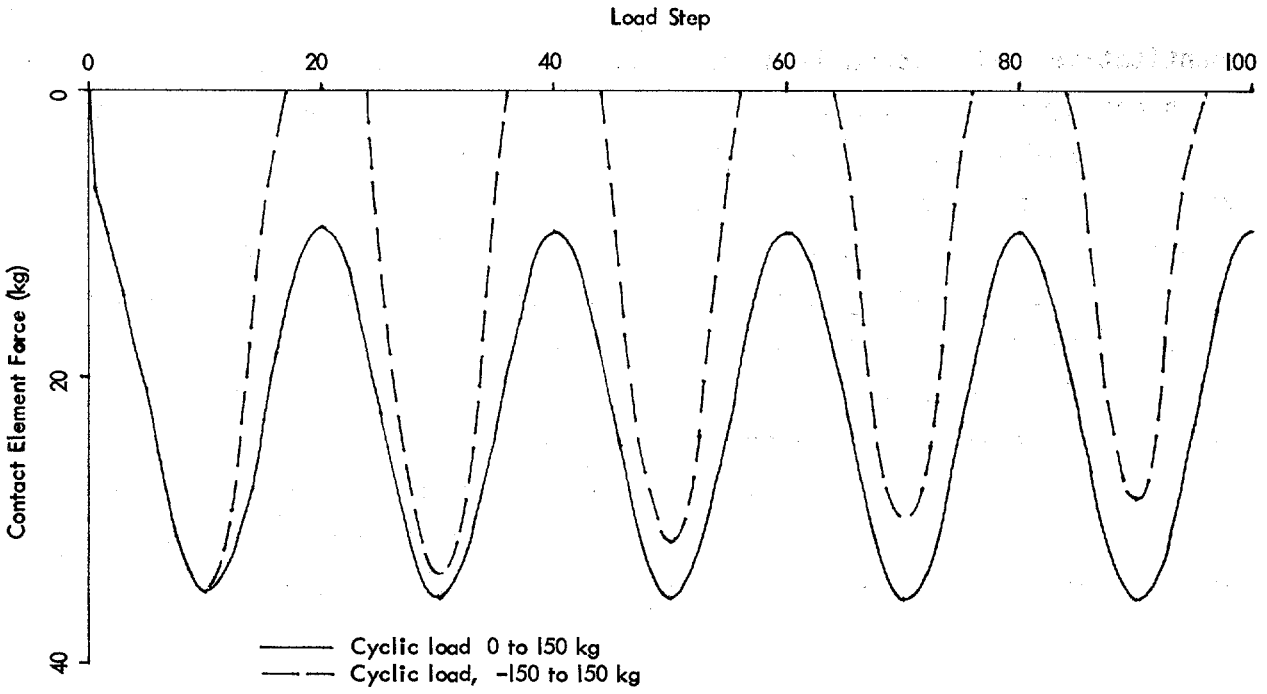

Figure 62. Pile in soil field - friction force in pile (with water table).

CONCLUSION

In this work the accuracy and ability of the Prevost soil model has been compared to laboratory test data. Results show favorable agreement. The model has been implemented into a finite element code of considerable significance. The finite element formulation allows for computation of effective stresses, pore pressures, and fluid flow under static and transient loadings. The material properties required to utilize the Prevost soil model are determined by conventional static triaxial compression and extension tests. Once these test data have been obtained, the formulations of required input parameters to quantify the properties of the soil are determined by an automated procedure.

Several demonstration problems illustrating the cyclic degradation capability of the soil model have been performed with successful results. At this point the model has been shown to agree reasonably well with laboratory tests which impose known simple loading states. Actual data of field behavior is very limited. The demonstration cases show the model performs consistently with field experience; however, more

quantitative data comparison is required. The soil properties are dependent upon the stress-state existing, which is a function of the type of loading condition or structure constructed at a site. Thus, actual case studies must have the complexity of evaluating material properties correctly before evaluation of response under load can be evaluated. In addition, verification of the model under more complex stress states in which drainage occurs is required.

It is recommended that this procedure be tried in a field study where actual field data can be obtained and utilized in a demonstration boundary value case study. Validation of the model and code in a quantified environment should be performed. A suitable bench mark must be obtained upon which analytical results can be compared.

ACKNOWLEDGMENTS

Professor J.H. Prevost, Princeton University, developed the effective stress soil model used in this study and authored the code DYNAFLOW. He also provided considerable guidance and assistance in conducting this study. Professor P. Lade, UCLA, performed basic soil tests. Dr. R. Ladd, Woodward-Clyde Consultants, also performed a series of soil tests. The authors gratefully acknowledge their assistance.

The Minerals Management Service provided partial funding for this work. Mr. C. Smith was Program Manager.

REFERENCES

1. Office of Naval Research Natural Hazards Review Panel. General review of seismic hazard to selected naval installations, ONR, Washington, D.C., Jan 1974.

2. J. Forrest and J.M. Ferritto. An earthquake analysis of the liquefaction potential at the Naval Air Station, North Island, Naval Civil Engineering Laboratory, Technical Report R-847. Port Hueneme, Calif., Sep 1976.

3. J.M. Ferritto. The effective stress soil model, Naval Civil Engineering Laboratory, Technical Memorandum M-51-81-12. Port Hueneme, Calif., Aug 1981.

4. J.M. Ferritto and R.T. Nakamoto. The effective stress soil model, Naval Civil Engineering Laboratory, Technical Memorandum M-51-82-07. Port Hueneme, Calif., Sep 1982.

5. R. Ladd. Static and cyclic triaxial testing program on Banding sand, Volumes I and II, Woodward-Clyde Consultants, Clifton, N.J., Apr 1983. (Contract Report No. N62583/83 M R077)

6. J.M. Ferritto and R.T. Nakamoto. Utilization of the Prevost soil model for soil-structure problems, Naval Civil Engineering Laboratory, Technical Memorandum M-51-83-09. Port Hueneme, Calif., Jun 1983.

7. J.H. Prevost and T.J.R. Hughes. "Finite element solution of boundary value problems in soil mechanics," in Proceedings of International Conference on Soils Under Cyclic and Transient Loading, Swansea, United Kingdom, Jan 1980.

8. _____. "Mathematical modeling of cyclic soil behavior," Earthquake Engineering and Soil Dynamics. New York, N.Y., American Society of Civil Engineers, Jun 1979.

9. J.H. Prevost. Constitutive equations for pressure sensitive soils, theory, numerical implementation, and examples. Princeton University, N.J., unpublished report for Naval Civil Engineering Laboratory, Jan 1982.

10. _____. "DYNAFLOW: A nonlinear transient finite element analysis program," Princeton University, Department of Civil Engineering. Princeton, N.J., 1981.

11. Soil mechanics, foundation and earth structures, Naval Facilities Engineering Command, NAVFAC DM 7. Alexandria, Va., Mar 1971.

12. L.C. Reese and M.W. O'Neill. "Field tests of bored piles in Beaumont clay," American Society of Civil Engineers Annual Meeting, Chicago, Ill., 1969. (Preprint 1008)

13. H. Peterson. "Application of finite element method in the analysis of contact problems," in Proceedings of the International Conference on Finite Elements in Nonlinear Solids and Structural Mechanics, Geilo, Norway, vol 2, Aug 1977.

14. L.R. Herrmann. "Nonlinear finite element analysis of frictional systems," in Proceedings of the International Conference on Finite Elements in Nonlinear Solids and Structural Mechanics, Geilo, Norway, vol 2, Aug 1977.

15. L.R. Herrmann and Z. Al-Yassin. "Numerical analysis of reinforced soil systems," American Society of Civil Engineers National Spring Convention and Continuing Education Program, Pittsburgh, Pa., Apr 24-28, 1978. (Preprint 3125)

16. L.R. Herrmann. "Finite element analysis of contact problems," Journal of Engineering Mechanics Division, American Society of Civil Engineers, vol 104, EM5, Oct 1978.

17. H.G. Poulos. "Cyclic axial response of single pile," Journal of the Geotechnical Engineering Division, American Society of Civil Engineers, vol 107, GT1, Jan 1981.

18. _____. "Development of an analysis for cyclic axial loading of piles," Third International Conference on Numerical Methods in Geomechanics, Aachen, Germany, vol 4, Rotterdam, 1979.

19. P.J. Valent. Coefficient of friction between calcareous sands and some building materials, and their significance, Civil Engineering Laboratory, Technical Note N-1541. Port Hueneme, Calif., Jan 1979.

BIBLIOGRAPHY

Prevost, J.H. (1977). "Mathematical modeling of monotonic and cyclic undrained clay behavior," International Journal Numerical and Analytical Methods in Geomechanics, vol 1, no. 2, 1977, pp 196-216.

_____ (1978a). "Anisotropic undrained stress-stain behavior of clays," Journal Geotechnical Engineering Division, American Society of Civil Engineers, vol 104, GT8, 1978, pp 1075-1090.

_____ (1978b). "Plasticity theory for soil stress-strain behavior," Journal Engineering Mechanics Division, American Society of Civil Engineers, vol 104, EM5, 1978, pp 1177-1194.

_____ (1980). "Constitutive theory for soil," in Proceedings, NSF/NSERC North American Workshop on Plasticity and Generalized Stress-Strain Applications in Soil Engineering, Montreal, Canada, May 1980.

_____ (1981a). "DYNA-FLOW: A nonlinear transient finite element analysis program," Princeton University, Department of Civil Engineering, Report 81-SM-1. Princeton, N.J., Jan 1981.

_____ (1981b). "Consolidation of an elastic porous media," American Society of Civil Engineers, vol 107, EM1, Feb 1981, pp 169-186.

_____ (1982a). "Nonlinear anisotropic stress-strength behavior of soils," in ASTM Publication STP 740 on Shear Strength of Soils, 1982, pp 431-455.

_____ (1982b). "Nonlinear transient phenomena in saturated porous media," Computer Methods in Applied Mechanics, vol 30, no. 1, 1982, pp 3-18.

_____ (1982c). "Two-surface vs. multi-surface plasticity theories," International Journal of Numerical and Analytical Methods in Geomechanics, 1982.

_____ (1982d). "Nonlinear transient phenomena in elastic-plastic Solids," Journal Engineering Mechanics Division, American Society of Civil Engineers, 1982.

Prevost, J.H., and Hughes, T.J.R. (1978). "Analysis of gravity offshore structure foundations subjected to cyclic wave forces," in Proceedings, 1978 Offshore Technology Conference, Houston, Tex., vol 1, May 1978, pp 1809-1818.

_____ (1980). "Finite element solution of boundary value problems in soil mechanics," in Proceedings, International Symposium on Soils Under Cyclic and Transient Loading, Swansea, United Kingdom, Jan 1980, pp 263-276.

_____ (1981). "Finite element solution of elastic-plastic boundary value problems," Journal Applied Mechanics, Amercian Society of Mechanical Engineers, vol 48, no. 1, Mar 1981, pp 34-69.

Prevost, J.H., Cuny, B., Hughes, T.J.R., and Scott, R.F. (1981). "Foundations of offshore gravity structures: Analysis," Journal Geotechnical Engineering Division, American Society of Civil Engineers, vol 107, GT2, Feb 1981, pp 143-165.

DISTRIBUTION LIST

AF HQ LEEH (J Stanton) Washington, DC; PREES Washington DC
AFB AF Tech Office (Mgt & Ops), Tyndall, FL; AFESC/TST, Tyndall FL; SAMSO/MNND, Norton AFB CA; Scol of Engrng (AFIT/DET); Stinfo Library, Offutt NE
AFESC DEB, Tyndall, FL
ARMY ARRADCOM, Dover, NJ; DAEN-MPE-D Washington DC; ERADCOM Tech Supp Dir. (DELSD-L) Ft. Monmouth, NJ; HQDA (DAEN-FEE-A)
ARMY - CERL Library, Champaign IL; Spec Assist for MILCON, Champaign, IL
ARMY CORPS OF ENGINEERS MRD-Eng. Div., Omaha NE
ARMY CRREL Library, Hanover NH
ARMY ENG DIV ED-CS (S.Bolin) Huntsville, AL; HNDED-CS, Huntsville AL
ARMY ENG WATERWAYS EXP STA Coastal Eng Rsrch Cntr, Vicksburg, MS; Library, Vicksburg MS
ARMY MATERIALS & MECHANICS RESEARCH CENTER Dr. Lenoe, Watertown MA
ARMY MISSILE R&D CMD SCI Info Cen (DOC) Redstone Arsenal, AL
BUREAU OF RECLAMATION Code 1512 (C. Selander) Denver CO
CNM MAT 08L21, Washington, DC; NMAT - 044, Washington DC
CNO Code NOP-964, Washington DC; OP987J, Washington, DC
DEFENSE CIVIL PREPAREDNESS AGENCY Washington, DC
DEFENSE INTELLIGENCE AGENCY DB-4C1 Washington DC
DNA STTL, Washington DC
DTIC Defense Technical Info Ctr/Alexandria, VA
DTNSRDC Code 1706, Bethesda MD; Code 172 (M. Krenzke), Bethesda MD
FOREST SERVICE Engr Staff Washington, DC
GIDEP OIC, Corona, CA
LIBRARY OF CONGRESS Washington, DC (Sciences & Tech Div)
NAS PW (J. Maguire), Corpus Christi TX
NATL BUREAU OF STANDARDS R Chung Washington, DC
NATL RESEARCH COUNCIL Naval Studies Board, Washington DC
NAVCOASTSYSCEN CO, Panama City FL; Library Panama City, FL
NAVFACENGCOM Alexandria, VA; Code 03 Alexandria, VA; Code 03T (Essoglou) Alexandria, VA; Code 04T4 (D. Potter) Alexandria, VA
NAVFACENGCOM - CHES DIV. Code 405 Wash, DC; Code 406 Washington DC; Library, Washington, D.C.
NAVFACENGCOM - LANT DIV. Code 1112, Norfolk, VA; Library, Norfolk, VA
NAVFACENGCOM - NORTH DIV. Code 04AL, Philadelphia PA; Code 405 Philadelphia, PA
NAVFACENGCOM - PAC DIV. Library, Pearl Harbor, HI
NAVFACENGCOM - SOUTH DIV. Code 405 Charleston, SC; Code 406 Charleston, SC; Code 411 Soil Mech & Paving BR Charleston, SC; Library, Charleston, SC
NAVFACENGCOM - WEST DIV. Code 04B San Bruno, CA; Library, San Bruno, CA; RDT&ELO San Bruno, CA
NAVOCEANSYSCEN Code 4473B (Tech Lib) San Diego, CA
NAVWARCOL Dir. of Facil., Newport RI
NOAA (Mr. Joseph Vadus) Rockville, MD
NORDA Code 440 (Ocean Rsch Off) Bay St. Louis MS
NRL Code 5800 Washington, DC; Code 5843 (F. Rosenthal) Washington, DC; Code 8441 (R.A. Skop), Washington DC
NUSC DET Code EA123 (R.S. Munn), New London CT; Code TA131 (G. De la Cruz), New London CT
ONR Code 485 (Silva) Arlington, VA
PWC Code 121.1, Oakland, CA; Code 154 (Library), Great Lakes, IL; Library, Code 120C, San Diego, CA; Library, Guam; Library, Norfolk, VA; Library, Pearl Harbor, HI; Library, Pensacola, FL; Library, Subic Bay, R.P.
US DEPT OF INTERIOR MS647 (C.E. Smith), Reston, VA
U.S. MERCHANT MARINE ACADEMY Kings Point, NY (Reprint Custodian)
US DEPT OF INTERIOR Bur of Land Mgmnt Code 583, Washington DC
US GEOLOGICAL SURVEY Off. Marine Geology, Piteleki, Reston VA
USCG R&D CENTER D. Motherway, Groton CT; Library New London, CT
USDA Ext Service (T. Maher) Washington, DC; Forest Service Reg 3 (R. Brown) Albuquerque, NM
AMERICAN CONCRETE INSTITUTE Detroit MI (Library)
CLARKSON COLL OF TECH G. Batson, Potsdam NY
COLORADO STATE UNIV., FOOTHILL CAMPUS Fort Collins (Nelson)
CORNELL UNIVERSITY Ithaca NY (Serials Dept, Engr Lib.); (Dr. F.Kulnawy) Dept of Civil & Environ Engrng, Ithaca, NY
DAMES & MOORE LIBRARY LOS ANGELES, CA
DUKE UNIV MEDICAL CENTER B. Muga, Durham NC
FLORIDA ATLANTIC UNIVERSITY Boca Raton, FL (McAllister)

GEORGIA INSTITUTE OF TECHNOLOGY Atlanta GA (School of Civil Engr., Kahn)
HARVARD UNIV. Dept. of Architecture, Dr. Kim, Cambridge, MA
IOWA STATE UNIVERSITY Ames IA (CE Dept, Handy)
LEHIGH UNIVERSITY BETHLEHEM, PA (MARINE GEOTECHNICAL LAB., RICHARDS); Bethlehem PA (Fritz Engr. Lab No. 13, Beedle); Bethlehem PA (Linderman Lib. No.30, Flecksteiner)
MICHIGAN TECHNOLOGICAL UNIVERSITY Houghton, MI (Haas)
MIT Cambridge MA; Cambridge MA (Rm 10-500, Tech. Reports, Engr. Lib.); Cambridge MA (Whitman)
NY CITY COMMUNITY COLLEGE BROOKLYN, NY (LIBRARY)
OREGON STATE UNIVERSITY CORVALLIS, OR (CE DEPT, BELL); CORVALLIS, OR (CE DEPT, HICKS); Corvalis OR (School of Oceanography)
PENNSYLVANIA STATE UNIVERSITY STATE COLLEGE, PA (SNYDER); UNIVERSITY PARK, PA (GOTOLSKI)
PURDUE UNIVERSITY Lafayette IN (Leonards); Lafayette, IN (Altschaeffl); Lafayette, IN (CE Engr. Lib)
SAN DIEGO STATE UNIV. I. Noorany San Diego, CA; Dr. Krishnamoorthy, San Diego CA
SOUTHWEST RSCH INST R. DeHart, San Antonio TX
STANFORD UNIVERSITY Stanford CA (Gene)
STATE UNIV. OF NEW YORK Buffalo, NY
TEXAS A&M UNIVERSITY J.M. Niedzwecki, College Station, TX; W.B. Ledbetter College Station, TX
UNIVERSITY OF CALIFORNIA BERKELEY, CA (CE DEPT, GERWICK); BERKELEY, CA (CE DEPT, MITCHELL); Berkeley CA (R. Williamson); DAVIS, CA (CE DEPT, TAYLOR); LIVERMORE, CA (LAWRENCE LIVERMORE LAB, TOKARZ); La Jolla CA (Acq. Dept, Lib. C-075A); M. Duncan, Berkeley CA
UNIVERSITY OF DELAWARE Newark, DE (Dept of Civil Engineering, Chesson)
UNIVERSITY OF HAWAII HONOLULU, HI (SCIENCE AND TECH. DIV.)
UNIVERSITY OF ILLINOIS (Hall) Urbana, IL; Metz Ref Rm, Urbana IL; URBANA, IL (DAVISSON); URBANA, IL (LIBRARY); Urbana IL (CE Dept, W. Gamble)
UNIVERSITY OF MASSACHUSETTS (Heronemus), ME Dept, Amherst, MA
UNIVERSITY OF MICHIGAN Ann Arbor MI (Richart)
UNIVERSITY OF NOTRE DAME Katona, Notre Dame, IN
UNIVERSITY OF TEXAS Inst. Marine Sci (Library), Port Arkansas TX
UNIVERSITY OF TEXAS AT AUSTIN AUSTIN, TX (THOMPSON); Austin TX (R. Olson); Austin, TX (Breen)
UNIVERSITY OF WASHINGTON Dept of Civil Engr (Dr. Mattock), Seattle WA; SEATTLE, WA (OCEAN ENG RSCH LAB, GRAY); Seattle, WA Transportation, Construction & Geom. Div
AMETEK Offshore Res. & Engr Div
ATLANTIC RICHFIELD CO. DALLAS, TX (SMITH)
BECHTEL CORP. SAN FRANCISCO, CA (PHELPS)
BETHLEHEM STEEL CO. Dismuke, Bethelehem, PA
BRITISH EMBASSY M A Wilkins (Sci & Tech Dept) Washington, DC
BROWN & ROOT Houston TX (D. Ward)
CHAS. TL MAIN, INC. (R.C. Goyette), Portland, OR
CHEVRON OIL FIELD RESEARCH CO. LA HABRA, CA (BROOKS)
CONRAD ASSOC. Van Nuys CA (A. Luisoni)
DRAVO CORP Pittsburgh PA (Wright)
EVALUATION ASSOC. INC KING OF PRUSSIA, PA (FEDELE)
EXXON PRODUCTION RESEARCH CO Houston, TX (Chao)
FURGO INC. Library, Houston, TX
GEOTECHNICAL ENGINEERS INC. Winchester, MA (Paulding)
GRUMMAN AEROSPACE CORP. Bethpage NY (Tech. Info. Ctr)
HALEY & ALDRICH, INC. Cambridge MA (Aldrich, Jr.)
NUSC DET Library, Newport, RI
LAMONT-DOHERTY GEOLOGICAL OBSERVATORY Palisades NY (McCoy)
MARATHON OIL CO Houston TX
MOBIL R & D CORP Manager, Offshore Engineering, Dallas, TX
MUESER, RUTLEDGE, WENTWORTH AND JOHNSTON New York (Richards)
PORTLAND CEMENT ASSOC. Skokie IL (Rsch & Dev Lab, Lib.)
RAND CORP. Santa Monica CA (A. Laupa)
RAYMOND INTERNATIONAL INC. E Colle Soil Tech Dept, Pennsauken, NJ
SANDIA LABORATORIES Library Div., Livermore CA
SCHUPACK ASSOC SO. NORWALK, CT (SCHUPACK)
SHANNON & WILLSON INC. Librarian Seattle, WA
SHELL DEVELOPMENT CO. Houston TX (E. Doyle)
SHELL OIL CO. HOUSTON, TX (MARSHALL)
TRW SYSTEMS CLEVELAND, OH (ENG. LIB.); REDONDO BEACH, CA (DAI)

WESTINGHOUSE ELECTRIC CORP. Annapolis MD (Oceanic Div Lib, Bryan); Library, Pittsburgh PA
WOODWARD-CLYDE CONSULTANTS (Dr. R. Dominguez), Houston, TX; Library, West. Reg., Walnut Creek, CA; PLYMOUTH MEETING PA (CROSS, III)
R.F. BESIER Old Saybrook CT
T.W. MERMEL Washington DC